Short-wave sand transport in the surf zone

Korte-golf zandtransport in de brekerzone

(met een samenvatting in het Nederlands)

P R O E F S C H R I F T

ter verkrijging van de graad van doctor aan de Universiteit Utrecht
op gezag van de rector magnificus, prof. dr. G. J. van der Zwaan,
ingevolge het besluit van het college voor promoties in het openbaar te verdedigen
op dinsdag 27 maart 2018 des middags te 2.30 uur

door

Johannes Adrianus Brinkkemper
geboren op 15 juni 1986 te Zaanstad

Promotor:
Prof. dr. B. G. Ruessink

Short-wave sand transport in the surf zone

Promotor:
Prof. dr. B. G. Ruessink

Examination committee:
dr. T. Aagaard
University of Copenhagen, Denmark
Prof. dr. ir. S.G.J. Aarninkhof
Delft University of Technology, The Netherlands
Prof. dr. G. Masselink
University of Plymouth, United Kingdom
Prof. dr. T. O'Donoghue
University of Aberdeen, Scotland
Prof. dr. ir. A.J.H.M. Reniers
Delft University of Technology, The Netherlands

Short-wave sand transport in the surf zone

J. A. Brinkkemper

Voorwoord / Preface

Ook al staat er maar één naam op de voorkant van dit proefschrift, alleen had ik dit onderzoek niet kunnen voltooien. Er zijn veel mensen die mij in de afgelopen vijf jaren hierbij direct of indirect hebben geholpen. Graag wil ik deze mensen daarvoor bedanken.

Uiteraard begin ik met het bedanken van mijn begeleider en promotor Gerben. Mijn bewondering voor Gerben als onderzoeker, onderwijzer en begeleider is steeds groter geworden tijdens mijn promotietraject. Het is indrukwekkend hoe hij al zijn werkzaamheden kan combineren en toch altijd tijd vrij kan maken voor zijn promovendi. Door zijn enthousiaste en betrokken manier van begeleiden heb ik ontzettend veel kunnen leren in de afgelopen jaren. Ik ben hem ook erg dankbaar voor de vrijheid die hij me heeft gegeven tijdens het traject en de mogelijkheden om me verder te kunnen ontwikkelen. Het is ook indrukwekkend hoe hij tijdens gesprekken over elk mogelijk onderwerp altijd wel een relevant artikel kan aanraden dat ergens tussen de jaren 60 en nu gepubliceerd is. Gerben, bedankt voor alles. In Copenhagen and in Skallingen, the time spend with Troels was very valuable. The experience Troels has with the collection and analysis of field measurements is impressive and I am very grateful that he took the time to share his knowledge with me. The discussions we had in the field and behind the computer certainly sharpened my ideas on sand transport processes. Marion, thanks for you guidance during the first year of my PhD. I learned a lot from the structured way you handled both your own research as well as the supervision of students. Florent, Thijs and Jack, thanks for all your valuable input while I was writing my first paper on turbulence. De veld- en laboratorium metingen die ik heb gebruikt en verzameld waren er niet geweest zonder de inzet van de FG technici, Marcel, Henk, Chris, Arjen, Bas en Hans. Er zal zonder hun ook zeker niet zoveel te lachen zijn geweest in het veld.

De halfjaarlijkse bijeenkomsten met eindgebruikers Dirk-Jan Walstra, Jebbe van der Werf, Gemma Ramaekers, Marius Sokolewicz, Karoune Nipius, Bart Grasmeijer en Cor de Boer gaven me inzicht in de wereld buiten het onderzoek. Deze bijeenkomsten heb ik altijd als zeer waardevol beschouwd en gaven me een goed beeld van hoe mijn onderzoek, en kustonderzoek in het algemeen, kan aansluiten bij de praktijk. Jebbe bedankt voor de goede begeleiding tijdens de periode dat ik bij Deltares mocht zitten. Joep bedankt voor alle inhoudelijke discussies, het was zeer leerzaam om zo nu en dan de methoden en bevindingen van onze onderzoeken naast elkaar te kunnen leggen.

Het departement Fysische Geografie was altijd een fijne omgeving om te werken. In het bijzonder met de collega's van de kustengroep: Gerben, Maarten, Piet, Renske, Tim, Christian, Marion, Jasper, Nynke, Winnie, Pam, Yvonne, Klaas, Sepehr, Laura, Daan, Anita, Anouk en Jantien. Jullie waren altijd goed gezelschap tijdens de vele conferenties, veldwerken en uiteraard in de Zonneveldvleugel. De vele discussies met Anouk, Tim en Jantien over elkaars werk waren altijd erg motiverend en zorgden ervoor dat ik ook bleef nadenken over de bredere context van mijn eigen onderzoek. Deze discussies waren pas echt inspirerend als ze plaats vonden tijdens excursies en veldwerken op het strand, momenten waarop vaak nieuwe ideeën naar boven kwamen. Dat we samen verder konden komen bleek wel toen we, als de golfgroep en de zandlopers, tweemaal samen de Utrechtse marathon volbrachten. Anouk,

Contents

Samenvatting

Het zandtransport in morfodynamische modellen wordt vaak voorspeld met behulp van empirische parameterisaties die gebaseerd zijn op de golforbitaal beweging nabij het bed. Dit resulteert in redelijke voorspellingen van de morfodynamiek in diep water, maar voorspellingen in ondiep water ($\lesssim$ 3 m) zijn vaak onnauwkeurig. Hierdoor zijn deze modellen niet goed te gebruiken om, bijvoorbeeld, het kustwaartse zandtransport te bestuderen na de uitvoering van (vooroever)suppleties. In ondiep water worden golven asymmetrisch en produceren turbulentie door breking. Zowel de asymmetrie van de orbitaalbeweging als de geproduceerde turbulentie door golfbreking, resulteren in extra zandopwoeling. Het netto effect op het korte-golf zandtransport van deze extra opwoeling is echter onbekend. Bovendien is het meeste onderzoek naar zandtransport in ondiep water uitgevoerd in geschaalde laboratoriumfaciliteiten met regelmatige golven en is het onduidelijk hoe de resultaten van deze experimenten kunnen worden toegepast in het verklaren van het zandtransport onder onregelmatige golven in natuurlijke brekerzones. Het doel van deze studie is om onze kennis over turbulentie, zand suspensie en korte-golf zandtransport onder onregelmatige en brekende golven te verbeteren. Dit doel is nagestreefd door middel van het analyseren van metingen van stroomsnelheden, turbulentie en zandconcentraties, verzameld onder onregelmatige golven in een golfgoot en in natuurlijke brekerzones.

Gedetailleerde metingen van de kinetische turbulente energie zijn verzameld op drie hoogten boven het bed tijdens het op veldschaal uitgevoerde golfgoot experiment BARDEXII. Deze metingen zijn gebruikt om het belang van aan het oppervlak gegenereerde turbulentie te analyseren als een functie van de relatieve golfhoogte (Hoofdstuk 2). Het verticale turbulentie profiel laat een overgang zien van gedomineerd door bed-gegenereerde turbulentie onder niet-brekende golven (lage relatieve golfhoogte) boven vortex ribbels, naar gedomineerd door turbulentie gegenereerd aan de oppervlakte onder plunging brekende golven (hoge relatieve golfhoogte) boven vlakkere bodemvormen. Met een toename van de relatieve golfhoogte verandert ook de intra-golf variabiliteit van de kinetische turbulente energie. Onder niet-brekende golven bereikt de intra-golf variabiliteit een maximum op het moment dat de golforbitaalbeweging verandert van richting van negatief naar positief gerichte orbitaalbeweging. Onder brekende golven verschuift dit maximum naar het golffront. De gemeten intra-golf variabiliteit in de kinetische turbulente energie onder brekende golven laat ziet dat de aan het wateroppervlak gegenereerde turbulentie invloed kan hebben op het korte-golf zandtransport.

Het effect van turbulente wervels op zandopwoeling in de pre-brekerzone en brekerzone tijdens het BARDEXII experiment is bestudeerd in Hoofdstuk 3. Er zijn hiervoor twee verschillende benaderingen gebruikt. De eerste benadering is gebaseerd op het identificeren van een relatie tussen individuele pieken in tijdseries van turbulentie en zandconcentratie. En de tweede benadering richt zich op de variabiliteit van de kinetische turbulente energie en de zandconcentratie in de golffase met behulp van fase-gemiddelde waarden. Het deel van de pieken in de turbulentie tijdseries die gerelateerd zijn aan pieken in de zandconcentratie is relatief hoog ($\sim$ 50%) vergeleken met eerder onderzoek onder spilling brekers. Turbulentie

gegenereerd door plunging brekers is dus relatief effectief in het opwoelen van zand van het bed. Deze conclusie wordt ondersteund door het grote verschil in de intragolf variabiliteit van de zandconcentratie tussen niet-brekende en brekende golven. Onder niet-brekende shoaling golven met vortex ribbels bereikt de zandconcentratie dicht bij het bed een maximum net na het positieve maximum in de golforbitaal beweging en is er een fase-verschuiving in de verticaal. Onder brekende golven met minder steile bodemvormen piekt de concentratie onder het golffront zonder fase-verschuiving in de verticaal. Verder kustwaarts onder bores blijft de zandconcentratie fase-gekoppeld aan de positief gerichte golf-orbitaal beweging, maar de algehele concentratie neemt af richting de kustlijn. Het golfgedreven suspensief transport is dus kustwaarts gericht en het grootst onder plunging brekende golven, terwijl het zeewaarts gericht en kleiner is onder shoaling golven.

Om de algemeenheid van deze bevindingen en het resulterende zandtransport in de ondiepe brekerzone te bestuderen, is in hoofdstuk 4 de grootte, de richting en het relatieve belang van de korte-golf zandflux in de BARDEXII dataset vergeleken met twee datasets verzameld op natuurlijke zandstranden. Deze datasets vertegenwoordigen een range aan strandprofielen, met een steilheid van 1:15 tot 1:80. Ook bevatten ze veel verschillende hydrodynamische condities, van laag-energetische aangroeiende condities waar korte golven de zandflux domineren, tot hoog-energetische erosieve condities waar de gemiddelde stroming de zandflux domineert. De grootte van de korte-golf zandflux correleert onder laag-energetische condities met de orbitaalsnelheid en de asymmetrie van de orbitaalbeweging. De korte-golf zandflux voor alle condities is negatief gecorreleerd met de gemiddelde stroming, en verandert van richting onder de invloed van een sterke tegenstroom. Het relatieve belang van de korte-golf zandflux in vergelijking met de gemiddelde flux, voor alle data gecombineerd, schaalt met $(A_u u_{rms})/|\overline{u}|$, met A_u de asymmetrie van de kustdwarse orbitaalbeweging, u_{rms} de kwadratisch gemiddelde orbitaalbeweging en $\overline{u}$ de gemiddelde kustdwarse stroming. De bijdrage van de korte-golf zandflux is hoog ($\sim$ 70%) als deze ratio hoog is ($\sim$ 10) en laag en soms negatief ($\sim$ 0%) als de ratio laag is ($\sim$ 1). Deze veld en laboratorium metingen onder onregelmatige golven ondersteunen dus de hypothese dat de asymmetrie van de orbitaalbeweging gebruikt kan worden ter verbetering van morfodynamische modellen voor het voorspellen van de morfologische ontwikkeling in de ondiepe brekerzone.

Summary

Morphodynamic models usually contain empirical parameterisations to estimate sand transport quantities from near-bed characteristics of wave-orbital motion. While this results in reasonable predictions of the nearshore morphodynamics in deeper water, predictions in shallow water ($\lesssim$ 3 m) are largely inaccurate. This precludes the use of these models to study, for example, the cross-shore sand transport toward the beach after the implementation of (shoreface) nourishments. In shallow water, waves become asymmetric (pitched forward) and generate turbulence through breaking. Both wave asymmetry and surface-generated turbulence can induce additional sand suspension; however, the net effect on sand transport is not clear. Moreover, most research on nearshore sand transport has been conducted in small-scale laboratory facilities with regular waves, and it is often not trivial how these measurements relate to sand transport beneath irregular waves in natural surf zones. The aim of this thesis is to improve our knowledge on turbulence, sand suspension and short-wave sand transport beneath irregular breaking waves. This aim is fulfilled through the analysis of turbulence and sand concentration measurements, collected beneath irregular waves in a field-scale laboratory flume and in natural surf zones.

Detailed measurements of the turbulent kinetic energy at three elevations above the bed were collected during the field-scale laboratory experiment BARDEXII to analyse the importance of surface-generated turbulence as a function of the relative wave height (Chapter 2). The vertical turbulence profile shows a transition from being dominated by bed-generated turbulence beneath non-breaking waves (low relative wave height) above vortex ripples to being dominated by surface-generated turbulence beneath plunging breaking waves (high relative wave height) above subdued bed forms. Analogously, the intrawave variability of the turbulent kinetic energy changes from reaching its maximum value at the instance of negative to positive flow-reversal beneath non-breaking waves to a maximum value beneath the wave front beneath breaking waves. The measured intrawave variability indicates that the surface-generated turbulence beneath plunging breaking waves can potentially affect sand suspension and short-wave transport.

The effect of turbulent vortices on sand suspension in the shoaling and surf zone of the BARDEXII beach is subsequently studied in Chapter 3. This possible effect is studied using two different approaches. An event-based approach is used to identify whether individual turbulence events are linked to suspension events and vice versa, and a wave-phase averaging approach is used to study the intrawave variability of both the turbulent kinetic energy and the sand concentration. The fraction of turbulence events that relates to suspension events is relatively high ($\sim$ 50%) in comparison with previous measurements beneath spilling breakers. Surface-generated turbulence beneath plunging breakers is thus relatively effective in stirring sand from the bed. This is also reflected by the large difference between non-breaking and breaking waves in intrawave variability of the sand concentration. Beneath nonbreaking shoaling waves with vortex ripples, the sand concentration close to the bed peaks right after the maximum positive wave-orbital motion and shows a marked lag in the vertical. Beneath plunging waves with subdued bed forms, concentration peaks beneath the wave-

front without any notable phase lags in the vertical. Further shoreward beneath bores, the sand concentration remains phase-coupled to the positive wave-orbital motion, but the concentration decreases toward the shoreline. The wave-driven suspended sand transport is thus onshore-directed and largest beneath plunging waves, while it is small and can also be offshore-directed beneath shoaling waves.

To explore the generality of these findings and the resulting sand transport in the shallow surf zone, the magnitude, direction and relative importance of the short-wave sand flux in the BARDEXII dataset is compared with measurements collected on two natural sandy beaches in Chapter 4. The datasets represent a wide range of beach slopes, from 1:15 to 1:80. And include a range in hydrodynamic conditions, from low-energetic accretive conditions with short-waves dominating the total sand flux, to high-energetic erosive conditions with the mean cross-shore current dominating the total sand flux. The relative importance of the short-wave sand flux in comparison with the mean flux, for all data combined, scales with $(A_u u_{rms})/|\overline{u}|$, where A_u is the velocity asymmetry, u_{rms} is the root-mean-square orbital motion and $\overline{u}$ is the mean cross-shore current. Contributions are high ($\sim 70\%$) when this ratio is high (~ 10) and low and sometimes negative ($\sim 0\%$) when this ratio is low (~ 1). These field and laboratory measurements under irregular waves thus support the hypothesis that the inclusion of velocity asymmetry in transport formulations would improve the performance of morphodynamic models in the shallow surf zone.

Chapter 1

Introduction

1.1 Context

The sand that forms our beaches is constantly redistributed by waves and wave-induced currents. Depending on the water level and offshore wave characteristics this will either result in beach accretion, where the shoreline shifts seaward, or beach erosion, where the shoreline shifts landward. The latter is a harmless process along natural uninhabited coastlines, but because coastal areas accommodate a large part of the human population (Small and Nicholls, 2003), with approximately 10% of the world's population living less than 10 m above sea level (McGranahan et al., 2007), coastal erosion is often problematic. Coastal vulnerability because of long-term erosion can have natural and man-induced causes and is expected to increase with the anticipated accelerated sea-level rise (0.3 – 1.0 m by 2100; Wong et al., 2014), potential increase in storminess, and pressure from a rapidly growing human population.

In the Netherlands a sandy strategy has been chosen to maintain the coastline (de Ruig and Hillen, 1997): here, large deposits of sand are placed along the entire coast, with a total volume of 12 million m³ per year and an estimated budget of 63 million euros in 2017 (Rijksoverheid, 2017). These nourishments are either applied above the mean water line as beach nourishments, or in shallow (4–8 m) water as shoreface nourishments. The latter approach is relatively cost-effective and is thus increasingly applied to nourish sandy coasts (Hamm et al., 2002). It is crucial to understand the processes driving sand transport from deeper water to the beach for an efficient design of shoreface nourishments, both in terms of time and money, and to determine the effect of these nourishments on nearshore morphology and the beach.

Practice-oriented engineering models (e.g., Delft3D (Lesser et al., 2004) and Unibest (Ruessink et al., 2007)) are a key tool to study the vulnerability of coastlines and to design measures to diminish long-term erosion. These morphodynamic models usually contain empirical parameterisations to relate transport quantities to near-bed wave-driven flow characteristics (e.g., Bailard, 1981; Ribberink, 1998; van Rijn, 2007a; van Rijn, 2007b). While these parameterisations result in reasonable predictions of nearshore morphodynamics in deeper water (Ruessink et al., 2007; Ruggiero et al., 2009; Walstra et al., 2012), predictions in shallow water ($\lesssim$ 3 m) are largely inaccurate, in particular due to a high degree of wave nonlinearity and breaking-induced turbulence. A better understanding of sand transport in shallow water, and ultimately the translation of this knowledge into practical engineering models, is thus needed to decrease these inaccuracies (e.g., van Rijn et al., 2013).

1.2 Short waves in the surf zone

1.2.1 Focus on short waves

Cross-shore sand transport in shallow water is driven by waves and wave-induced currents, of which the former is often separated based on wave frequency in long (or low-frequency, 0.005 – 0.05 Hz) waves and short (or high-frequency, 0.05 – 1 Hz) waves. The net sand flux (q_{tot}) at a specific height above the bed, is the result of a summation of the mean flux q_m, the low-frequency flux q_{lf} and the high-frequency flux q_{hf}, which are calculated by a multiplication of frequency-filtered cross-shore velocity (u_m, u_{lf} and u_{hf}) with the frequency-filtered sand concentration (c_m, c_{lf} and c_{hf}) as

$$q_{tot} = q_m + q_{lf} + q_{hf} = u_m c_m + \langle u_{lf} c_{lf} \rangle + \langle u_{hf} c_{hf} \rangle, \tag{1.1}$$

where $\langle ... \rangle$ denote time-averaging. The total sand transport is obtained by integrating the flux over the water depth.

The direction of the net cross-shore sand transport in the surf zone is mainly related to the offshore wave conditions, with an offshore directed transport leading to beach erosion during high energetic wave conditions and an onshore directed transport resulting in beach accretion during low energetic wave conditions. The offshore directed transport of sand during storms is mainly driven by offshore directed wave-induced currents (Osborne and Greenwood, 1992b; Gallagher et al., 1998; Aagaard and Hughes, 2010), also referred to as the undertow. During low energetic conditions the onshore directed sand transport is mainly driven by short waves (Osborne and Greenwood, 1992a; Osborne and Greenwood, 1992b;

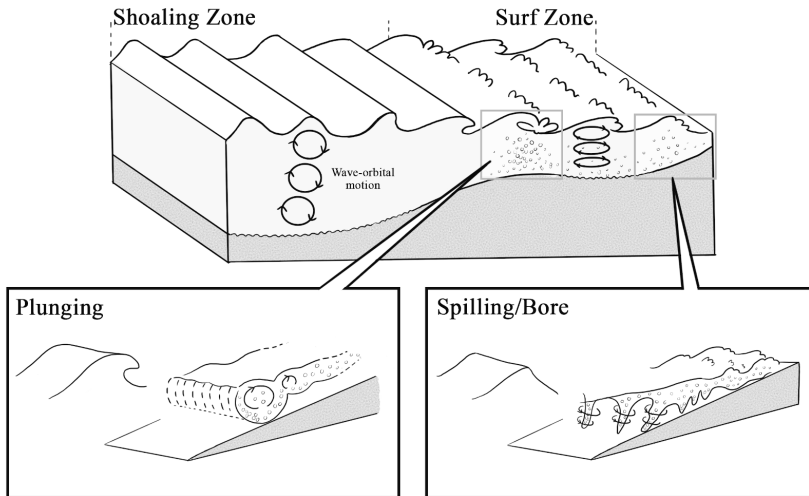**Figure 1.1: The transformation and breaking of waves over a longhore bar. The lower plots show the difference between plunging and spilling breakers in terms of wave shape and generated turbulence. Plunging breakers generate large vortices around a horizontal axis, while beneath spilling breakers and bores obliquely descending eddies around a vertical axis are observed (lower plots based on Zhang and Sunamura (1994)).**

Ruessink et al., 1998; Hoefel and Elgar, 2003). Offshore directed sand transport by mean currents is relatively well understood and the morphodynamics during high energetic conditions are thus well represented in practical engineering models (van Rijn et al., 2011). This is not true for the onshore directed sand transport by short waves (van Rijn et al., 2011), particularly in the turbulent surf zone (van Rijn et al., 2013) where waves are highly nonlinear and inject breaking-induced turbulence into the water column (e.g., Figure 1.1). To improve our understanding of sand transport in the surf zone, this study focuses on the short-wave contribution to sand transport under breaking waves. The following sections describe the wave hydrodynamics in shallow water, i.e. wave nonlinearity (Section 1.2.2) and breaking-induced turbulence (Section 1.2.3), and how these mechanisms may result in a nonzero short-wave sand transport (Section 1.2.4).

1.2.2 Wave nonlinearity

When short waves propagate into intermediate water depths, which is defined as a water depth less then a quarter to half the wavelength (Masselink and Hughes, 2003), the wave hydrodynamics are affected by the sea bed (Figure 1.1). The interaction with the bed results in a shortening of the wavelength and a simultaneous increase in waveheight as the energy flux is conserved, a process called shoaling. Simultaneously, the wave shape and the orbital motion alter through nonlinear energy transfers from primary wave frequencies to their higher harmonics (Elgar, 1987). These nonlinear energy transfers cause the shape and orbital motion of initial sinusoidal waves (Figure 1.2a) to become asymmetric in the horizontal with narrow short-duration crests and flat long-duration troughs (Figures 1.2b and 1.2c). The horizontal asymmetry of the wave shape and the wave orbital motion is referred to as wave skewness and velocity skewness, respectively, and is calculated for a time-series of high-frequency cross-shore velocity as

$$S_u = \frac{\langle u_{hf}^3 \rangle}{\langle u_{hf}^2 \rangle^{3/2}}. \tag{1.2}$$

Values for S_u on moderately sloping beaches typically range between 0 and 1.5 (Figure 1.3a).

The primary wave frequencies and their higher harmonics are in phase beneath skewed waves, but this changes when the water depth further decreases. Here, the higher harmonics will increasingly phase-lag the primary frequencies (Flick et al., 1981; Elgar and Guza, 1985a; Elgar and Guza, 1985b) and waves become pitched-forward (Figures 1.2c and 1.2e), i.e. asymmetric in the vertical. This is referred to as wave asymmetry (shape) and velocity asymmetry (wave orbital motion) and is related to the acceleration skewness (Elgar, 1987). The velocity asymmetry A_u is estimated by replacing u_{hf} in Equation 1.2 by its Hilbert transform. Values for A_u typically decrease from 0 under horizontal symmetric waves to -1.5 under asymmetric bores (Figure 1.3b).

The degree of wave nonlinearity of irregular waves, expressed in the skewness and asymmetry, was found to scale with the Ursell number (Doering and Bowen, 1995; Abreu et al., 2010; Ruessink et al., 2012a), which is a function of the local wave period, the wave height and the water depth. Ruessink et al. (2012a) used 30.000+ field observations (Figure 1.3) to develop parameterisations to estimate S_u and A_u with these local wave parameters. These parameterisations are currently implemented in several morphodynamic models (e.g., van der Werf et al., 2012; Dubarbier et al., 2015; Fernández-Mora et al., 2015; van der Werf et al., 2015). There is, however, considerable scatter of the data around the parameterisations and Ruessink et al. (2012a) already pointed out that S_u may be underestimated for narrow-banded swell, on steep beach slopes and in laboratory flumes. Rocha et al. (2017) suggested
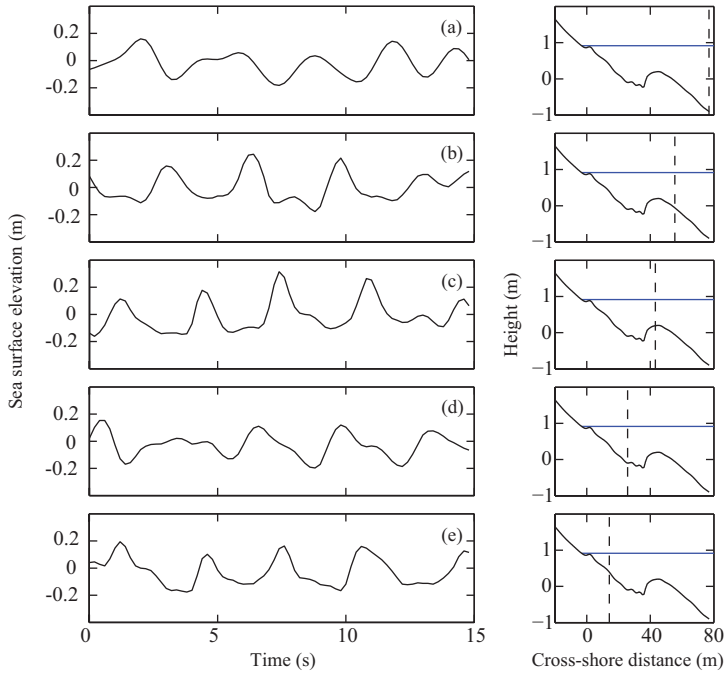
Figure 1.2: (a–e) Observations of sea surface elevation η on different cross-shore locations during a field campaign at Egmond aan Zee in 2011. The adjacent small plots show the (dashed line) location where the measurements were collected with respect to the (solid line) beach profile, and the (blue line) water level. Values for wave shape skewness S_η and wave shape asymmetry A_η, for the full 30 min length time series from which these examples were taken, are (a) -0.1 and 0.0, (b) 0.3 and -0.2, (c) 0.5 and -0.5, (d) 0.1 and 0.0, (e) 0.3 and -0.8. Figure from Brinkkemper (2013).

to reduce this scatter by including the local beach slope and offshore wave characteristics (spectral bandwidth and wave steepness).

The process of wave transformation results in wave breaking when the front of the wave becomes too steep for the wave to maintain its shape. On mild to moderately sloping beaches, as are found in the Netherlands, two types of breaking waves can be distinguished, namely plunging and spilling breakers (Figure 1.1). The beach slope and the offshore wave steepness determine which breaker type prevails (Battjes, 1974). After initial breaking, the wave transforms into a surf bore, with decreasing skewness and increasing asymmetry with distance from the location of initial wave breaking. The surf zone is the area where waves break and is separated into the outer surf zone, from the location of the most seaward located initial breaking wave to the location where all waves are broken, and the inner surf zone, where all waves are present as bores. In the surf zone, wave heights decrease due to energy loss through turbulence present at the wave front. This results the wave height to become linearly dependent on the water depth in the inner surf zone (Thornton and Guza, 1982).

1.2.3 Breaking-induced turbulence

Turbulence in the nearshore zone is generated both at the bed and at the water surface. The former is generated by the interaction between water flow and the bed, the latter by break-

ing waves and bores (Thornton, 1979). Both turbulence types can affect sand entrainment from the bed, as surface-generated vortices are able to travel downward and reach the bed (Nadaoka et al., 1988; Zhang and Sunamura, 1994; Scott et al., 2005; Aagaard and Hughes, 2010; Yoon and Cox, 2012; Van der A et al., 2017). The ratio between bed-generated and surface-generated turbulence beneath irregular waves is related to the location in the cross-shore (Feddersen et al., 2007; Ruessink, 2010; Grasso et al., 2012; de Winter et al., 2013). In the shoaling zone the bed is the dominant turbulence source, but the surface-generated turbulence becomes increasingly significant as the fraction of breaking waves increases. The turbulence intensity and degree of vertical mixing is enhanced simultaneously (e.g., de Winter et al., 2013).

The aforementioned different breaker types generate turbulence vortices with different characteristics (Figure 1.1). These vortices have been studied in much detail beneath regular waves in laboratory facilities (e.g., Nadaoka et al., 1989; Zhang and Sunamura, 1990) and using numerical models (e.g., Kim et al., 2017; Zhou et al., 2017). The most relevant characteristics to affect sand suspension and transport are the fraction of vortices that reach the bed, the direction of the oscillatory flow when vortices reach the bed, and the induced degree of vertical mixing. Beneath spilling breakers and bores, most of the turbulence is confined to the upper part of the water column (Ting and Kirby, 1996; Grasso et al., 2012), but can travel downwards behind the wave crest in descending eddies (Nadaoka et al., 1989; Zhang and Sunamura, 1990). Turbulence beneath plunging breakers is organised in large horizontal vortices generated by the overturning wave crest (Zhang and Sunamura, 1990). These vortices more effectively affect the near-bed turbulence and, due to their scale, strongly enhance the vertical mixing (Ting, 2013; van der Zanden et al., 2016). While the dynamics
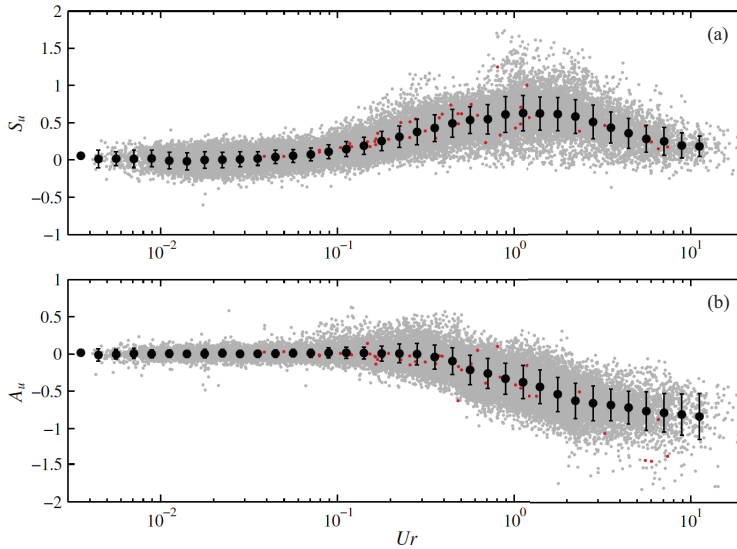

Figure 1.3: (a) Near-bed velocity skewness S_u and (b) asymmetry A_u as a function of the Ursell number Ur. The grey dotes are estimated values from field measurements, the black dots represent class-mean values with their standard deviation. The red dots are the data from Doering and Bowen (1995). Figure from Ruessink et al. (2012a).

of these vortices and their impact on the bed is well understood beneath regular waves, the translation of this knowledge to irregular waves in natural surf zones remains a challenge.

1.2.4   Sand suspension and transport

Observations of the effect of nonlinear oscillatory flow on sediment suspension and transport in oscillatory flow tunnels (e.g., King, 1991; Ribberink and Al-Salem, 1994; O'Donoghue and Wright, 2004; van der A et al., 2010), wave flumes (e.g., Flick et al., 1981; Sato et al., 1990; Barkaszi and Dally, 1992; Ting and Kirby, 1994; Thorne et al., 2002; Scott et al., 2009; Yoon and Cox, 2012; Henriquez et al., 2014; Masselink et al., 2016; van der Zanden et al., 2017) and in the field (e.g., Kana, 1978; Nielsen, 1984; Hanes and Huntley, 1986; Osborne and Greenwood, 1992a; Ruessink et al., 1998; Foster et al., 2006; Grasso et al., 2011; Aagaard et al., 2013) in past decades largely extended our knowledge on wave-driven transport processes in the surf zone. Experiments in oscillatory wave tunnels allow for the isolation of the near-bed effects of the cross-shore component of the wave-orbital motion. Under flat-bed conditions, skewed oscillatory flow drives sand transport in the positive ("onshore") direction (Ribberink and Al-Salem, 1994) due to the difference in magnitude between the maximum positive and negative "offshore") directed velocities and the associated difference in concentrations. Above a rippled bed, vortex shedding can strongly reduce this transport or even reverse the direction (e.g., Vincent and Green, 1990; Thorne et al., 2003; O'Hara Murray et al., 2011), as these vortices entrain the majority of sand during the positive to negative flow reversal and most sand is thus available during the negative directed flow phase (O'Donoghue and Wright, 2004; van der Werf et al., 2007).

Velocity asymmetry was long believed not to impact sand transport, as the positive and negative directed velocity are of the same magnitude. For example, Roelvink and Stive (1989) assumed that asymmetric bores do not transport sand in a net direction. This changed when Elgar et al. (2001) suggested the importance of acceleration skewness to the onshore migration of nearshore bars. The onshore directed transport by asymmetric (or, acceleration skewed) flow was later shown in several flow tunnel experiments (Watanabe and Sato, 2004; van der A et al., 2009; Ruessink et al., 2011; Silva et al., 2011) and was found to be driven by several mechanisms. Firstly, the wave-boundary layer has less time to grow during the high acceleration between the maximum negative and maximum positive directed flow, in comparison with the low acceleration with a long duration between maximum positive and maximum negative directed flow. This results in higher vertical gradients in flow velocity and thus shear stresses during the positive flow phase (Nielsen, 1992; Henderson et al., 2004; van der A et al., 2008). Secondly, sand stirred during maximum negative flow has less time to settle before the flow reversal from negative to positive directed flow, in comparison with the longer duration between maximum positive flow and the flow reversal from positive to negative directed flow. This second effect largely depends on the sediment fall velocity and is probably only of importance when the grain size is smaller than about 200 μm (Ruessink et al., 2009).

While the effects of flow nonlinearity on sand transport can be isolated in these flow tunnel experiments, observations under nonlinear waves in laboratory flumes and on natural beaches show additional mechanisms that can affect suspended sand transport. Besides the horizontal wave-orbital motion, progressive surface waves also include a vertical component. This vertical wave-orbital motion is maximum upward directed beneath the front of the wave (i.e. during the negative-positive flow reversal) and can thus stimulate onshore wave-driven suspended transport, in particular when this velocity exceeds the sand fall velocity higher in the water column (Kranenburg et al., 2013). Moreover, experiments in laboratory flumes

and on natural beaches include wave breaking and the corresponding injection of turbulence. Crucially, the timing of this turbulence injection in the wave phase determines whether sand is brought in suspension during onshore or offshore directed wave velocities. Studies suggest that this phase-coupling depends on the breaker type with positive phase-coupling beneath plunging breakers (Ting and Kirby, 1994; Ting, 2013; Aagaard and Hughes, 2010) and negative (Ting and Kirby, 1994; Scott et al., 2009) or no phase-coupling (Nadaoka et al., 1988; Sato et al., 1990; Barkaszi and Dally, 1992; Aagaard and Hughes, 2010) beneath spilling breakers and bores. It is, however, difficult to separate the effect of breaking-induced turbulence from the effects of velocity asymmetry on the short-wave transport (e.g., van Thiel de Vries et al., 2008). Another factor which could affect the short-wave sand transport in the surf zone is the often strong opposing current, i.e. undertow, as was shown in an oscillatory flow experiment by Ruessink et al. (2011). An opposing current increases sand pick-up from the bed during the negative flow phase by enhancing the shear stress and similarly decreases sand pick-up during the positive flow phase. This effect was earlier suggested to be important to the offshore transport by long waves in the inner-surf zone (de Bakker et al., 2016), but its significance for sand transport by short waves in a natural surf zone is unknown. Overall, separate effects of relevant processes are well understood from idealised laboratory experiments, but it remains unclear what the relative contributions of these processes are to the short-wave sand transport in natural surf zones.

1.3   Research aims and thesis outline

The main aim of this study is to better understand the processes involved in sand suspension and transport by short waves in a natural surf zone. The specific research objectives for Chapters 2–4 are to:

1. ***Determine the cross-shore variability of turbulence in terms of the vertical profile and the intrawave variability***
   The majority of research on turbulence characteristics beneath breaking waves was and still is conducted in scaled laboratory flumes and/or with regular wave series (e.g., Nadaoka et al., 1988; Ting and Kirby, 1994; van der Zanden et al., 2016). To extend our knowledge of how the findings from these measurements can be applied to field conditions, as a first step, measurements of turbulence, collected in a field-scale laboratory flume and beneath irregular waves during the BARDEXII experiment (Masselink et al., 2016), are analysed in Chapter 2 (Figure 1.4a). With instruments to measure turbulence at one cross-shore location, and a wide variety of wave conditions, these analyses provide a good overview of turbulence beneath a wide range of wave types, and cover both the shoaling and the surf zone. Here, the analyses are focused on the vertical structure and the wave phase dependency of turbulent kinetic energy.

2. ***Analyse the effect of breaking-induced turbulence on the suspension of sand***
   In Chapter 3, the turbulence data from the field-scale flume experiment are combined with measurements of sand concentration to assess how breaking-induced turbulence can affect suspension and transport of sand. Therefore, the main differences in suspension of sand beneath non-breaking and plunging breaking waves are analysed with both an event-based approach and a wave phase-averaged approach. The former approach focuses on the importance of individual events in the turbulence and sand concentration measurements and whether individual events in turbulence can be related to events in the concentration.

The latter approach focuses on the variability of both turbulence and sand concentration in the wave phase.

3. *Determine which hydrodynamic parameters scale with the short-wave sand transport in the shallow surf zone*
   The effects of the nonlinearity of the wave orbital motion, breaking-induced turbulence and opposing currents on sand suspension have been studied in detail in oscillatory flow tunnels (e.g., King, 1991; van der A et al., 2009; Ruessink et al., 2011), laboratory flumes (e.g., Ting and Kirby, 1994; Scott et al., 2009) and numerical models (e.g., Hsu et al., 2006; Hoefel and Elgar, 2003; Fernández-Mora et al., 2015). The relative importance of these effects for the short-wave sand transport in natural shallow surf zones has received much less attention. In Chapter 4 the measurements from the BARDEXII dataset are compared with field datasets collected at two natural beaches (Figure 1.4b) in the Netherlands during field campaigns at the beach of Ameland (barrier island in the Wadden Sea) in 2010 and the beach of the Sand Engine (a mega nourishment near Ter Heijde) in 2014 to gain more insight into the factors explaining the direction and magnitude of the short wave transport in the shallow surf zone.

In Chapter 5, the research questions are answered and discussed, and recommendations are given for further research. As the Chapters 2, 3 and 4 were published separately in scientific journals (Brinkkemper et al., 2016; Brinkkemper et al., 2017b; Brinkkemper et al., under review), there is some overlap between the chapters, particularly in the descriptions of data collection and processing.

Figure 1.4: (a) Plunging breaker in the Deltaflume during the BARDEXII experiment and (b) the cross-shore instrument array, as deployed during the campaigns at the beaches of Ameland and the Sand Engine, during low tide at the Sand Engine.

Chapter 2

Observations of turbulence

Abstract

Current coastal-evolution models generally lack the ability to accurately predict bed level change in shallow ($\lesssim$ 2 m) water, which is, at least partly, due to the preclusion of the effect of surface-induced turbulence on sand suspension and transport. As a first step to remedy this situation, we investigated the vertical structure of turbulence in the surf zone using measurements collected under random shoaling and plunging waves on a steep (initially 1:15) field-scale sandy laboratory beach. Turbulence was measured with a vertical array of three Acoustic Doppler Velocimeters (ADVs). The vertical turbulence structure evolves from bottom-dominated to approximately vertically uniform with an increase in the fraction of breaking waves to $\sim$ 50%. We further find that the instantaneous turbulence kinetic energy is phase-coupled with the short-wave orbital motion under the plunging breakers, with higher levels shortly after the reversal from offshore to onshore motion (i.e. wavefront).

2.1 Introduction

Morphodynamic models can predict morphological change in the nearshore zone with reasonable accuracy, where the water depth exceeds $\sim$ 2 m and the morphology is approximately alongshore uniform (e.g., Plant et al., 2004; Ruessink, 2005; Ruessink et al., 2007; Ruggiero et al., 2009; Kuriyama, 2012; Walstra et al., 2012). There is, however, still a mismatch between predictions and observations for the inner surf zone (e.g., Ruessink, 2005; Masselink and Puleo, 2006; Ruessink and Kuriyama, 2008). This zone is, together with the swash zone, the connection for sand exchange between deeper water and the beach and is thus of high importance for the design of beach-restoration and nourishment projects. Most morphodynamic models calculate sediment transport solely with near-bed wave orbital motions (e.g., Bailard, 1981; Ribberink, 1998), lacking the earlier measured influence of surface-induced turbulence on sand entrainment and transport (Nadaoka et al., 1988; Voulgaris and Collins, 2000; Aagaard and Hughes, 2010; Yoon and Cox, 2012). To improve the transport formulations for shallow water, a better understanding of the mechanisms involved in the suspension and transport of sand is needed (e.g., van Rijn et al., 2013). This chapter presents a recently collected field-scale laboratory dataset and focuses on the vertical structure of turbulence in the surf zone as a first step toward more accurate sand transport predictions.

The difference between the shoaling and the surf zone in terms of sediment suspension is the presence of surface-induced turbulence in the surf zone (Aagaard and Hughes, 2010). In the surf zone, turbulence is generated by breaking waves and bores in horizontal and oblique vortices (Nadaoka et al., 1989; Zhang and Sunamura, 1990), able to travel downward to the bed and suspend sediment intermittently (Nadaoka et al., 1988; Voulgaris and Collins, 2000; Aagaard and Hughes, 2010; Yoon and Cox, 2012). As these vortices also keep sediment in suspension, the timing of these vortices in the wave phase determines whether vortices, and thus sediment, are transported in the landward or seaward direction by the wave orbital motion. The structure and intermittency of the generated turbulence are highly dependent on the breaker type (Zhang and Sunamura, 1990). The turbulence in spilling breakers is confined to the upper part of the water column due to the relatively small size of the generated eddies ($0.1 - 0.2h$, where h is the water depth) (Ting and Kirby, 1996), but turbulence spreads downwards in obliquely descending eddies behind the wave crest (Figure 1.1; Nadaoka et al., 1989). The amount of turbulence is fairly homogeneous over a wave cycle beneath spilling breakers and thus turbulence is generally transported in the seaward direction due to the longer duration of the offshore wave motion (Ting and Kirby, 1994). Turbulence beneath plunging breakers is characterised by downburst vortices generated by the impact of the overturning wave crest. This results in large mixing lengths and more homogeneous turbulence intensities in the vertical. The vortices were found around the breaking wave front and are thus correlated with onshore orbital motions, resulting in an onshore transport of turbulence beneath plunging breakers (e.g., Ting and Kirby, 1994; Ting and Kirby, 1995). Recently, Aagaard and Hughes (2006) as well as Aagaard and Jensen (2013) found the largest sediment concentrations just after the onshore velocity maximum for plunging breakers in the field, suggesting the coupling between turbulence and suspension events and sediment transport by the wave orbital motion in the onshore direction. The sediment concentration beneath bores was much more homogeneous over time and no net wave-induced sediment transport was measured.

The change from near-bed orbital motion to surface-generated eddies as dominant sand stirring mechanism from the shoaling into the surf zone is also reflected in measured vertical profiles of wave-averaged turbulent kinetic energy (k). Numerous small-scale laboratory experiments have been conducted with a fixed bed and regular breaking waves using laser

Doppler anemometry (LDA, see Mocke (2001) for an overview) and more recently with particle image velocimetry (PIV) (e.g., Kimmoun and Branger, 2007; Sou et al., 2010; Govender et al., 2011). These methods provide detailed turbulence measurements in the cross-shore and vertical directions, while the alongshore component is often approximated assuming that turbulence beneath breaking waves is similar to plane wake flow (Svendsen, 1987). The vertical structure of turbulence was found to depend strongly on the wave-breaking type. Conditions with plunging breakers result in a relatively uniform turbulence profile, while spilling breakers show a strong increase of turbulent kinetic energy close to the water surface. Typical values for the Froude-scaled turbulent kinetic energy ($\sqrt{k/gh}$, where g is the gravitational acceleration and h is the water depth) below the wave trough level are between 0.03 and 0.07 for spilling breakers, and between 0.05 and 0.1 below plunging breakers (Mocke, 2001).

While these small-scale laboratory studies have provided substantial knowledge on turbulence beneath regular breaking waves on a fixed bed, it is uncertain how these measurements compare to field scale and irregular waves over a mobile bed. Scott et al. (2005) measured turbulence beneath regular and irregular breaking waves above a fixed bed in a large-scale flume and found a similar vertical and cross-shore structure of turbulence for both wave conditions, but the magnitude of the turbulent kinetic energy was up to five times larger beneath regular waves. The vertical structure and intensity (Froude-scaled turbulence between 0.02 and 0.06 at the bar crest) of turbulent kinetic energy measured during the experiments with identical random wave conditions but with a movable bed were similar to experiments with a fixed bed (Yoon and Cox, 2010). In these large-scale laboratory experiments, turbulence characteristics were measured using several vertical arrays of Acoustic Doppler Velocimeters (ADVs), offering some insight into their cross-shore structure. In general the turbulent kinetic energy is maximum at the location where most wave energy is dissipated by breaking, consistent with the dominance of surface-generated turbulence. In the field, however, a vertical profile of turbulence is often measured at a single cross-shore location because of logistical constrains (e.g., Feddersen et al., 2007; Ruessink, 2010). The time-variation in offshore wave conditions and tidal water level then results in measurements at different locations with respect to the breaker zone, but instruments at one cross-shore location inherently do not provide any information on the cross-shore variability of the turbulent structure. Field experiments show a dependency of the vertical turbulence structure on H_s/h in the surf zone, where H_s is the significant wave height. Surface-induced turbulence becomes increasingly important with higher relative wave height and is dominant in the inner surf zone (e.g., Grasso et al., 2012; Lanckriet and Puleo, 2013), where the majority of the waves have transformed into bores and ripples are generally absent. Measurements in natural surf zones indicate that turbulence intensities increase towards the surface and towards the bed (Feddersen et al., 2007; Grasso et al., 2012), indicating that both surface-induced and bed-induced turbulence are important in the field. Grasso et al. (2012) hypothesized that the difference between field datasets in turbulence intensities in the lower part of the water column, and with laboratory measurements with a fixed bed, might be explained by differences in bed roughness (i.e. presence of ripples). On the whole, there is still substantial need for turbulence observations under natural conditions.

Although the vertical structure of turbulence in idealised laboratory surf zones is well researched, measurements of turbulence at field scale are scarce but necessary to make progress in our understanding of sediment transport in shallow water. This lack of data and process understanding was one of the reasons to carry out the second large-scale Barrier Dynamics Experiment (BARDEXII). BARDEXII was designed to improve understanding of sediment transport processes in the surf, swash and overwash zone (see also Masselink et al. (2016))
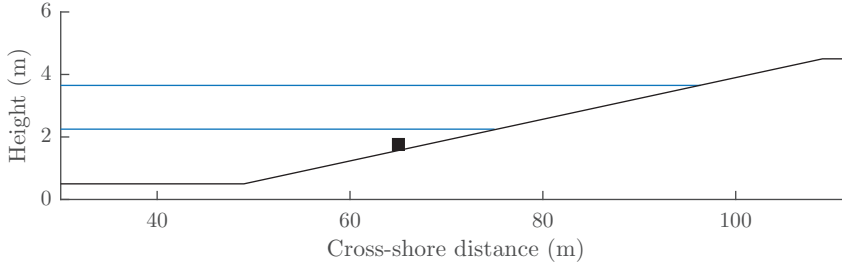
Figure 2.1: Initial beach profile during the BARDEXII experiment. The cross-shore distance is 0 at the wave-maker. The vertical distance is positive upward from the concrete floor. The square represents the location of the turbulence rig. The blue lines represent the lowest and highest still water level during the cases described in this chapter, see Table 2.1.

of a medium-coarse grained sandy barrier. This chapter focuses on the measured vertical structure of turbulence and its variability from the shoaling into the surf zone. The structure of this chapter is as follows. In Section 2.2, we describe the experimental setup, initial data processing and the methods used to extract turbulence from the measured velocities. In Section 2.3 we discuss the vertical profiles of turbulence and its intrawave variability in the shoaling and surf zones. These results are discussed and compared with earlier observations in Section 2.4. Conclusions are provided in Section 2.5.

2.2 Methods

2.2.1 BARDEXII

The BARDEXII experiment was carried out in the Delta Flume in Vollenhove, The Netherlands, from May to July 2012. A 4.5 m high, 5 m wide and 75 m long sandy (median grain diameter $d_{50} = 430\ \mu$m) barrier was constructed in the central region of the flume, enabling a lagoon to be situated at its landward side. Initially, the profile contained an 1:15 slope from $x = 49$ m to $x = 109$ m, where $x = 0$ is at the wavemaker (Figure 2.1). Masselink et al. (2016) describe the objectives and the experimental setup of the project. We focus on the specific conditions and instruments that are used in this study.

The experiment consisted of five test series (A – E) with a total of 19 distinct tests with different wave and water level conditions. Test series A focused on beach response to varying wave conditions and different lagoon levels; B on bar dynamics due to different water levels on the seaside of the barrier; C on beach response to varying wave conditions with a tide; D on identifying overtopping/overwash thresholds and E on barrier overwash. Table 2.1 provides an overview of the significant spectral wave height H_s and peak period T_p near the wavemaker, and of the water level relative to the flume floor $\bar{\zeta}$. The wavemaker was forced with random waves with a JONSWAP spectrum. The test series were divided in runs with a length of 15 – 180 min. In between these runs the cross-shore bed profile was measured along the centerline of the flume with a mechanical bed profiler (cross-shore resolution of 0.01 m). Between several test series, a run with monochromatic waves and a run with bichromatic waves were additionally carried out.

Table 2.1: Hydrodynamic conditions during the BARDEXII experiment, with wave height H_s, peak wave period T_p, water elevation in respect to the concrete floor $\overline{\eta}$, and the fraction of breaking waves at the location of the turbulence rig Q_b.

Test	H_s (m)	T_p (s)	$\overline{\eta}$ (m)	Q_b
A1	0.89	8	3	0.07
A2	0.88	8	3	0.09
A3	0.88	8	3	0.07
A4	0.88	8	3	0.11
A6	0.69	12	3	0.01
A7	0.77	12	3	0.05
A8	0.77	12	3	0.04
B1	0.89	8	3	0.03 − 0.08
B2	0.87	8	2.5	0.17 − 0.26
C1	0.88, 0.55	8	2.25 − 3.65	0.41 − 0
C2	0.55, 0.90	8	3.53 − 2.25	0 − 0.48
D1	0.74	4	3.15 − 4.2	0
D2	0.79	5	3.45 − 4.05	0
D3	0.80	6	3.45 − 3.9	0
D4	0.83	7	3.45 − 3.9	0
D5	0.79	8	3.45 − 3.75	0
D6	0.81	9	3.30 − 3.75	0
D7	0.81	10	3.15 − 3.6	0
E1	0.90	8	3.9	0

2.2.2 Instruments

Measurements were collected at x=65 m (Figure 2.1). Here, 3 sideways-oriented and vertically stacked Sontek Ocean ADVs were positioned (Figure 2.2a) to measure all three velocity components. The instruments were, together with a pressure transducer (PT), attached to a wall-mounted scaffolding rig with around 2 m between the instruments and the nearest flume wall. The vertical position of the rig was manually adjustable, ensuring an equal height of the instruments above the bed at the start of each run (0.175, 0.435 and 0.7 m for ADV1-3 and 0.25m for the PT). The time series of instantaneous pressure were converted to sea surface elevation using linear wave theory and processed into the values of the local waterdepth h and high-frequency ($0.05 < f < 1$ Hz) wave height H_s. The lowermost ADV failed during series A1-A6, and was replaced by a Nortek ADV in series A7. The Sonteks operated at 10 Hz in bursts of 29 min and the Nortek operated continuously at 16 Hz; the time series of the Nortek ADV were later downsampled spectrally to 10 Hz for consistency with the Sontek ADVs. All data were time-stamped by the rig's central data logging system. Additionally, three ARGUS-style cameras (Figure 2.2b) recorded images (20 Hz) of the wave field from the wavemaker into the swash zone. These observations were stored in timestacks as the cross-shore pixel intensity averaged over a 50 pixels wide 'alongshore' strip.

2.2.3 Turbulence data processing

The velocity series were quality controlled and despiked based on the guidelines by Elgar et al. (2005) and Mori et al. (2007). Beam velocities were transformed into the ADV's orthog-

Figure 2.2: Instruments during the BARDEXII experiment of which the measurements were used in this chapter, with (a) the rig containing three ADVs and one PT, and (b) three Argus-style cameras.

onal coordinate system, which was subsequently rotated into cross-shore u, 'alongshore' v and vertical w velocities. Positive u is in the shoreward direction, positive v into the sensor perpendicular to the flume and positive w is upward. Further details on the quality control of the ADV measurements applied here are described in Ruessink (2010).

For each run, turbulence velocities u', v' and w' were estimated using the two-sensor filtering technique of Feddersen and Williams (2007), as modified by Gerbi et al. (2009). This method uses adaptive-filtered velocities from a vertically spaced sensor B to estimate the turbulence at sensor A, by subtracting coherent wave motions from the demeaned time series measured by sensor A. Here, sensors A and B can both be either ADV 1, 2 or 3. Turbulent velocities at a specific location can be estimated in two ways, for example at ADV1 using series of either ADV2 or ADV3, denoted 1(2) and 1(3) henceforth. The vertical distance between sensors A and B must be large relative to the turbulent length scale, but small enough to ensure that wave velocities are correlated. This is increasingly complicated closer to the bed, where wave velocities are dampened (Yoon and Cox, 2010). The turbulent length scale is typically between $\sim 0.1 - 0.3h$ beneath breaking waves (e.g., Feddersen, 2012; Govender et al., 2004; Pedersen et al., 1998; Sou et al., 2010). Turbulence velocities u', v' and w' were squared, and after subtracting the Doppler noise variance (3–5 Hz) from each component (Grasso and Ruessink, 2012; Scott et al., 2005), combined into the turbulent kinetic energy as

$$k = 0.5(\overline{u'^2} + \overline{v'^2} + \overline{w'^2}), \tag{2.1}$$

where the overline denotes the average over a run.

When experiments use regular wave series, it is common practice to extract the turbulence velocities by subtracting the ensemble average from the measured time series (Svend-

sen, 1987). The assumption is that the wave orbital motions are equal beneath each wave or wave group, but turbulence is random and is thus not included in the ensemble average. To investigate the accuracy of the two-sensor filtering technique and the difference between turbulence estimates using a large (e.g., 1(3)) and a small (e.g., 1(2)) instrument separation distance, k estimated with both the two-sensor filtering technique and using the ensemble average are compared for a mono- and a bichromatic wave run with values for wave height and period similar to A7 (Table 2.1). Overall, values for k derived with both techniques are of the same order and do show the same vertical structure (Figure 2.3), in agreement with Scott et al. (2005). For the bichromatic case, the estimations with more vertical distance, 1(3) and 3(1), show larger values than the estimations with less vertical distance, 1(2) and 3(2) (Figure 2.3b). This difference can be ascribed to wave bias included in the turbulence time series when the vertical distance between the sensors is larger (Yoon and Cox, 2010). Taking this into account, turbulence was extracted in the remainder of this study using the sensor combinations 1(2), 2(3) and 3(2). The vertical distance between instruments 1 and 2 is 0.26 m, and between 2 and 3 is 0.265 m. Although these distances are with $0.1 - 0.3h$ close to the earlier mentioned turbulence length scale beneath breaking waves, this decision did not notably change the results.

Despite the small vertical distance used in the adaptive filtering, wave bias may still be present in the turbulence time series (Feddersen and Williams, 2007). To further assess the quality of u', v' and w', the cospectra of $\langle u'w' \rangle$ and $\langle v'w' \rangle$ were used (Feddersen and Williams, 2007). The nondimensional cumulative cospectrum (ogive) of $\langle u'w' \rangle$ is defined as

$$Og_{u'w'}(f) = \frac{\int^f Co_{u'w'}(\hat{f})d\hat{f}}{\langle u'w' \rangle}, \tag{2.2}$$
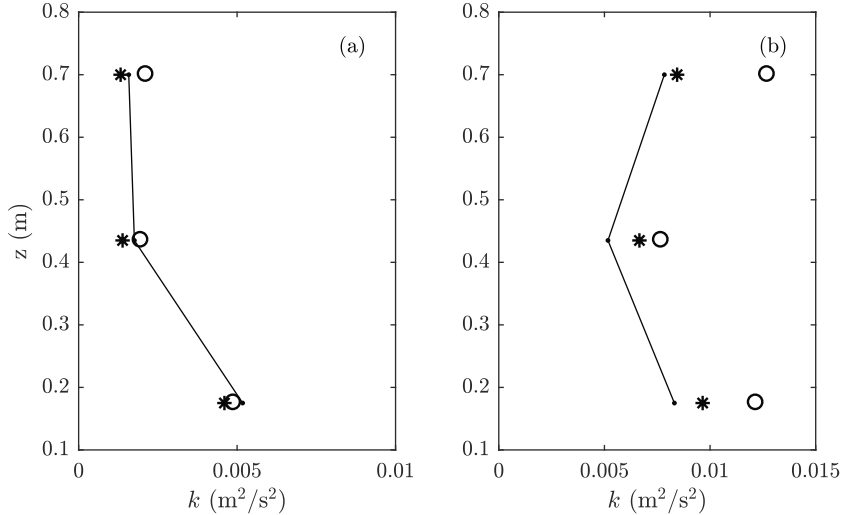

Figure 2.3: Vertical structure of turbulent kinetic energy k for (a) monochromatic and (b) bichromatic run. The turbulent kinetic energy is estimated with the (solid line) ensemble-average and with the two-sensor filtering technique with (circles) large vertical separation between sensors (1(3) and 3(1)) and 2(1) and (asterisks) small vertical separation distance (1(2) and 3(2)) and 2(3).
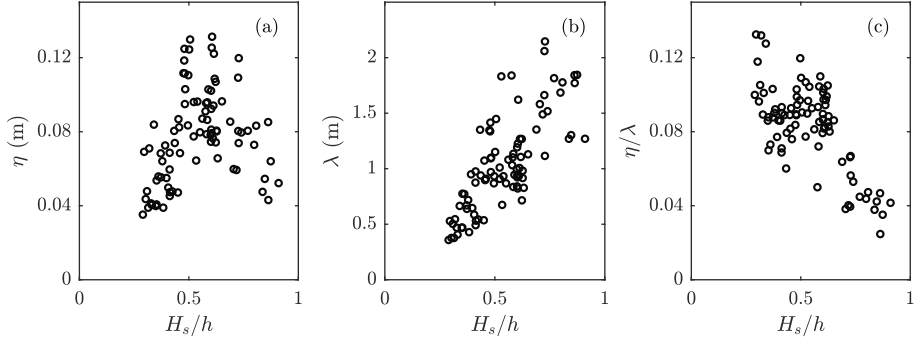
Figure 2.4: Ripple dimensions at the location of the rig ($x = 65$ m): (a) ripple height η, (b) ripple length λ and (c) ripple steepness η/λ versus relative wave height H_s/h.

where $Co_{u'w'}$ is the cospectrum of $u'w'$. The ogive of $v'w'$ is defined similarly. Ogive curves are expected to increase gradually from 0 to 1, sharp increases or fluctuations indicate wave bias. In line with Ruessink (2010), this study rejects measurements where $Og(f)$ of both $u'w'$ and $v'w'$ was not in the range $-0.5 < Og(f) < 1.6$ for all frequencies. In total 35, 39 and 48 runs were selected for further analyses for ADV1, 2 and 3, respectively. For these runs also the turbulence dissipation, ε, was estimated from the $1.5 - 3$ Hz frequency range using the approach of Feddersen et al. (2007) and Gerbi et al. (2009).

2.2.4 Experimental conditions

Morphology

As described more extensively in Ruessink et al. (2016), a sandbar developed near the outer surf zone during series A1 ($x \approx 69$ m), and remained approximately unaltered to the end of series A4. During the following series (A6 – A8), low-steepness waves resulted in the onshore migration and subsequent disappearance of the sandbar, and the development of a berm on the upper beach. During tests B and C, a horizontal platform formed between $x \approx 70 - 85$ m, while the remainder of the profile was fairly stable. The overwash during series D and E resulted in barrier destruction.

Ripples

The bed state, i.e. ripple characteristics, at the location of the rig was determined using the measurements from the mechanical bed profiler. As described in detail in Ruessink et al. (2015), for each surveyed bed profile the small-scale wave ripples were separated from the large-scale bar and berm using a scale-controlled interpolator (Plant et al., 2002). A 10 m long stretch of ripple data, centred around the rig, was processed with the approach of Masselink et al. (2007) into an estimate of ripple length and height for each survey. Results for a shorter stretch (5 m) were similar but more scattered. The ripple height ranged from 0.02 – 0.16 m, where the highest ripples were found where the relative wave height was in the range 0.45 – 0.65 (Figure 2.4a). The ripple length increased linearly with relative wave height (H_s/h, Figure 2.4b). Ripple steepness ranged from ~ 0.12 for low relative wave height to ~ 0.02 under breaking waves (Figure 2.4c). Observations with a 3D profiling sonar, collected seaward of the rig at $x = 63.1$ m, illustrate that the ripples were strongly three-dimensional during series A and B and more two-dimensional during D and E (Ruessink et al., 2015).

Hydrodynamic zones

The different offshore wave and water level conditions (Table 2.1) resulted in a variety of wave conditions at the rig. We divided these conditions into three classes: (1) pre-shoaling and shoaling without wave breaking, (2) shoaling with occasional wave breaking, and (3) breaking (surf zone). The criteria to divide the test runs into these classes were based on H_s/h, the wave shape and the fraction of broken waves, Q_b. As waves propagate into shallower water, their shape change from near-sinusoidal to peaked (skewness) and pitched forward (asymmetry). As such, the skewness and asymmetry are valuable parameters to determine the cross-shore position in terms of hydrodynamic processes. The skewness and asymmetry were calculated as:

$$Sk = \frac{\langle \eta_{hf}^3 \rangle}{\langle \eta_{hf}^2 \rangle^{3/2}}, \tag{2.3}$$

$$As = \frac{\langle (H(\eta_{hf}))^3 \rangle}{\langle \eta_{hf}^2 \rangle^{3/2}}, \tag{2.4}$$

where η is the sea surface time series and H is the Hilbert transform. At the rig, Sk ranged from 0 to 1.0 and As from 0 to -1.5 (Figure 2.5a). These values are larger than those measured during comparable conditions in the field (e.g., Grasso et al., 2012; Ruessink et al., 2012a), explained by the lack of directional spread and therefore stronger energy-transfers to higher harmonics in a laboratory flume (e.g., Grasso et al., 2011). The fraction of broken waves (Q_b) at the location of the rig was determined by marking wave breaking locations manually on the video timestacks (Figure 2.6). The Q_b at the rig was calculated as the number of waves breaking seaward of the rig divided by the total number of waves, resulting in Q_b ranging
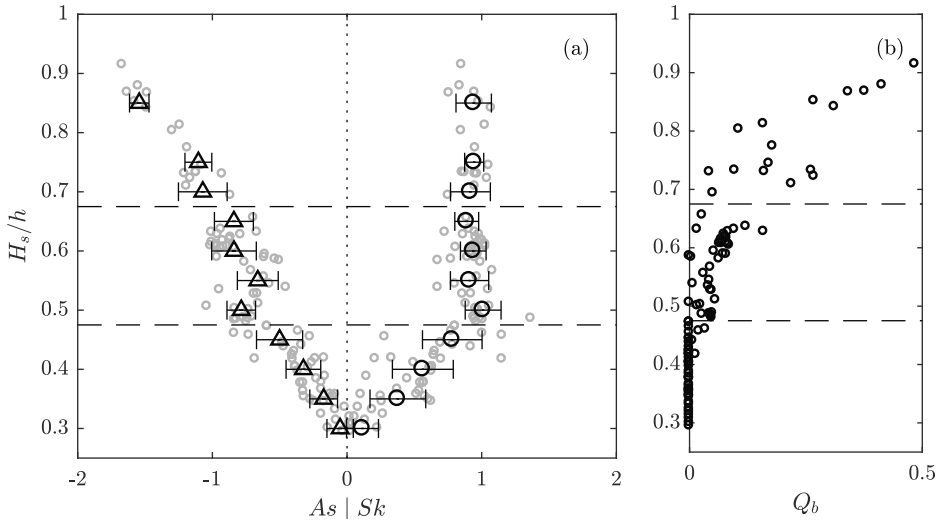
Figure 2.5: Wave characteristics at the location of the rig, with (a) asymmetry *As* and skewness *Sk* and (b) fraction of broken waves Q_b versus relative wave height H_s/h. The grey circles in (a) show observed values for the *Sk* and *As*, the triangles (*As*) and circles (*Sk*) are the H_s/h bin-averaged values with a bin width of 0.05. The error bars are $\pm$ the standard deviation within each bin. The dashed horizontal lines represent the chosen values to divide the cases in nonbreaking, occasional breaking and breaking (surf zone).

from 0 to 0.48 (Figure 2.5b). Both the wave shape and Q_b scale with H_s/h (Figure 2.5), which makes this a suitable parameter to classify the runs.

The observations under pre-shoaling and shoaling waves were recognised as where the skewness and asymmetry are increasing with H_s/h, but Q_b is still zero. This is valid for $H_s/h < 0.475$ (Figure 2.5). Sk remains constant for $H_s/h > 0.475$, while $|As|$ increases linearly. The test series with shoaling waves and occasional wave breaking at the rig is recognised for $|As| < Sk$, while Q_b is below 0.15. This is valid for $0.475 < H_s/h < 0.675$. Test series were classified as the surf zone when $|As| > Sk$, valid for $H_s/h > 0.675$. The number of runs in these classes is 15 (18, 20), 7 (16, 21) and 13 (5, 7) for ADV1 (ADV2, ADV3), respectively. The vast majority of waves were observed to break as plunging breakers. An occasional wave plunged immediately from the wavemaker and propagated as a bore through the entire flume.
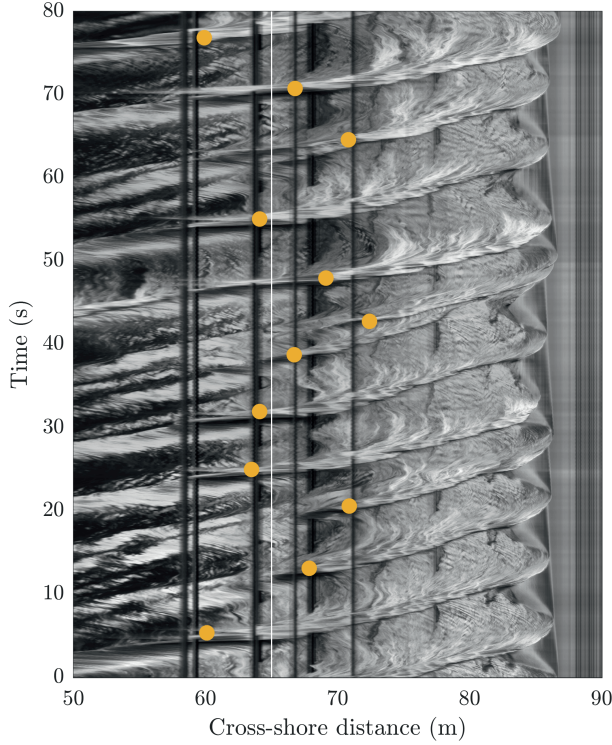
Figure 2.6: An example of a cross-shore timestack of pixel intensity, collected during run 2 of test series C1. The white vertical line indicates the location of the rig and yellow dots are the manually detected location of wave breaking.

2.3 Results

Class-averaged turbulence characteristics are analysed with both the Froude-scaled turbulent kinetic energy $\sqrt{k/gh}$ and the turbulence dissipation ε (Figures 2.7a,b). The magnitude of $\sqrt{k/gh}$ increases with relative wave height (Figure 2.7a). The two classes with nonbreaking and occasional-breaking conditions show an increase in $\sqrt{k/gh}$ towards the bed. This can be attributed to bed-generated turbulence and is certainly enhanced by the observed ripples (Section 2.2.4). It must be noted, however, that the three ADVs were all located in the lower half $(0.1 - 0.5h)$ of the water column for these conditions and that the potential near-surface increase in $\sqrt{k/gh}$ in the class with occasional wave breaking may have been missed. The vertical turbulence profile in the surf zone shows larger values throughout the water column and becomes relatively uniform. The same conclusions can be drawn from vertical profiles of ε (Figure 2.7b) and illustrates that k and ε can be used interchangeably to study the vertical turbulence profile.

The cross-shore transport of turbulence by wave velocities relates to sediment transport as turbulent vortices keep sand in suspension. The intrawave variability in $\sqrt{k/gh}$ indicates whether the majority of turbulence is transported by waves in the onshore or the offshore direction. To investigate intrawave variability for both short waves and infragravity waves, the timeseries of cross-shore velocity (u) were frequency filtered for short-wave (u_{hf}, $0.05 < f < 0.5\ Hz$) and infragravity-wave motion (u_{lf}, $0.005 < f < 0.05\ Hz$). The instantaneous wave phase was calculated for both timeseries using the Hilbert transform, and $\sqrt{k/gh}$ was then averaged into 0.2π wide bins. These phase-averaged quantities were grouped and averaged based on H_s/h, in the classes nonbreaking ($H_s/h < 0.475$) and breaking ($H_s/h > 0.675$). Turbulence intensities beneath nonbreaking waves are largest close to the bed and decrease rapidly towards the water surface during all wave phases (Figure 2.8a). The largest values for $\sqrt{k/gh}$ are present after reversal from offshore to onshore flow, when the orbital velocity is in the onshore direction. This intrawave variability is probably caused by vortex shedding (van der Werf et al., 2007), as ripples with a steepness up to 0.12 were observed (Section 2.2.4). When waves are breaking, $\sqrt{k/gh}$ is larger throughout the water column during all phases (Figure 2.8b), indicating a large degree of vertical mixing. Near the surface ($z \sim$
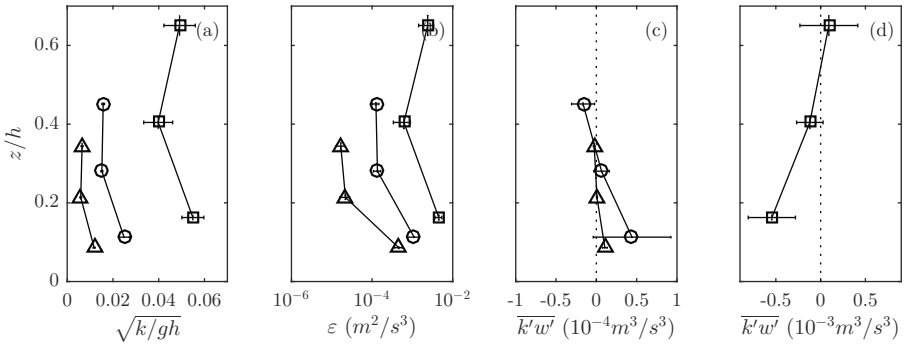
Figure 2.7: Mean values of (a) Froude-scaled turbulent kinetic energy $\sqrt{k/gh}$, (b) turbulence dissipation ε and (c-d) vertical turbulent flux $\overline{k'w'}$, versus vertical position relative to water depth h. The different symbols represent the classes (triangles) $H_s/h < 0.475$, (circles) $0.475 < H_s/h < 0.675$ and (squares) $H_s/h > 0.675$. Vertical and horizontal brackets are $\pm$ the standard error of the mean. Note there is a factor ten difference between the (c) and (d).
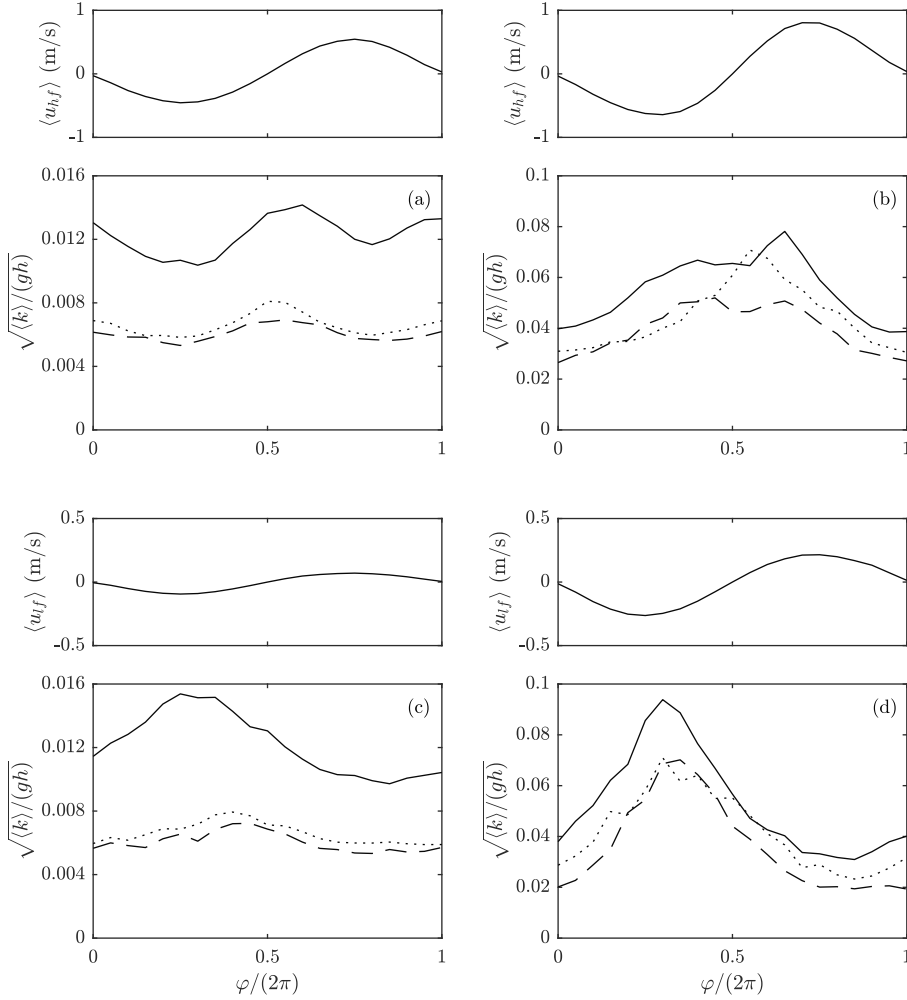
Figure 2.8: Intrawave variability of $\sqrt{k/gh}$ for (a,c) nonbreaking and (b,d) breaking waves within (a,b) short wave orbital motion and (c,d) infragravity motion. The three lines represent the froude-scaled turbulence at (solid line) 0.175 m, (dashed line) 0.435 m and (dotted line) 0.7 m above the bed. The plots above each subplot denote phase-averaged u_{hf} or u_{lf} over all waves used in the analysis.

$0.7h$), $\sqrt{k/gh}$ is largest during flow reversal from offshore to onshore u_{hf}, while near the bottom, $\sqrt{k/gh}$ is largest when u_{hf} is maximum onshore. This phase-lag between turbulence near the surface and near the bottom could indicate downward transport of surface-induced turbulence, although the position of the peak value measured by the middle ADV suggests a more complicated situation. The peak in turbulence near the water surface at $\phi/(2\pi) \approx 0.5$ indicates that the plunging jet of the breaking waves injects turbulence at the wave front, similar to observations beneath regular plunging waves (Ting and Kirby, 1995).

Beneath both nonbreaking and breaking waves, $\sqrt{k/gh}$ is also modulated on an infragravity time scale (Figures 2.8c and d), with large $\sqrt{k/gh}$ when u_{lf} is in the offshore direction. This

phase-coupling can be explained by the presence of the highest short-waves in the trough of the infragravity waves. Beneath nonbreaking waves this means larger wave-orbital velocities and presumably stronger vortex shedding from the ripples. The time series with breaking waves were collected in the outer surf zone, where only the highest waves break. At the location of the rig, approximately two thirds of the broken waves were observed while u_{lf} was in the offshore direction, giving rise to the observed infragravity modulation of $\sqrt{k/gh}$.

Returning to Figure 2.7, the vertical turbulence profile was also analysed with the time-averaged vertical turbulence flux, $\overline{k'w'}$ (Figures 2.7c and d). Negative (positive) $\overline{k'w'}$ signify the majority of the turbulence events traveling downward (upward). These directions indicate whether turbulence is dominantly surface-generated (downward) or bed-generated (upward). The dominance of bed-generated turbulence for nonbreaking and occasional breaking waves is confirmed by positive $\overline{k'w'}$ close to the bed (Figure 2.7c). The class with occasional wave breaking additionally shows a negative vertical turbulence flux near the surface, illustrating the downward flux of turbulence by the plunging breakers in these time series. The vertical profile and magnitude of the turbulence flux of this class is similar to field observations above a rippled bed described in Grasso and Ruessink (2012). Negative $\overline{k'w'}$ in the surf zone (Figure 2.7d) suggests downward traveling turbulence as dominant close to the bed, thus the large $\sqrt{k/gh}$ values observed close to the bed are not necessarily related to bed-induced turbulence. Although $\overline{k'w'}$ values are small in the surf zone in the upper part of the water column (Figure 2.7d), large instantaneous upward and downward turbulent fluxes were measured. This might be attributed to the presence of horizontal vortices in the upper part of the water column beneath plunging breakers (Figure 1.1; Zhang and Sunamura, 1990). The horizontal vortices may result in large instantaneous turbulence fluxes but cancel out in a time-average sense.

2.4   Discussion

The range in $\sqrt{k/gh}$ observed in the surf zone (0.02 – 0.06) agrees with earlier large-scale experiments with irregular plunging waves (Yoon and Cox, 2010), although $\sqrt{k/gh}$ close to the bed is larger in our observations. The latter is presumably related to the wave-induced ripples observed here (Figure 2.4), while flat-bed conditions presumably dominated in the experiment of Yoon and Cox (2010) given the smaller grain size. The observed Froude-scaled turbulence is larger than found during field observations with both plunging breakers and bores (0.02 – 0.04, Ruessink (2010)), which might depend on wave conditions and the cross-shore location of the rig, and is low in comparison with regular plunging waves in the laboratory (0.06 – 0.12, Mocke (2001)). Our dataset lacks, however, observations with $Q_b > 0.5$. It is expected that k near the water surface further increases and k near the bed becomes less important as Q_b increases and the ripple steepness reduces.

The direction of turbulence transport by infragravity waves may depend on the horizontal location in the surf zone. Ting (2001) and Ting (2002) measured a net offshore directed transport by infragravity waves beneath spilling breakers in the outer surf zone. This reversed to the onshore direction in the inner surf zone, where short-waves are depth-saturated and can only reach shallower water on the crest of infragravity waves (e.g., Janssen et al., 2003; Tissier et al., 2013). Our dataset lacks observations in the inner surf zone and we cannot confirm the change in the direction of turbulence transport induced by infragravity waves.

In many small-scale experiments (e.g., Ting and Kirby, 1994; Ting and Kirby, 1995; Kimmoun and Branger, 2007; Sou et al., 2010; Govender et al., 2011; Henriquez et al., 2014), tur-
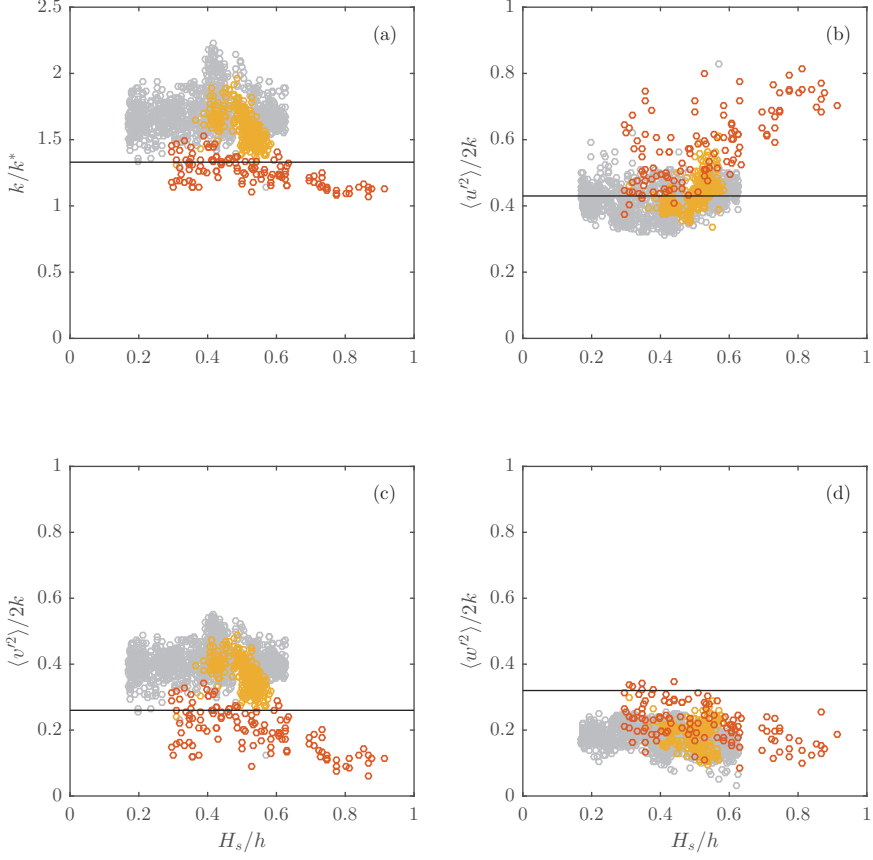
Figure 2.9: Distribution of (a) k/k^*, (b) $\langle u'^2 \rangle/2k$, (c) $\langle v'^2 \rangle/2k$ and (d) $\langle w'^2 \rangle/2k$ versus relative wave height H_s/h from (red) BARDEXII observations, (gray) Ameland (Ruessink et al., 2012b) and (yellow) Truc Vert (Ruessink, 2010). The solid lines show the values for plane wake turbulence (Svendsen, 1987)

bulence is measured in high detail in two directions, u' and w'. To account for the lack of having v' measurements in the total turbulent kinetic energy, k is often estimated as $k = 1.33k^*$, with $k^* = 0.5\left(\langle u'^2 \rangle + \langle w'^2 \rangle\right)$. The ratio between k and k^* is based on the assumption of plane wake turbulence in the surf zone, as proposed by Svendsen (1987), for which the ratio between $\langle u'^2 \rangle : \langle v'^2 \rangle : \langle w'^2 \rangle$ is 0.42 : 0.26 : 0.32. Our observations are compared with these ratios in Figure 2.9. Observations are close to $k = 1.33k^*$ and thus support the assumption of plane wake turbulence in the surf zone. The ratios between the different turbulence components, however, differ from the values for plane wake turbulence with an increasing relative wave height. The cross-shore component of the turbulence, $\langle u'^2 \rangle/2k$, increases with H_s/h and is particularly larger than the plane wake value in the surf zone ($H_s/h > 0.675$). For example for $0.7 < H_s/h < 0.9$, $\langle u'^2 \rangle : \langle v'^2 \rangle : \langle w'^2 \rangle$ is 0.71 : 0.12 : 0.17.

Ruessink (2010) also described the deviation from plane wake turbulence of observations during field campaigns at Truc Vert Beach (beach slope 1:40, France) in 2008 and at Ameland (beach slope 1:80, The Netherlands) in 2010 (Ruessink et al., 2012b); both datasets are added to Figure 2.9. For the field datasets, the ratio k/k^* is about 1.6, due to the higher impor-

tance of v' (Figure 2.9c). While the Ameland observations show weak correlation between $\langle v'^2 \rangle / 2k$ and the mean alongshore current $(\bar{v})$, this does not explain the difference with plane wake turbulence. It seems the plane wake assumption holds for turbulence beneath shoaling and occasional breaking waves in a laboratory flume, but not for field observations. In the field, the longshore turbulence component might be enhanced by wave directional spreading. The difference between the datasets can also be caused (or enhanced) by the breaker type and its associated orientation of the turbulent vortices. The Ameland dataset consisted of spilling breakers, Truc Vert of both plunging breakers and bores, and BARDEXII of plunging breakers only. Beneath plunging breakers, the turbulence is organised in vortices with an alongshore rotation axis, enhancing u' and limiting v' (Nadaoka et al., 1989; Zhang and Sunamura, 1990), whereas beneath spilling breakers mainly oblique descending eddies are present with turbulence in all axes. This might explain (part of) the difference in $\langle v'^2 \rangle / 2k$ between the different datasets, and the increase in $\langle u'^2 \rangle / 2k$ with the fraction of breaking waves in the BARDEXII and Truc Vert datasets. The vertical turbulence component is in the same range for all datasets and is constant with H_s / h.

2.5   Conclusions

The vertical turbulence structure in the shoaling and surf zones of a field-scale laboratory beach was studied. The cross-shore variation in the vertical structure provides insight into the importance of surface-induced turbulence, relative to bed-induced turbulence, in the different hydrodynamic zones. Seaward of the surf zone, the turbulence structure was dominated by bed-induced turbulence. The Froude-scaled turbulence was largest close to the bed during flow reversal of the wave orbital motion from negative to positive, possibly explained by the shedding of turbulent vortices by vortex ripples during flow reversal. In the surf zone, Froude-scaled turbulence was largest beneath the front of the waves, where the plunging jets of the breaking waves inject turbulence into the water column. In addition, for both non-breaking and breaking waves, Froude-scaled turbulence was modulated on the group scale, with largest values when u_{lf} was in the offshore direction. Turbulence is both generated at the surface and at the bed, but surface-induced turbulence is of increasing importance with the fraction of breaking waves.

Chapter 3

Intrawave sand suspension

Abstract

Short-wave sand transport in morphodynamic models is often based solely on the near-bed wave-orbital motion, thereby neglecting the effect of ripple-induced and surface-generated turbulence on sand transport processes. Here, sand stirring was studied using measurements of the wave-orbital motion, turbulence, ripple characteristics and sand concentration collected on a field-scale laboratory beach under conditions ranging from irregular nonbreaking waves above vortex ripples to plunging waves and bores above subdued bed forms. Turbulence and sand concentration were analysed as individual events and in a wave phase-averaged sense. The fraction of turbulence events related to suspension events is relatively high ($\sim 50\%$), especially beneath plunging waves. Beneath nonbreaking waves with vortex ripples, the sand concentration close to the bed peaks right after the maximum positive wave-orbital motion and shows a marked phase lag in the vertical, although the peak in concentration at higher elevations does not shift to beyond the positive to negative flow reversal. Under plunging waves, concentration peaks beneath the wavefront without any notable phase lags in the vertical. In the inner-surf zone (bores), the sand concentration remains phase coupled to positive wave-orbital motion, but the concentration decreases with distance toward the shoreline. On the whole, our observations demonstrate that the wave-driven suspended load transport is onshore and largest beneath plunging waves, while it is small and can also be offshore beneath shoaling waves. To accurately predict wave-driven sand transport in morphodynamic models, the effect of surface-generated turbulence beneath plunging waves should thus be included.

3.1 Introduction

Short (sea or swell, 2–20 s) waves are an important sand stirring agent in the nearshore zone and largely determine the amount of suspended sand available for transport by other hydrodynamic processes, such as infragravity waves and mean currents. When sand is predominantly suspended during a particular phase of the orbital motion, short waves can also transport sand themselves e.g., Jaffe et al., 1984. While short-wave sand transport beneath nonbreaking waves on a plane bed (i.e., sheetflow conditions) is reasonably well understood from extensive laboratory experiments, ripple-induced and surface-generated turbulence effects have not received much attention. Both can strongly affect the phase coupling between sand suspension and the wave-orbital motion in natural shoaling and surf zones, respectively. These effects are not yet represented in current morphodynamic models (e.g., van Rijn et al., 2013; Dubarbier et al., 2015) and are the focus of this chapter.

In the absence of a mean cross-shore current, nonzero shortwave-induced sand transport Q_{hf} under sheet flow conditions demands the orbital motion to be nonlinear. As waves propagate toward the beach into shallower water, they become skewed (high narrow crests and low wide troughs) in the shoaling zone and asymmetric (pitched forward) in the surf zone. This shape transition leads to analogous changes in the near-bed orbital motion. Experiments with skewed flow velocities in oscillatory flow tunnels (e.g., King, 1991; Ribberink and Al-Salem, 1994; O'Donoghue and Wright, 2004) have illustrated that these flows drive positive (i.e., "onshore") sand transport when the median grain size D_{50} is coarser than $\sim$ 200 μm, as the higher positive velocities are capable of mobilizing larger amounts of sand (e.g., Ribberink and Al-Salem, 1994) than the lower negative velocities. For finer sand, the sand has not all settled at the time of flow reversal from positive to negative directed and may therefore be transported by the negative flow. These phase-lag effects can cause Q_{hf} to become negative, i.e., "offshore" directed (Dohmen-Janssen et al., 2002; O'Donoghue and Wright, 2004; Grasso et al., 2011). Below velocity-asymmetric flow, maximum positive and negative velocities are equal in magnitude; however, flow tunnel experiments show these flows still drive sand transport in the positive direction (e.g., van der A et al., 2010; Grasso et al., 2011; Ruessink et al., 2011). The net positive-directed transport of sand by velocity-asymmetric flows can be explained by two effects. First, the time between the maximum positive velocity and the positive-negative flow reversal is longer than the time between the maximum negative and the negative-positive flow reversal. This means that sand suspended during the maximum negative velocity has less time to settle prior to flow reversal and is prone to be moved in the positive direction. Numerical simulations by Ruessink et al. (2009) indicate that this effect only contributes to the net transport when $D_{50} \lesssim 250$ μm. Second, the high acceleration from negative to positive flow induces high bed shear stresses (Nielsen, 1992), as the boundary layer has limited time to grow, in comparison with a longer time span and low acceleration during the change from positive to negative flow. This causes the suspension peak during positive flow to just exceed that during negative flow (Ruessink et al., 2011), and thus, Q_{hf} is small but positive.

The presence of ripples in the sea bed complicates the short-wave sand transport considerably. Measurements by Ribberink and Al-Salem (1994) in an oscillatory flow tunnel showed a reduction in the positive-directed suspended sand transport in the presence of ripples. Several other laboratory (e.g., van der Werf et al., 2007) and field (e.g., Osborne and Vincent, 1996) studies showed that steep vortex ripples can even cause a reversal in the net transport direction to offshore (see also Aagaard et al. (2013)). This influence of vortex ripples is caused by turbulent vortices that are ejected from the ripple crests during flow reversal. During positive flow velocities, a vortex is formed at the lee side of the ripple crest, which detaches from

the bed during flow reversal from positive to negative velocities, and is subsequently ejected into the water column during the negative flow phase. This phenomenon also occurs during the negative-positive flow reversal, but due to the higher positive velocities under velocity-skewed flows the ejected vortex at positive-negative flow reversal is larger and, as a result, suspended sand is transported in the net negative direction. The sand concentration above vortex ripples is thus both variable in time and space, and suspended transport estimates highly depend on the location with respect to the ripple crest (e.g., Osborne and Vincent, 1996; Thorne et al., 2003; van der Werf et al., 2007).

Surface-generated turbulence injected by breaking waves is another mechanism that can affect the phase coupling between sand suspension and orbital flow. Depending on the breaker type and the stage of breaking, turbulence is organised in obliquely descending eddies (ODEs), horizontal vortices, or both (Nadaoka et al., 1989; Zhang and Sunamura, 1990). ODEs, which are observed beneath spilling breakers and bores (Zhang and Sunamura, 1990), intermittently descend toward the bed and suspend sand (Nadaoka et al., 1988). Yoon and Cox (2012) found that 20 – 35% of the turbulence events beneath spilling breakers resulted in a suspension event and concluded that most of the turbulence dissipated before it reached the bed. These events did, however, explain 50 – 65% of the observed suspension events. The turbulence field beneath plunging breakers is characterised by an injection of turbulence at the plunge point, the location where the plunging jet hits the water surface, and the formation of large-scale horizontal vortices at the wavefront. These turbulent structures are more effective in stirring sand from the bed than the vortices beneath spilling breakers (e.g., Beach and Sternberg, 1996; Aagaard and Hughes, 2010). Moreover, the large-scale horizontal vortices enable the sand to be mixed throughout the water column. Whether the additional sand stirred from the bed by wave breaking induced turbulence affects the magnitude or direction of the short-wave sand transport depends on the timing of sand stirring in respect to the wave phase. Several studies suggest that sand stirring in the surf zone becomes unrelated with the wave-orbital motion and Q_{hf} thus reduces to zero (Sato et al., 1990; Barkaszi and Dally, 1992; Nadaoka et al., 1988). Other laboratory and field studies suggest, however, that Q_{hf} in the surf zone can either be positive (e.g., Jaffe and Sallenger Jr., 1992; van Thiel de Vries et al., 2008; Aagaard and Hughes, 2010) or negative (e.g., Scott et al., 2009).

The main goal of this study is to gain more insight in the effect of the surface-generated turbulence on sand suspension beneath plunging breaking waves. More specifically, the steps are (1) to quantify the effectiveness of turbulence events in stirring sand from the bed and (2) to determine the phase coupling of sand suspension to the wave-orbital motion, beneath nonbreaking waves, plunging breaking waves and bores. Understanding this effect is crucial to be able to predict sand transport by short waves in the surf zone and to eventually improve morphodynamic models. In this study, field-scale flume measurements collected during the Barrier Dynamic Experiment II (BARDEXII) were used. This experiment gave us the opportunity to simulate field-like conditions, with the advantage of more detailed measurements (i.e., more sensors and very detailed bed surveys) and more control over instrument heights. The first mentioned goal was approached by determining the fraction of related turbulence and suspension events. To reach the second goal, the focus was on the timing of sand suspension in the wave-orbital motion as this largely determines the magnitude and direction of the short-wave transport. This chapter is structured as follows. In section 3.2 the laboratory experiments, data processing, and analysis procedures are described. Subsequently, in section 3.3, the results from the event-based approach and the wave phase-based approach are presented. A discussion of the results is found in section 3.4 and the main conclusions of our work are provided in section 3.5.
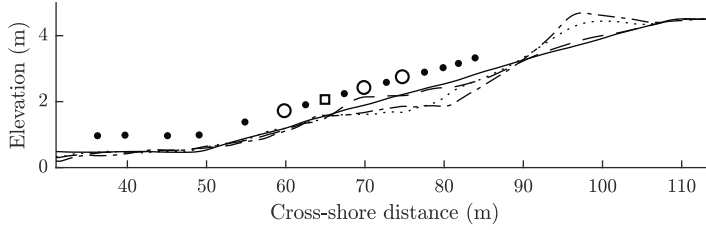
Figure 3.1: The (solid) initial profile and profiles after (dashed line) A4, (dotted line) A8 and (dash-dotted line) C2. The location of the instrument rigs, (square) TR and (circles, numbered in positive x-axis direction) R1, R2, and R3 are indicated, as well as the location of the (dots) individual pressure transducers.

3.2 Methods

3.2.1 Data collection

The Barrier Dynamic Experiment II (BARDEXII) was conducted in the Delta flume in Vollenhove, The Netherlands, in 2012 (Masselink et al., 2016). The initial bed profile consisted of a 4.5 m high, 5 m wide and 75 m long sandy (median grain diameter D_{50} = 430 μm, mean grain size = 510 μm) barrier. The initial beach slope was 1:15 from x = 49 m to x = 109 m, where x = 0 m is the wave maker (Figure 3.1). The experiment consisted of five series (A – E) that were divided into tests with different wave and/or water level conditions. Each test was subsequently divided into wave-runs with a duration of 15 – 180 min; between runs the bed level along the entire flume was surveyed (Ruessink et al., 2016). This study focuses on the tests that were designed to study surf-swash dynamics, i.e., tests A1 – C2. During these tests, irregular waves with test-dependent offshore significant wave height H_s and peak period T_p (Table 3.2.1) were forced using a JONSWAP spectrum. During series A, the beach profile was first (A1 – A4) subjected to erosive waves (H_s = 0.8 m, T_p = 8 s), causing sand to be eroded from the inner-surf zone to form a sandbar in the outer-surf zone (Ruessink et al., 2016). In the second part (A6 – A8), accretive waves (H_s = 0.6 m, T_p = 12 s) resulted in the migration of the sandbar in the onshore direction, until it eventually merged with the beach face to form a steep (1:6) berm (Ruessink et al., 2016). Series B consisted of two tests with a different water level (ζ = 3 and ζ = 2.5 m, where ζ refers to the height of the still water above the concrete flume floor). In series C a tidal cycle was simulated by raising (C1) and subsequent lowering (C2) of the water level in steps of maximum 0.2 m between wave runs. The sandbar remained relatively stable during series B and C (Ruessink et al., 2016), see also Figure 3.1.

Concurrent suspended sand concentration and velocity measurements, of which the latter suitable to quantify turbulence characteristics, were collected using a rig deployed at x = 65 m (Figure 3.1). The Turbulence-Rig (TR hereafter) contained three sideways oriented Ocean Acoustic Doppler Velocimeters (ADVs) measuring flow velocity in all directions at 10 Hz, a vertical array of 7 Seapoint Turbidity Meters (STMs) to estimate suspended sand concentrations (4 Hz) and a Pressure Transducer (PT) to sample near-bed pressure (4 Hz). The height of the rig was manually adjustable, ensuring an equal height of the instruments above the bed at the start of each wave run (0.175, 0.435, and 0.7 m for ADV1-3; 0.04, 0.07, 0.10, 0.14, 0.17, 0.44 and 0.71 m for STM1-7; and 0.25 m for the PT). The horizontal distance between the instruments and the nearest flume wall was around 2 m.

Additional velocity and suspension data were collected using three rigs (R1, R2, and R3) at x = 60, x = 70, and x = 75 m (Figure 3.1). These rigs contained an electromagnetic flow

Table 3.1: Hydrodynamic conditions A-C during the BARDEXII experiment.

Test	H_s (m)	T_p (s)	ζ (m)	Q_b ($x =$65 m)
A1	0.89	8	3	0.07
A2	0.88	8	3	0.09
A3	0.88	8	3	0.07
A4	0.88	8	3	0.11
A6	0.69	12	3	0.01
A7	0.77	12	3	0.05
A8	0.77	12	3	0.04
B1	0.89	8	3	0.03–0.08
B2	0.87	8	2.5	0.17–0.26
C1	0.88,0.55	8	2.25–3.65	0.41–0
C2	0.55,0.90	8	3.53–2.25	0–0.48

meter at $z \approx 0.11$ m to measure flow velocities in the cross-shore and alongshore directions, a vertical array of 3 STMs ($z \approx 0.04$, 0.06, and 0.11 m) and a PT ($z \approx 0.25$ m). Although turbulence could not be estimated at these locations, these measurements do enable us to analyse the phase coupling between the orbital motion and sand concentration at multiple cross-shore locations. Pressure transducers were also deployed individually at nine locations (Figure 3.1).

The bed elevation was measured using a mechanical bed profiler (cross-shore resolution of 0.01 m) in between each wave run along the centerline of the flume to quantify both the large-scale bar-berm and small-scale wave ripple morphology. Additionally, a 3-D Profiling Sonar was deployed at $x = 63.1$ m to obtain circular elevation models of small-scale bed forms in between wave runs and information on ripple migration during the runs (Ruessink et al., 2015). Moreover, three Argus type cameras were deployed (Masselink et al., 2016) to collect information on the location of wave breaking. The pixel intensity along the centerline of the flume was averaged over a 50 pixel wide "alongshore" strip and subsequently collected in a timestack. It was chosen to average over a certain amount of pixels rather than a fixed part of the flume width, as the purpose was to reduce pixel noise (the water surface is considered homogeneous over the width of the flume).

3.2.2 Data Processing

Instantaneous pressure time series were converted to water surface elevation using linear wave theory. The water depth (h) was calculated as the sum of the instrument height above the bed with the mean of the pressure time series. The instantaneous water surface elevation was bandpass filtered to obtain the short-wave part (η_{hf}) with $0.05 < f < 1$ Hz and processed into the significant short-wave height (H_s). The nonlinearity of the short waves was, as described in Chapter 2, expressed with the skewness (Sk) and asymmetry (As) as:

$$Sk = \frac{\langle \eta_{\text{hf}}^3 \rangle}{\langle \eta_{\text{hf}}^2 \rangle^{3/2}},$$

(3.1)

$$As = \frac{\langle (H(\eta_{\text{hf}}))^3 \rangle}{\langle \eta_{\text{hf}}^2 \rangle^{3/2}},$$

(3.2)

where H denotes the Hilbert transform (Elgar, 1987).

The velocity series from the ADVs were quality controlled and despiked based on the guidelines provided in Elgar et al. (2005) and Mori et al. (2007). Beam velocities were transformed into the ADV's orthogonal coordinate system and subsequently rotated into cross-shore u, alongshore v (wall to wall) and vertical w velocities. Positive u is in the shoreward direction, positive v is into the sensor perpendicular to the flume, and positive w is upward. Further details on the quality control measures applied on the velocity measurements are described in Ruessink (2010). The turbulence velocities u', v', and w' were estimated using the two-sensor filtering technique developed by Feddersen and Williams (2007) and modified by Gerbi et al. (2009). This method uses adaptive-filtered velocities from a vertically spaced sensor B to estimate the turbulence at sensor A, denoted A(B), where A and B can be ADV 1, 2 or 3. To reduce bias in the turbulence velocities due to wave damping near the bed, the sensor combinations with a relatively small vertical separation distance 1(2), 2(3), and 3(2) were chosen for the two-sensor filtering technique (see Chapter 2). The turbulence velocities were combined into the instantaneous turbulent kinetic energy as

$$k = 0.5(u'^2 + v'^2 + w'^2). \tag{3.3}$$

The STMs were postcalibrated in a recirculation tank using sand samples collected at the locations of the instrument rigs at the end of the experiment. The output of the instruments correlated quadratically with the sand concentration over the range 0–40 kg/m³ ($r^2 \geq 0.99$ for all instruments). Small background concentrations were removed by subtracting the 0.5 percentile in blocks of 15 min. Concentration signals that indicated instrument burial in the bed or the presence of bubbles were rejected. Air bubbles beneath breaking waves and surf zone bores can have a significant effect on measurements recorded by optical instruments (Puleo et al., 2006). In the time series these bubbles can be recognised as a steep spike in concentration, often occurring prior to an actual sand suspension event. Time series were rejected when a cross correlation with the concentration signal at a lower sensor resulted in a negative phase-lag, i.e., when concentration peaked earlier at a higher than lower sensor, and when the mean in sand concentration decreased toward the bed (e.g., Aagaard and Jensen, 2013).

Ripples were separated from the large-scale morphology by applying a second-order loess interpolator (Plant et al., 2002) with $l_x = 3.5$ m. This acts as a high-pass filter and removes variability with length scales larger than $l_x/0.7$ (i.e., 5 m). The cross-shore ripple statistics, ripple height (η_r), ripple length (λ_r) and ripple steepness ($\vartheta_r = \eta_r/\lambda_r$) were calculated every 0.5 m from overlapping (95%) windows with a length of 10 m. As this approach occasionally resulted in unrealistically large variations in ripple statistics in especially the breaker zone, the statistics were low-pass filtered with $l_x = 3.5$ m. The computation of ripple statistics from the collected bed profiles was described in more detail by Ruessink et al. (2015).

The video timestacks were used to identify the location where individual waves were breaking, as this is clearly visible in timestacks due to the white foam that is generated shortly after a plunging jet hits the water surface. The fraction of broken waves (Q_b) was consequently determined at the location of each instrument rig and for each wave run, as the number of broken waves at these locations divided by the total number of waves (see Chapter 2 for further details).

3.2.3 Data analysis

Related events

Turbulence measurements from the lowest ADV ($z \approx 0.175$ m) and the concentration measurements from the lowest five STMs at TR were used for the event analysis. Measurements were cut into 15 min long blocks to ensure an equal length for all time series. The readings from the lowest five STMs were combined into an instantaneous suspended load by integrating the time series, using the trapezoidal method, over the vertical distance from the lowest sensor ($z \approx 0.04$ m) to the fifth sensor ($z \approx 0.17$ m) (Butt et al., 2004; Puleo, 2009; Yoon and Cox, 2012):

$$C = \int_{0.04m}^{0.17m} c(z) \, \mathrm{d}z, \tag{3.4}$$

where $c(z)$ is the measured sand concentration at height z above the bed. A 2 s moving average filter was applied to smoothen both instantaneous k and C as to make the event statistics more robust. Subsequently, moderate and intense events were identified in the k and C series. Moderate k events were identified where k exceeded $\bar{k} + \sigma$, where $\bar{k}$ is the block mean and σ is the standard deviation, but did not exceed $\bar{k} + 3\sigma$; intense events were identified where $\bar{k} + 3\sigma$ was exceeded. Moderate and intense events in the suspended load time series were identified analogously.

The fraction of time where k was above the threshold (ϕ_k) was calculated as the number of data points where the threshold was exceeded divided by the total length of the time series. The importance of the events for the total turbulent kinetic energy (φ_k) was calculated as the sum of values above the threshold divided by the total sum (Yoon and Cox, 2012). The same approach was used to quantify the fraction and importance of events in the suspended load time series, with ϕ_C and φ_C.

To study which fraction of the measured suspension events was related to a turbulence event and vice versa, the fraction of related events was calculated. For this analysis, events were selected that exceeded the turbulence threshold $\bar{k} + \sigma$ or $\bar{C} + \sigma$ for the suspended load series. Turbulence or suspension events were identified as related when they occurred simultaneously within the time window $\pm T_p/2$, where T_p is the peak wave period, of a suspension or turbulence peak, respectively. Events that are advected by the wave-orbital motion can also be related by using this time window (Yoon and Cox, 2012). The fraction of turbulence events related to suspension events ($E_{kC|k}$) was calculated as nE_{kC}/nE_k, where nE_k is the number of turbulence events and nE_{kC} is the number of related events. Similarly, the fraction of suspension events related to turbulence events is $E_{kC|C} = nE_{kC}/nE_C$.

Phase coupling

While event analysis was applied for TR only, the phase coupling analysis also included measurements collected at R1, R2, and R3. This analysis was applied for conditions C1 and C2, as the simulated tidal cycle resulted in a wide range in H_s/h at the location of the rigs, see Section 3.2.4. The cross-shore velocity collected at TR by the lowest ADV was downsampled to 4 Hz to obtain a frequency equal to the concentration measurements. This downsampled signal and the cross-shore velocity measured at R1, R2 and R3 were detrended and subsequently bandpass filtered (0.05–1 Hz) to obtain the high-frequency part (u_hf).

To estimate phase-averaged values of k, c, and u_hf, individual waves were first identified in u_hf using a zero up-crossing method. Subsequently, the time axis of each wave was normalised with its period (t/T). Time series of k, c, and u_hf were then bin averaged over t/T,
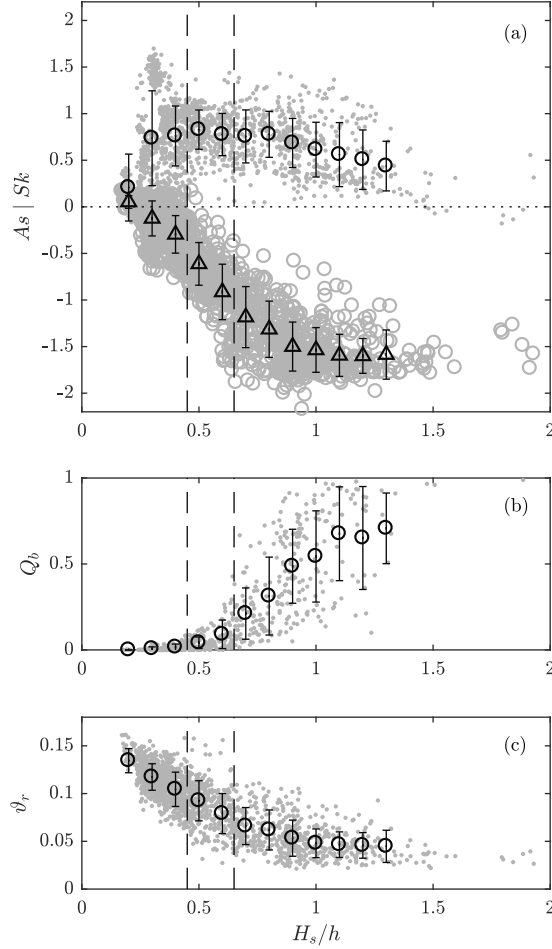
Figure 3.2: Wave shape (a) skewness *Sk* (dots) and asymmetry *As* (circles), (b) fraction of broken waves Q_b, and (c) ripple steepness ϑ_r versus relative wave height H_s/h at all instrument locations. The error bars show the mean and standard deviations.

only including the one third highest waves, with a bin width of 0.05. Including all waves in the binning did not notably change the phase-averaged patterns presented in Section 3.3.2.

The short-wave sand transport rate at individual STMs was estimated as $q_{\text{hf}} = \langle u_{\text{hf}} \cdot c_{hf} \rangle$, where $\langle .. \rangle$ denotes the time average. The vertically integrated sand transport rate was calculated as $Q_{\text{hf}} = \langle u_{\text{hf}} \cdot C_{hf} \rangle$, where C_{hf} is the high-frequency part of the sand concentration integrated over the lowest 3 STMs, similar to Equation 3.4.

3.2.4 Measurement conditions

Due to the variability in water level, wave height, and wave period, measurements were collected under a wide range of hydrodynamic conditions, from symmetric nonbreaking waves to velocity-skewed and velocity-asymmetric breaking waves. The relative wave height (H_s/h) has often been used to scale hydrodynamic conditions (e.g., Osborne and Greenwood, 1992b;

Ruessink et al., 1998; Aagaard et al., 2013), as it gives a good approximation of the location relative to the breaker zone and thus of the nonlinearity of the short waves. This approximation also holds for the BARDEXII data set, as illustrated by the variability of S_k and A_s with H_s/h at the 13 pressure sensors (Figure 3.2) and shown in Chapter 2. *Sk* and *As* increased with H_s/h and Q_b remained close to zero (Figure 3.2b) for $H_s/h < 0.45$ (Figure 3.2a), which implies that these measurements were collected in the shoaling zone. The ripple steepness for these conditions was between 0.1 and 0.15 (Figure 3.2c), i.e., vortex ripples. As H_s/h increased from 0.45 to 0.65, the asymmetry further increased but the skewness remained constant. This H_s/h range is the transition from the shoaling to the surf zone. When $H_s/h > 0.65$, instruments were located in the surf zone, with $|As| > Sk$ and an increasing Q_b. Under these conditions the ripples became flat and elongated, reflected in a decreasing ϑ_r (Figure 3.2c). Ruessink et al. (2015) analyzed 3-D sonar scans collected during the same experiment and showed also an increase in the 3-D ripple irregularity when H_s/h increased. The increase of Q_b with H_s/h was also apparent from the turbulence magnitude, as the time-averaged turbulent kinetic energy increased with H_s/h for this data set, especially when $H_s/h > 0.65$ (Chapter 2; de Winter et al., 2013). Besides the magnitude also the vertical turbulence profile changed, from an increase toward the bottom under nonbreaking waves, to an increase both toward the bottom and to the surface beneath breaking waves. This indicates that the relative importance of surface-generated turbulence increased with H_s/h. As all these hydrodynamic parameters scale well with H_s/h and the value of H_s/h is relatively easy to estimate, this ratio was used to compare hydrodynamic conditions in this study.
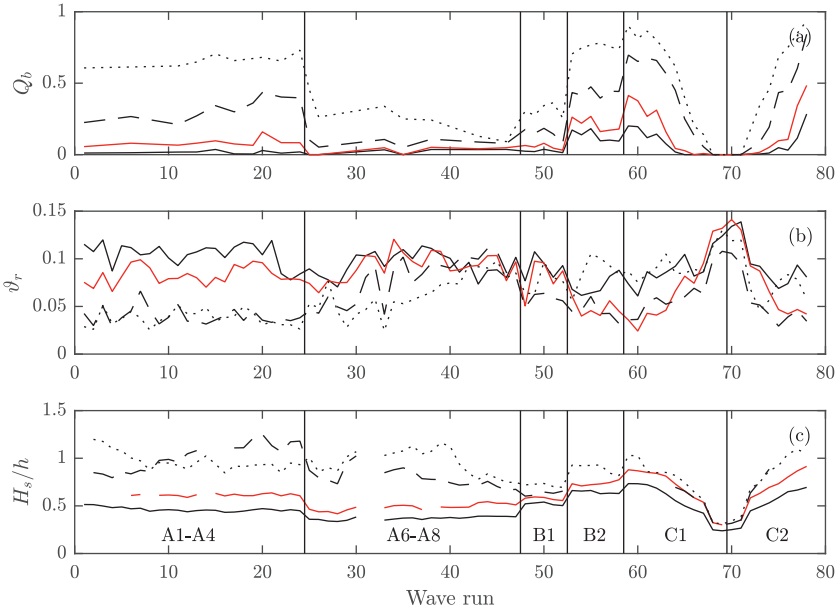

Figure 3.3: (a) Fraction of broken waves Q_b, (b) ripple steepness ϑ_r and (c) relative wave height H_s/h at the location of the four rigs: R1 (black solid line), TR (red solid line), R2 (dashed line) and R3 (dotted line). The solid vertical lines show the separation between the test cases.

An overview of measured conditions during tests A1–C2 at the location of the four rigs is presented in Figure 3.3. Values for H_s/h and Q_b increased over the crest of the bar (located just seaward of R3, Figure 3.1) during the erosive conditions A1-A4 (Figures 3.3a and 3.3c). In accordance to the previous analysis, the ripples became subdued when breaking increased. During subsequent conditions (A6-A8) sand was transported toward the beach face and the water depth increased at all rigs (Figure 3.1), which resulted in a continuously decreasing Q_b and H_s/h at the most landward rig R3 (Figures 3.3a and 3.3c). The wave conditions during B1 were equal to the conditions during A1-A4, but the low flat terrace caused by tests A6-A8 resulted in a lower Q_b at R2 and R3. The decrease in water level during B2 raised H_s/h and Q_b at all locations. During B2, ϑ_r was on average higher in the inner-surf zone ($\vartheta_r \sim 0.1$, $Q_b \sim 0.75$) than in the outer-surf zone ($\vartheta_r \sim 0.05$, $Q_b \sim 0.45$), as observed earlier by Ruessink et al. (2015).

The simulated tidal cycle during tests C1 and C2 caused H_s/h to vary between 0.3 and 1.0 (Figure 3.3c) and thus to cover a wide range in hydrodynamic conditions. For this reason the C series were selected to analyse phase coupling between c and u_{hf}. During the runs with $\zeta = 2.25$ m, Q_b increased from 0.2 to 0.9 over the distance where the rigs were located. During the runs with a high water level, however, most waves broke shoreward of our instrument transect (Figure 3.3a). Observed ripples ranged from steep vortex ripples ($\vartheta_r \approx 0.15$) beneath nonbreaking waves to hummock-type features ($\vartheta_r \approx 0.02 - 0.03$) below breaking waves (Figure 3.3b), see Ruessink et al. (2015) for further details.

3.3 Results

3.3.1 Event statistics

Figure 3.4 shows the thresholds that were used to identify events and the importance of events for the total turbulence and suspension. The two thresholds for k, $\overline{k} + \sigma$ and $\overline{k} + 3\sigma$, show an exponential increase with H_s/h (Figure 3.4a). Thresholds for C are, in contrast, relatively constant (Figure 3.4b). The concentration series were above the threshold $\overline{C} + \sigma$ for about 10% of the time and above $\overline{C} + 3\sigma$ for about 2% of the time irrespective of H_s/h (Figure 3.4d), while the importance of these events in the cumulative load (φ_C) was around 40% and 20%, respectively (Figure 3.4f), similar to values found in earlier studies (Yoon and Cox, 2012; Cox and Kobayashi, 2000). The statistics for the occurrence and importance of turbulence events are comparable with the suspension event statistics (Figures 3.4c and 3.4e). However, when looking in more detail, the fraction of time when k is above the threshold (ϕ_k), decreases with H_s/h for the moderate events and approaches the values of the intense events at $H_s/h \approx 0.8$. This is the result of an increase in kurtosis in k with H_s/h: fewer threshold exceeding events are present but the events are more energetic, and thus events that exceed $\overline{k} + \sigma$ are more likely to also exceed $\overline{k} + 3\sigma$. While the fraction of time in which events are present decreases, the contribution of the events to the total amount of turbulence (φ_k) slightly increases with H_s/h, from < 10% at $H_s/h = 0.4$ to around 20% at $H_s/h = 0.8$ (Figure 3.4e).

The decrease in the fraction of time where k exceeds $\overline{k} + \sigma$ is also reflected in the number of detected turbulence events (Figure 3.5c). While the number of events is decreasing with H_s/h, the fraction of turbulence events which is associated with a suspension event ($E_{kC|k}$) within $-T_p/2$ and $+T_p/2$ is slightly increasing (Figure 3.5a) from 0.4 to 0.6. This implies that turbulence events beneath breaking waves have a higher chance to generate a suspension event than the less energetic turbulence events beneath nonbreaking waves. The number of suspension events is relatively constant (Figure 3.5d), showing the similarity again between
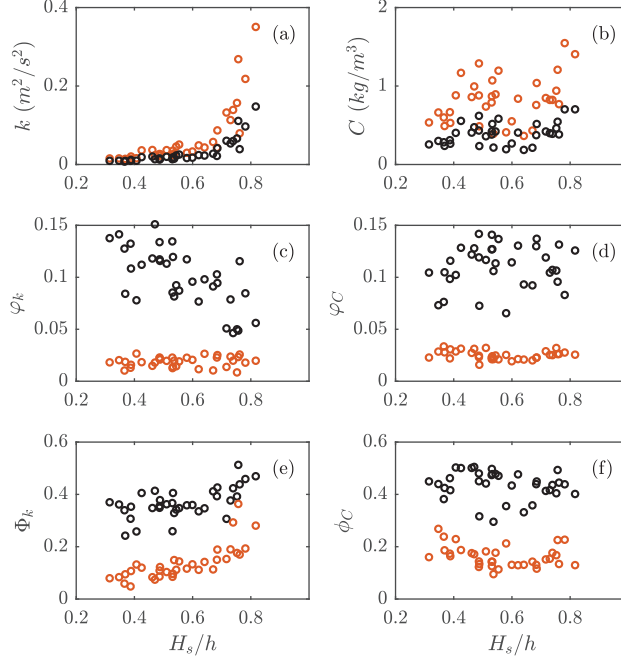
Figure 3.4: Event (a, b) thresholds, (c, d) fraction of time, and (e, f) fraction of total movement for (a,c,e) turbulence and (b,d,f) suspension versus relative waveheight. The black circles represent moderate events (mean + σ), and the red circles represent intense events (mean + 3σ).

measured suspension signals beneath nonbreaking and breaking waves. The fraction of suspension events that are related to a turbulence event ($E_{kC|C}$) shows a slight decrease with increasing H_s/h (Figure 3.5b).

3.3.2 Phase coupling

In the previous section it appeared that measured concentrations cannot be entirely explained by measured turbulence with an event-based approach; therefore, subsequent analysis focused on the coupling of turbulence and suspension in the wave phase. Measured sand concentrations during C1 and C2 at two heights ($z \approx 0.04$ m and $z \approx 0.13$ m) above the bed and at the four rig locations were wave phase-averaged per wave run (25 min). Subsequently, these phase-averaged concentrations were normalised per wave run by dividing them by their maximum value and sorted by relative wave height in Figure 3.6. Beneath nonbreaking waves ($H_s/h < 0.45$) phase-averaged c peaks around $t/T = 0.3$ at $z \approx 0.04$ m, and a phase-lag is observed at the higher sensor with a peak around $t/T = 0.5$. The increase in phase-lag between u_{hf} and c in the vertical, from approximately 0.1 to 0.3 between 0.04 and 0.14 m above the bed, can be seen in more detail when studying a nonbreaking case at the location of TR, where five vertically spaced sensors are located within this range (Figure 3.7e). Phase-averaged k peaks around the same t/T as phase-averaged c at the same elevation (Figure 3.7c), which suggests sand is suspended within turbulent vortices from the bed. Although observations show vortex-type ripples under these conditions (section 3.2.4), phase-averaged concentration does not show signs of ejected vortices during the negative to positive flow reversal. Whether vortex shedding is of significance for sand entrainment

43
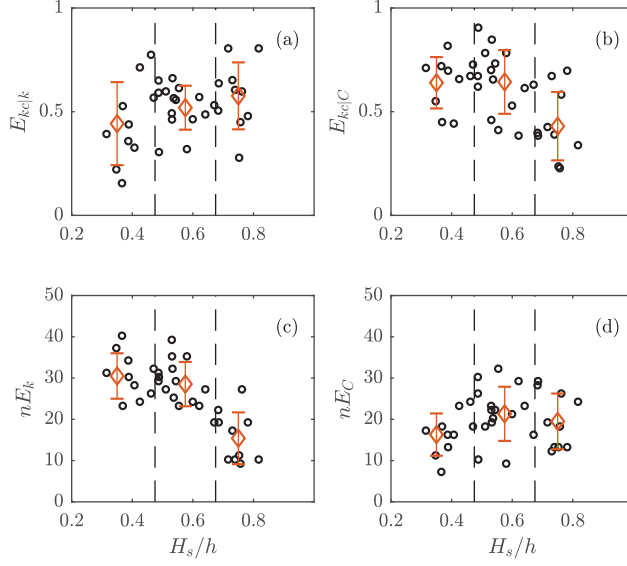
Figure 3.5: (a, b) Event correlation and (c, d) number of events versus relative wave height (H_s/h). The dashed lines represent the nonbreaking regime ($H_s/h < 0.45$) and breaking regime ($H_s/h > 0.65$). The red diamonds show the mean values and standard deviation per regime.

beneath the shoaling waves in this experiment is not clear from the pattern in phase coupling, as the phase-averaged concentration only peaks during positive flow. This has been observed in the field both above ripples (Austin and Masselink, 2008) and above a flat bed (Black and Vincent, 2001). Interestingly, the intrawave variability in k that was found beneath near-sinusoidal waves in Chapter 2, in contrast to the shoaling waves here, does show the ejection of turbulent vortices at the moment of flow reversal.
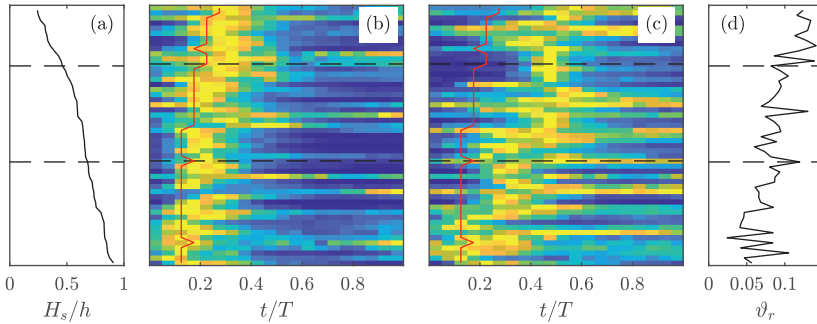
Figure 3.6: Normalized phase-averaged sand concentration from (blue) 0 to (yellow) 1, sorted by relative wave height H_s/h and measured at (b) $z \approx 0.04$ m and (c) $z \approx 0.11$ m. The relative wave height increases from (a) top to bottom. The red solid lines in Figures 3.6b and 3.6c indicate the timing of the maximum positive cross-shore velocity. (d) The ripple steepness ϑ_r.

For increasing H_s/h, the peak in phase-averaged suspension close to the bed ($z = 0.04$ m) shifts from $t/T \approx 0.3$ to $t/T \approx 0.15$ (Figure 3.6b), i.e., the suspension maximum gradually shifts from occurring just after the maximum positive u_{hf} to slightly before maximum positive u_{hf} when the wave-orbital motion becomes more asymmetric. Phase-averaged c at $z \approx 0.11$ m shows considerably more scatter, which might be caused by differences in ripple characteristics (Figure 3.6d), indicating H_s/h does not explain all variability (Figure 3.6c). The general trend, however, is a decrease in phase-lag between u_{hf} and c when H_s/h increases, from 0.3 when $H_s/h = 0.2$ to 0 when $H_s/h = 1$. This implies that the difference in phase coupling of c with u_{hf} in the vertical disappears when H_s/h increases. An example at TR from the wave run with the lowest water level shows the maximum of the phase-averaged c is present at the same t/T throughout the measured vertical transect ($z \approx 0.04 - 0.17$ m, Figure 3.7f). The phase-averaged k for these measurements from the surf zone is an order of magnitude larger than beneath nonbreaking waves and shows the highest value beneath the front of the waves (Figure 3.7d). This probably represents the injection of turbulence by the plunging breakers.

Besides the differences in terms of phase coupling beneath nonbreaking and breaking waves, the nonnormalised phase-averaged concentration beneath nonbreaking waves also shows a decrease in concentration vertically upward and a more homogeneous concentration beneath breaking waves (Figures 3.7c and 3.7d). The concentration close to the bed, $z \approx 0.04$ m, beneath nonbreaking waves is of the same magnitude as beneath breaking waves
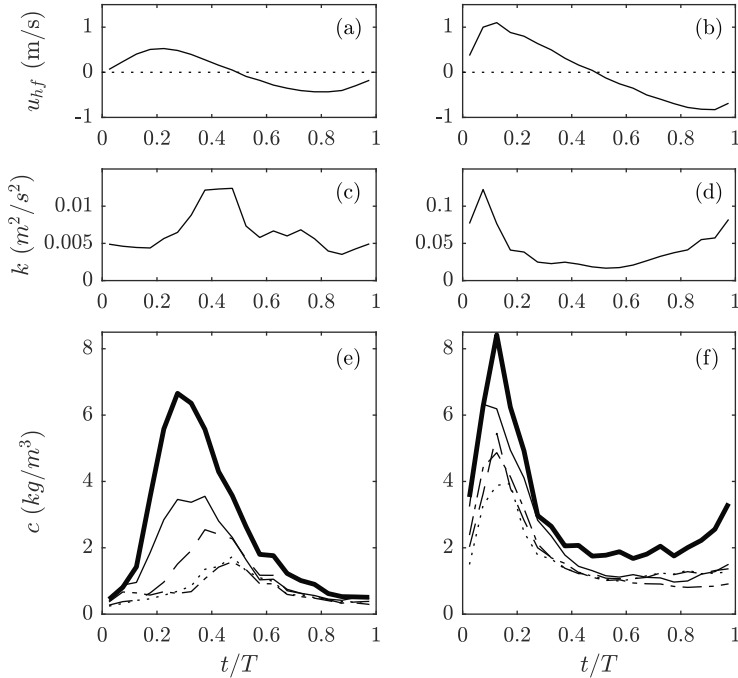
Figure 3.7: Wave phase-averaged values of (a, b) u_{hf}, (c, d) k, and (e, f) c, for a run (a, c, e) without breaking waves and a run (b, d, f) with fraction of breaking waves $Q_b \approx 0.4$. In Figures 3.7e and 3.7f the concentrations at $z \approx 0.04, 0.07, 0.10, 0.14$, and 0.17 m are represented as thick, solid, dashed, dash-dotted and dotted lines, respectively. In Figures 3.7c and 3.7d the turbulence at $z \approx 0.17$ m is shown.
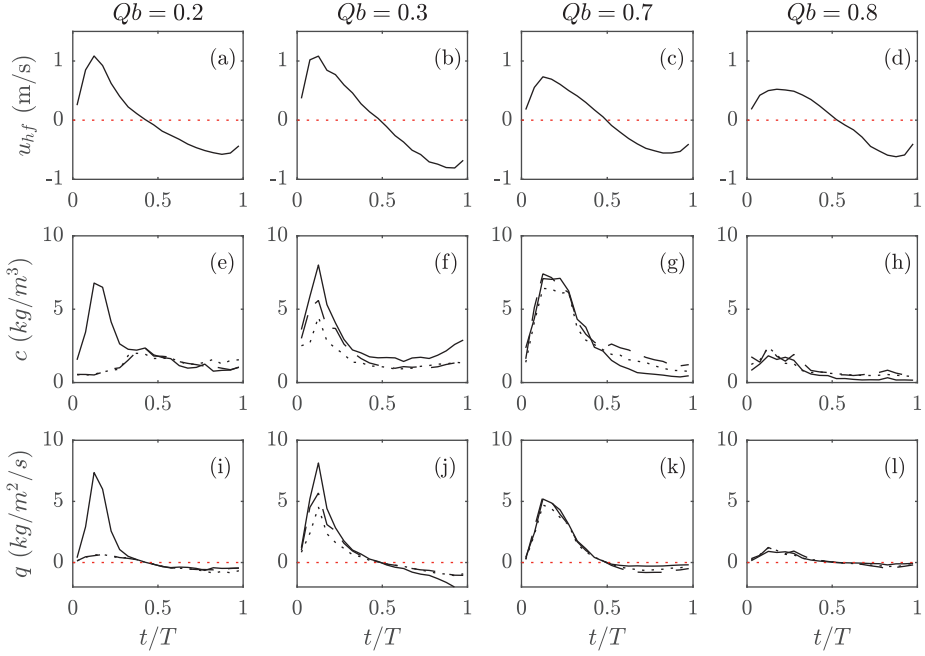
Figure 3.8: Phase-averaged (a–d) u_{hf}, (e–h) c, and (i–l) q at (solid line) $z = 0.04$, (dashed line) $z = 0.07$ and (dotted line) $z = 0.10$ m, at the four rigs in the surf zone during test C1, run 2 or 3.

(Figures 3.7e and 3.7f and 3.8e and 3.8f). To explore the nonnormalised phase-averaged concentration for the outer surf and inner surf, Figure 3.8 shows the cross-shore evolution of phase-averaged u_{hf}, c, and q during two runs of C1 with a low water level and $Q_b = 0.2$–0.8. For each location, run 2 or 3 was chosen depending on which run passed the checks on air bubbles (Section 3.2.2). At R1, where $Q_b = 0.2$, measured c shows a phase-lag in the vertical, with maximum phase-averaged c at the higher sensors during positive to negative flow reversal, as was earlier also seen for lower Q_b values. During those conditions, q_{hf} is only of importance close to the bed (Figure 3.8i). As Q_b increases to 0.3, the phase-lag between the concentration time series in the vertical approaches zero. Further shoreward ($Q_b = 0.7$), the concentration peak widens but remains high throughout the positive flow phase of the waves (Figure 3.8g). With increasing distance from the onset of wave breaking, well into the inner-surf zone with $Q_b \sim 0.8$, the amount of sand suspended in the water column decreases at all heights but the phase coupling and thus the sand transport direction remain unaltered (Figures 3.8h and 3.8l).

The net effect of different phase coupling within the wave phase and in the vertical leads to a dependence of the cumulative high-frequency transport Q_{hf} on H_s/h. As discussed previously, the phase-lag increases and sand concentration decreases vertically upward for low H_s/h. Hence, Q_{hf} is around zero for $H_s/h < 0.65$ (Figure 3.9). Below plunging waves, sand is suspended during the onshore wave-orbital motion throughout the vertical measurement transect. Hence, Q_{hf} is positive and substantially larger in the outer-surf zone ($0.6 < H_s/h < 1.0$). Further shoreward, beneath bores in the inner-surf zone ($Q_b > 0.5$), the transport decreases as sand concentrations decrease (Figure 3.9). This implies that the largest onshore Q_{hf} are found in the outer-surf zone.

3.4 Discussion

The fraction of related events in the surf zone is relatively high (both $E_{kC|k}$ and $E_{kC|C}$) compared to the data of Yoon and Cox (2012). This indicates that turbulence beneath plunging breakers is more effective in stirring sand from the bed than the turbulence beneath spilling breakers in their experiments. Although the related event fractions are high, in none of the tests all suspension events are related to turbulence. This can, at least partly, be explained by the instruments measuring in one location. It is very well possible that suspension events were generated by measured turbulence events but were missed by the STMs or vice versa. Visual observations in detailed small-scale laboratory experiments showed that sand suspension is strongly three-dimensional (e.g., Nadaoka et al., 1988). Irrespective of the causes, it is obvious that individual sand suspension events cannot be predicted deterministically from turbulence information alone, see also Yoon et al. (2013). Therefore, the results of a more stochastic approach, i.e., averaging in the wave phase, were subsequently evaluated.

We acknowledge that the wave-induced sand transport is not represented by the suspended load transport alone, bed load transport can under specific conditions also significantly contribute. Miles and Thorpe (2015) discussed the relative importance of bed load transport using field measurements of bed form migration rates, which are shown to give a good representation of the bed load transport under conditions when sheet flow is not of importance (Traykovski et al., 1999). The bedform contribution to the total transport in their measurements varied highly between individual cases but was around 15% if averaged over the cross-shore. Migration rates are driven by nonlinearities in the wave-orbital motion (Masselink et al., 2007; Miles and Thorpe, 2015) and are therefore part of the total wave-induced transport. Bed forms were not observed to migrate in a specific direction during the cases discussed in this study (Ruessink et al., 2015), and the suspended load transport thus probably explains the bulk of the total wave-induced sand transport.

Earlier measurements beneath velocity-asymmetric flows in oscillatory flow tunnels (van der A et al., 2009; Ruessink et al., 2011) show high sand concentration during both the positive and negative flow phase. Beneath the plunging breakers and bores in our study, sand is predominantly suspended during the onshore wave-orbital motion. For the plunging breakers this can be ascribed to the injection of turbulence at the wavefront, this strong phase coupling of turbulence with the wave-orbital motion was also seen in other laboratory studies (e.g., Ting and Kirby, 1994; van der Zanden et al., 2016). There is, however, less agreement on
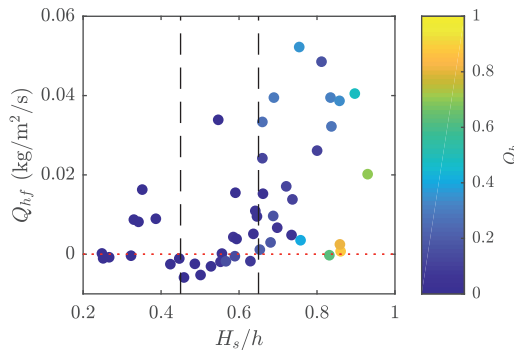

Figure 3.9: The cumulative high-frequency transport Q_{hf} vs relative wave height H_s/h. The colors indicate the fraction of broken waves Q_b.

the existence of phase coupling in the inner-surf zone. Several studies, both in the laboratory and in the field, suggest that sand suspension becomes unrelated to the wave-orbital motion beneath surf bores (e.g., Nadaoka et al., 1988; Barkaszi and Dally, 1992; Aagaard and Hughes, 2010), while in our measurements and the field measurements by Yu et al. (1993) sand suspension occurred predominantly beneath the crest of the bores. This difference might be explained by the breaker type from which the bores originate, as Ting and Kirby (1995) and Ting and Kirby (1996) describe that turbulence is more homogeneous beneath bores that originate from spilling breakers. Ting and Kirby (1994) ascribe this difference to the higher H_s/h present beneath bores that originate from plunging breakers. This means that for the same h, plunging breaker bores are higher and can thus be more effective in stirring sand. This hypothesis is in agreement with the breaker types during the experiments of Nadaoka et al. (1988) (spilling breakers) and Yu et al. (1993) (plunging breakers), but it is difficult to compare all measurements as information on the exact location of the instruments with respect to the breakpoint is often not provided.

In this study we have shown the differences between sand suspension under nonbreaking and breaking irregular waves, with fraction of breaking waves between $Q_b = 0$ and $Q_b = 0.8$. Overall, when H_s/h and Q_b increase, turbulence becomes more effective in stirring sand from the bed and simultaneously reduces the phase-lag in the vertical between the wave-orbital motion and concentration. The wave-induced sand transport in current morphodynamic models is often solely based on the wave-orbital motion and thus lack the effect of surface-generated turbulence. Most of these models now need site-specific calibration through free model parameters (e.g., Ruessink et al., 2007; Walstra et al., 2012; Dubarbier et al., 2015) to compensate for the lack of certain physical processes. In this study we show that sand suspension is strongly coupled to the onshore phase of the wave-orbital motion beneath plunging breakers and bores. This signifies that the onshore-driven sand transport in the surf zone is significantly higher than in the shoaling zone and that this difference is, at least partly, explained by the presence of surface-generated turbulence.

3.5 Conclusions

Measurements of near-bed turbulence, wave-orbital motion, sand concentration and ripple characteristics were collected beneath irregular waves in the shoaling and surf zone of a field-scale laboratory beach. Event-by-event analysis shows that turbulence beneath plunging breaking waves with subdued ripples is more effective in stirring sand from the bed than turbulence beneath nonbreaking shoaling waves above vortex ripples. Although turbulence events can be correlated to about 50% of the suspension events, the origin of a large part of the suspension events remains unclear.

Below nonbreaking waves, sand is brought into suspension right after the maximum positive wave-orbital motion u_{hf} and reaches higher elevations during flow reversal from positive to negative u_{hf}. This is substantially different from the suspension pattern beneath breaking waves and bores, where phase-averaged c peaks during the positive-directed wave-orbital motion throughout the measured part of the water column. In the inner-surf zone c remains phase coupled to the wave-orbital motion, but the concentration decreases with distance from the onset of wave breaking.

The vertically integrated suspended sand transport by short waves Q_{hf} is thus onshore and largest beneath plunging waves. Under bores, Q_{hf} remains onshore but is smaller, while under shoaling waves Q_{hf} is smallest and can also be offshore directed. To accurately predict the contribution of short, breaking (plunging) waves to the total suspended sand transport

in morphodynamic models, the effect of the injection of surface-generated turbulence on short-wave sand transport should thus be included.

Acknowledgments

Chapter 4

Sand transport in the shallow surf zone

Abstract

Measurements of near-bed velocity and suspended sand concentration, collected during two field campaigns (at the Sand Engine and Ameland, the Netherlands) and one field-scale laboratory experiment (BARDEXII), were analysed to study the magnitude, direction and relative importance of the short-wave sand flux in the shallow surf zone. The measurements were conducted on a wide range of beach profiles, with a steepness from 1:15 to 1:80. Conditions range from from low-energetic accretive conditions, with short waves dominating the total sand flux, to high-energetic erosive conditions, with the mean cross-shore current (undertow) dominating the total sand flux. Under low-energetic conditions, the onshore-directed short-wave sand flux scales with the root-mean-square orbital velocity u_{rms} and velocity asymmetry A_u, but not with the velocity skewness. Under more energetic conditions the short-wave flux reduces with an increase in the cross-shore mean current $\overline{u}$ and can even become offshore-directed. For all data combined, the contribution of the short-wave flux to the total flux scales with $(-A_u u_{rms})/|\overline{u}|$, with a high contribution of the short-wave flux ($\sim 70\%$) when this ratio is high ($\sim$ 10) and low contributions ($\sim 0\%$) when this ratio is low (~ 1). We argue that the velocity asymmetry is a good proxy for the net effect of several transport mechanisms in the shallow surf zone, including breaking-induced turbulence. These field and laboratory measurements under irregular waves thus support the hypothesis that the inclusion of velocity asymmetry in transport formulations would improve the performance of morphodynamic models in shallow water.

4.1   Introduction

In the surf zone, short waves (wave period of 1–20 s) become asymmetric about the vertical axis, with a steep front face and a gentle rear face (i.e. pitched-forward), and reduce in height due to energy dissipation through breaking. Both wave asymmetry and breaking-induced turbulence can affect the magnitude and direction of the short-wave sand transport (e.g., van der A et al., 2009; Scott et al., 2009) and therefore prohibit the application of transport formulas designed for deeper water and shoaling wave conditions. The short-wave driven sand transport is particularly important during low-energetic conditions, when other transport components, i.e. long-wave (wave period of 20–200 s) driven transport and transport by mean cross-shore currents, are small (e.g., Osborne and Greenwood, 1992b; Aagaard et al., 2013). During these low-energetic conditions, the short-wave sand transport is often crucial for the onshore migration of nearshore bars (e.g., Aagaard et al., 2002; Hoefel and Elgar, 2003), and thus for the recovery of beaches between storms.

The wave orbital velocities in shallow water change analogously with the wave shape and also become skewed in the shoaling zone and asymmetric in the surf zone. While velocity skewed flows were shown to transport sand in the onshore direction (e.g., Ribberink and Al-Salem, 1994; O'Donoghue and Wright, 2004) under flat bed conditions, asymmetric flow was long believed to not induce sand transport (Roelvink and Stive, 1989). However, flow tunnel experiments later showed asymmetric flow to drive sand transport in the direction of highest acceleration (King, 1991; Watanabe and Sato, 2004; van der A et al., 2009; Ruessink et al., 2011; Silva et al., 2011), which would also be in the onshore direction on a natural beach. This onshore transport has been ascribed to several mechanisms. Firstly, the boundary layer has less time to grow during the large acceleration between maximum negative and maximum positive velocities in comparison with the long duration and small acceleration from maximum positive to negative flow. The vertical gradient in flow velocity is thus larger and shear stresses are higher during the positive flow phase (Nielsen, 1992; Henderson et al., 2004; van der A et al., 2008). Secondly, sand stirred during maximum negative flow has less time to settle before flow reverses in comparison with sand stirred during the maximum positive flow. This effect is largely dependent on the sediment fall velocity, and a modeling study by Ruessink et al. (2009) indicated that these phase-lag effects are only important for fine-medium sands ($\lesssim$ 250 μm). Another process that can contribute to the onshore directed transport is plug flow (Sleath, 1999; Foster et al., 2006; Calantoni and Puleo, 2006), a term to describe an instant mobilization of several centimeters of sand by the horizontal pressure gradient during the strong flow acceleration at the front of the waves. This mobilized sand is then available for transport during the onshore flow phase. The relative contribution of these mechanisms to the onshore transport by velocity asymmetric waves and the variability of these contributions as a function of wave conditions and beach characteristics are, however, unknown.

Strong opposing currents were also found to affect the transport of sand by oscillatory flow, as these currents increase shear stress during the negative directed flow phase and decrease the shear stress during the positive directed phase. This effect can reverse the net transport direction, depending on the magnitude of the current and the degree of asymmetry of the oscillatory flow (Ruessink et al., 2011; Silva et al., 2011). In the field, a strong undertow was suggested to enhance shear stress during the offshore directed flow phase of long waves (de Bakker et al., 2016), and Aagaard et al. (2013) suggested that strong undertow velocities can have a similar effect on the shear stress beneath short waves, although field observations to support this hypothesis are hitherto lacking.

Most of the above mentioned studies were conducted in flow tunnels, where the effects of nonlinear oscillatory flow on sand suspension are studied in isolation. In nature, however, these asymmetric oscillatory flows only exist in combination with breaking-induced turbulence injected from the water surface. This breaking-induced turbulence can descend toward the bed and enhance pick-up and vertical mixing of sediment (e.g., Nadaoka et al., 1988; Sato et al., 1990; Beach and Sternberg, 1996; Voulgaris and Collins, 2000; van der Zanden et al., 2017). The effect of surface-induced turbulence on short-wave sand transport depends on whether the turbulent vortices reach the bed during the positive or the negative flow phase. This phase-coupling between the surface-induced turbulence and the wave orbital motion was found to be positive under plunging breakers (e.g., Ting and Kirby, 1995; Aagaard and Hughes, 2010; Brinkkemper et al., 2017b). However under spilling breakers and bores contradictory observations were described, with the phase-coupling being either positive (e.g., Ting and Kirby, 1994), negative (e.g., Ting and Kirby, 1996; Yoon and Cox, 2012) or absent (e.g., Aagaard and Hughes, 2010; van der Zanden et al., 2016).

Practical engineering models rely on empirical parameterizations of the sand transport, irrespective of the precise mechanisms responsible. In this study, we combine sand flux measurements at three distinct beach profiles and hypothesize that, in order to improve sand transport predictions in the surf zone, the velocity asymmetry could be used as a proxy to include the combined effect of the relevant transport mechanisms in the parameterisations. Firstly, we introduce the three different datasets and discuss the data processing and analysis in Section 4.2. In Section 4.3 general trends in the measured short-wave sand flux are discussed and are combined to explain its relative importance to the total flux. In Section 4.4 we discuss the significance of our findings and suggest further steps to improve sand transport predictions in the shallow surf zone. Lastly, the main conclusions are summarized in Section 4.5.

4.2 Methods

4.2.1 Data collection

Observations used for this study were collected during two field and one large-scale wave flume experiment. The first field campaign took place on the gently sloping (1:80, Figure 4.1) Ballum beach at the Dutch barrier island Ameland in the autumn of 2010 (AM, de Bakker et al. (2014)). The second field campaign was conducted at the moderately sloping (1:35)
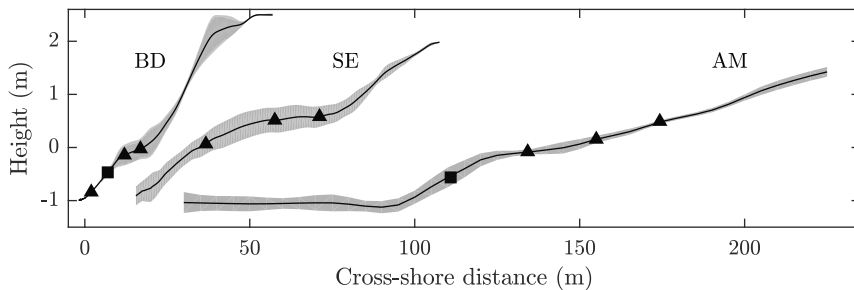

Figure 4.1: Mean cross-shore beach profiles with (grey) standard deviation during the experiments BARDEXII (BD), Sand Engine 2014 (SE) and Ameland 2010 (AM). The squares and triangles indicate the location of the rigs, of which the squares indicate the location of the rig with ADVs.

Sand Engine beach, a mega-nourishment (de Schipper et al., 2016) near the town Ter Heijde, also in the Netherlands, in the autumn of 2014 (SE, de Bakker et al. (2016)). The flume measurements were collected on a steep beach profile (initially 1:15) during BARDEXII (Barrier Dynamics Experiment II) in the Delta Flume in the summer of 2012 (BD, Masselink et al. (2016)). The median sand grainsize d_{50} was 200, 350 and 420 μm for AM, SE and BD, respectively.

During the three experiments, measurements of near-bed flow velocities, near-bed pressure and sand concentrations were collected with instruments attached to four rigs deployed in a cross-shore array (Figure 4.1). Three of those rigs were equipped with an electromagnetic flowmeter (EMF), three optical backscatter sensors (Seapoint Turbidity Meters or STMs) and a pressure transducer (PT). The nominal height of the instruments above the bed was 0.15-0.20 m for the EMF, 0.03-0.20 m for the STMs and 0.05-0.10 m for the PT. The fourth rig comprised three vertically spaced Acoustic Doppler Velocimeters (ADVs), seven STMs and a PT. The nominal heights of these instruments were 0.15–0.70 m for the three ADVs, 0.04–0.70 m for the STMs and 0.05–0.10 m for the PT. The sampling frequency of all instruments was 4 Hz, except for the ADVs which sampled at 10 Hz. The data from the fourth rig at SE were discarded as large bed level changes affected the rig stability.

The cross-shore instrument array was located in the intertidal zone during the AM and SE field campaigns. This implies that the instruments were submerged and measuring during high tide, while data retrieval and adjustment of the sensor height were possible during low tide. Also during low tide, cross-shore bed profiles were measured with RTK-GPS every other day at AM and every day at SE. At SE, offshore wave conditions were obtained from a directional wave buoy located in 11 m water depth, 0.8 km seaward of the measurement array. For AM, these data were available from a directional wave buoy in 24 m water depth.

The BD experiments consisted of five test series (A-E) that were divided into tests with different wave and/or water level conditions. The tests were subsequently divided into wave runs with a duration of 10 to 120 min. In between each of those wave runs the bed level along the centerline of the flume was surveyed (Ruessink et al., 2016) and the heights of the instruments above the bed were adjusted to their desired values.

4.2.2 Data processing and analysis

All data were analysed in blocks of 30 minutes. The 30 minute window was chosen as a sufficiently long period to attain a robust average over the typical wave characteristics, while it is short enough for the tidal water level to be approximately constant. Measured near-bed pressure was converted to sea surface elevation (η) with linear wave theory. The water depth (h) was calculated as the sum of the mean pressure and the instrument height above the bed. The significant high-frequency waveheight (H_s) was calculated as the zeroth moment of the wave energy spectrum from 0.05 to 1 Hz. The Ursell number was used to quantify the degree of nonlinearity (e.g., Doering and Bowen, 1995; Ruessink et al., 2012a) and was calculated as

$$Ur = \frac{3}{4} \frac{a_w k}{(kh)^3}, \tag{4.1}$$

where $a_w = 0.5 H_s$ and k is the wave number computed with linear theory using the peak wave period T_p.

The flow velocity was defined so that u is cross-shore and positive in the landward direction. Subsequently, the cross-shore velocity was bandpass filtered into its low (u_{lf}, 0.005 − 0.05 Hz) and high (u_{hf}, 0.05 − 1 Hz) frequency component, i.e. the long-wave and short-wave

component. The nonlinearity of u_{hf} was expressed with its skewness S_u as

$$S_u = \frac{\langle u_{hf}^3 \rangle}{\langle u_{hf}^2 \rangle^{3/2}},$$

(4.2)

where $\langle ... \rangle$ denote time averaging, and with its asymmetry A_u, by replacing u_{hf} in Eq (4.2) with its Hilbert transform (Elgar, 1987). The velocity asymmetry is linearly correlated with the skewness of the acceleration, but is less sensitive to the high-frequency cut-off that is used to estimate u_{hf} (Elgar, 1987).

The STMs were calibrated in a recirculation tank with sediment samples collected at the location of the instruments at the end of each campaign. The calibration resulted in a quadratic correlation between output voltages and concentration c up to $\sim 30 - 40$ kg/m³ with $r^2 \sim$ 0.99 for all datasets. Field offsets that were present in the calibrated concentrations were determined from the cumulative frequency distribution (e.g., Aagaard and Hughes, 2006) and were around the 5th percentile for all STM data. These offsets were subtracted from the data and negative values were set to zero.

STM measurements are sensitive to air-bubbles (Puleo et al., 2006), and concentration time series collected in the surf zone should thus be checked for the presence of these bubbles. Air-bubbles can be recognised in concentration data as high and narrow spikes, often occurring prior to an actual sand suspension event. To diminish the effect of air-bubbles on our analysis, concentration measurements were selected for the analysis based on two criteria: the sand concentration decreases vertically upward and a cross-correlation with a higher sensor should show a positive correlation at a negative lag (Aagaard and Jensen, 2013), i.e. events occur in general first at the lower sensor. Moreover, concentration time-series that showed signs of the sensor being too close to the bed, or a fluctuating offset due to the presence of fine suspended particles, were rejected. Fluctuating offsets in the STM signals were particularly found in the SE dataset during low energetic conditions, hence the block size in which data was quality controlled and analysed for BD and AM (30 min) was reduced to 10 min for SE. This increased the number of blocks available for data analysis, as offsets were often approximately stable at a timescale of 10 min. A reduction in block length did not result in a wider range in conditions in the quality controlled data for AM or BD, and it was thus decided to not reduce the block length for those datasets.

For each 10 min or 30 min block that passed the concentration quality checks, the lowest STM in the range of 0.03–0.10 m above the bed was selected for further analysis. The concentration time series were frequency filtered into c_{hf}, c_{lf} and its mean component $\bar{c}$. These concentration components were combined with their correlating velocity components at the colocated flow meter to calculate sand fluxes q_{tot}, q_{hf}, q_{lf} and q_m as

$$q_{tot} = q_{hf} + q_{lf} + q_m = \langle u_{hf} \cdot c_{hf} \rangle + \langle u_{lf} \cdot c_{lf} \rangle + \bar{u} \cdot \bar{c},$$

(4.3)

where positive q means a flux in the shoreward direction and the angle brackets and overbar represent a time average. The relative importance of q_{hf} for the total flux was calculated as

$$\widehat{q}_{hf} = \frac{q_{hf}}{|q_{hf}| + |q_{lf}| + |q_m|}.$$

(4.4)

The contributions of q_{lf} and q_m were calculated analogously as $\widehat{q}_{lf}$ and $\widehat{q}_m$.

The height of the selected STM above the bed affects the measured mean concentration and can also affect the phase-coupling between u and c. Phase-lags in the vertical can be
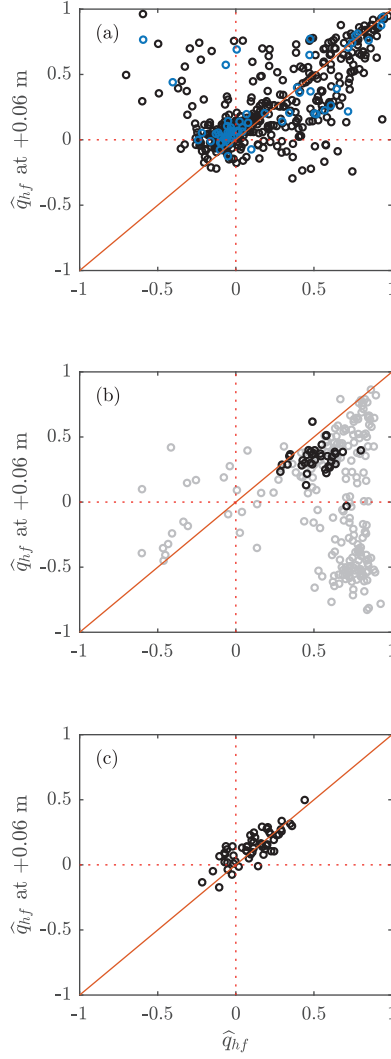
Figure 4.2: The relative importance of q_{hf} for the total sand flux at the selected STM and at a sensor 0.06 m higher for the (a) Sand Engine, (b) BARDEXII and (c) Ameland datasets. The red solid line is the line of equality. The blue and black circles in (a) signify the 30 and 10 minute blocks, respectively. The black circles in (b) are observations that were selected for further analysis based on the ripple steepness. See Section 4.2.2 for further explanation.

neglected for low frequency motions (de Bakker et al., 2016), but are of importance at higher frequencies especially below non-breaking waves above wave-induced ripples, which can reduce measured q_{hf} and even reverse the direction of the estimated flux (e.g., van der Werf et al., 2007). Beneath breaking waves, phase-lags in the vertical are generally small (Brinkkem-

per et al., 2017b). Here, we explore the difference between $\widehat{q}_{hf}$ at the selected sensor and at a sensor 6 cm higher in the water column (Figure 4.2) to avoid a sensitivity of the results to the height of the sensor. The difference between the two sensors can be explained by both a decreasing concentration and a decreasing phase-coupling between u_{hf} and c_{hf} vertically upward, hence $\widehat{q}_{hf}$ at +0.06 m is both above and below the line of perfect agreement with $\widehat{q}_{hf}$ at the selected sensor for SE (Figure 4.2a). Although $\widehat{q}_{hf}$ shows considerable sensitivity to sensor height above the bed for SE, fluxes are generally (88%) in the same direction. This is often not the case for BD (Figure 4.2b), where large phase-lags between the sensors can result in a reversal of the flux direction. Brinkkemper et al. (2017b) showed for the same dataset that these phase-lags particularly occur beneath non-breaking waves with steep ripples. As our analysis focus on breaking wave conditions, measurements are used in the following analysis only when the ripple steepness was below 0.05. This also reduces the sensitivity of our results to the height of the sensor above the bed. The normalised measurements collected in the inner-surf zone at AM are not sensitive to sensor height (Figure 4.2c). This lack of sensitivity indicates the relatively small grain size at AM does not induce a phase-lag between u_{hf} and c.

Quantile regression was used to test whether linear relations between hydrodynamic parameters and sand fluxes are statistically significant. This method is more robust than least-square regression when one or more factors of influence are unmeasured, i.e. when data are scattered, as 'outliers' affect least-square regression (Cade and Noon, 2003). Regression lines were computed for the minimum, median and maximum response by taking the 10%, 50% and 90% quantiles, denoted as $\tau = 0.1$, 0.5 and 0.9, following the approach of de Bakker et al. (2016). The 90% statistical significance of these regression lines was estimated following Koenker (2005).

4.2.3 Measurement conditions

Offshore wave heights H_o during the Sand Engine campaign were between 0.1 and 4.9 m with significant wave periods T_o between 2.7 and 14.2 s (Figures 4.3a and 4.3d). The first four weeks of the campaign are characterised by low offshore wave heights ($H_o < 0.5$ m) alternating with short periods with moderate waveheights of $1.5 - 2.0$ m. A storm during the last week of the campaign resulted in H_o up to 4.9 m and an elevated water level up to 2 m above mean sea level. Wave dissipation during high tide and seaward of the first measurement rig only occurred when the offshore waveheight was larger than 1 m. The tidal range at the Sand Engine was around 2 m (Figure 4.3g). The data from the BARDEXII experiment that focused on surf zone dynamics can be divided into six test series (A1-A4, A6-A8, B1, B2, C1 and C2). The wave height and peak wave period were 0.89 m and 8 s, respectively, for series A1-A4 (Figure 4.3b and 4.3e). Subsequently the wave height was lowered to 0.75 m and the wave period increased to 12 s for A6-A8. The wave conditions during B1 and B2 are equal to A1-A4, but the water level was 0.5 m lower during B2 (Figure 4.3h). The water level was gradually raised from $\eta = 0$ to $\eta = 1.3$ m during C1 and lowered back to $\eta = 0$ m during C2 to simulate a full tidal cycle over a time-span of 12 hours. The wave height was lowered to 0.55 m during the last wave runs of C1 and the first of C2 to avoid wave overtopping the flume walls. H_o during the field campaign at Ameland was generally higher than at SE, but shows a similar range between 0.3 and 5.9 m (Figure 4.3c). T_o ranged between 3.2 and 10.2 s and was higher during periods with large H_o (Figure 4.3f). Wave heights were substantially reduced before reaching the first instrument rig, as wave breaking occurred on an ebb tidal delta a few kilometers offshore. The tidal range of 3 m is approximately 1 m higher than at SE (Figure 4.3i).
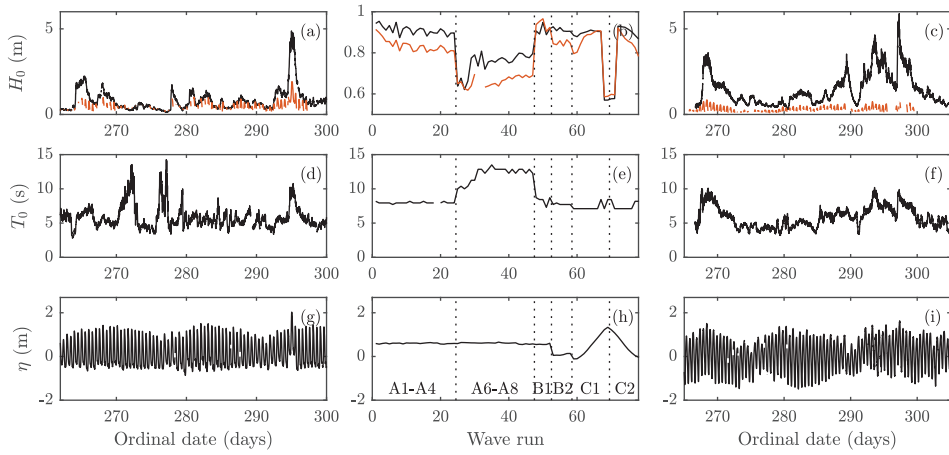
Figure 4.3: Wave characteristics and water levels during the lab- and field experiments. (a-c) Significant wave height H_0 at (black) an offshore wave buoy or the wavemaker and (red) the most seaward located suspension rig, (d-f) offshore significant wave period T_0, and (g-i) the water level η, for the (a,d,g) Sand Engine, (b,e,h) BARDEXII and (c,f,i) Ameland experiments.

The wide range in offshore wave conditions resulted in a range in H_s/h at the different rigs for the selected time series. This range was $H_s/h = 0.18 - 0.81$, $H_s/h = 0.56 - 1.31$ and $H_s/h = 0.35 - 0.64$ for the SE, BD and AM experiments, respectively. Considering the seaward boundary of the surfzone to be $H_s/h \sim 0.33$ for mild to moderately sloping beaches (Ruessink et al., 1998) and $H_s/h \sim 0.65$ for the steep beach slope in BD (Brinkkemper et al., 2016), the large majority of the measurements were collected in the surf zone (Figure 4.4). Due to the placement of the rigs in shallow water (h is typically between 0.5 and 1.5 m, except during the storm surge towards the end of the campaign at SE, when h is up to 3 m) this includes the outer and inner-surf zone during low-energetic conditions and only the inner-surf zone during high-energetic conditions. The term shallow surf zone is here used to refer to the hydrodynamic zone in which these measurements were conducted.

Figure 4.4: Histogram of the number of data blocks that include sand fluxes for the (a) Sand Engine, (b) BARDEXII, and (c) Ameland experiments, separated in 0.1 wide classes of relative wave height H_s/h. The vertical dashed line represents an estimate of H_s/h at the seaward edge of the surf zone.

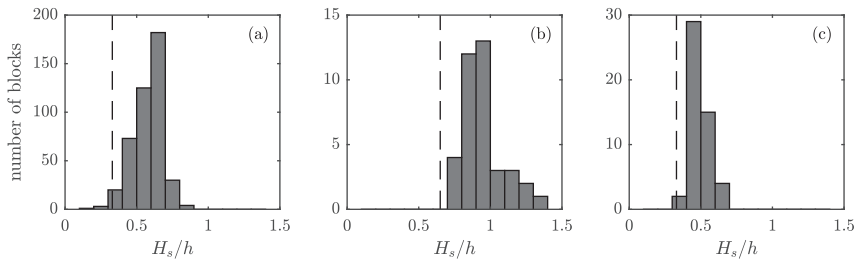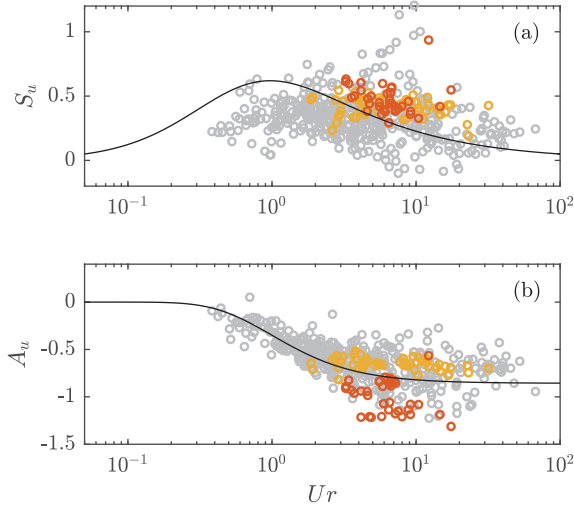**Figure 4.5:** Velocity nonlinearity (a) velocity skewness S_u and (b) velocity asymmetry A_u versus the Ursell number Ur for the (grey) Sand Engine, (red) BARDEXII and (yellow) Ameland experiments for cases where sand fluxes are available. The solid lines show parameterisations based on field data by Ruessink et al. (2012a).

The wide range in offshore wave height and periods at SE, together with a relatively high number of data blocks that passed the quality checks, resulted in observations collected beneath waves which demonstrate a wide range in nonlinearity, from a near-sinusoidal wave-orbital motion with $S_u \sim 0.2$ and $A_u \sim 0$ to a highly skewed/asymmetric wave-orbital motion with $S_u \sim 1$ and $A_u \sim -1$ (Figure 4.5). The velocity skewness in the measured range does not show a clear dependence on Ur. The velocity asymmetry, however, increases with Ur until $Ur \gtrsim 10$, consistent with the parameterisation by Ruessink et al. (2012a) (Figure 4.5a). While values for S_u for BD and AM are similar for equal Ur, A_u at BD is higher in comparison for the same Ur at AM.

4.3 Results

The observations from SE that passed the quality checks contained a wide range in hydrodynamic conditions, from low-energy swell to high-energy wind waves. Two high tides were selected from the SE dataset as an example for accretive and erosive conditions (Figure 4.6), a high tide with low-energetic swell waves ($H_o = 0.35$ m, $T_s = 9$ s) and a high tide with relatively energetic wind waves ($H_o = 1.10$ m, $T_s = 5$ s), respectively. Fluxes at the selected sensor were averaged over a two-hour block around each high tide to enable a comparison with the net morphological changes. The intertidal bar steepened and moved in the landward direction during the accretive high tide (Figure 4.6a). Moreover, a swash berm developed around the high water line. The magnitude of q_{hf} is largest on the seaward flank of the bar, where it dominates the total sand flux, and decreases across the intertidal bar in landward direction. The magnitude of q_{lf} is small but changes direction from offshore to onshore over the intertidal bar. This is caused by a change in correlation between the short-wave envelope,
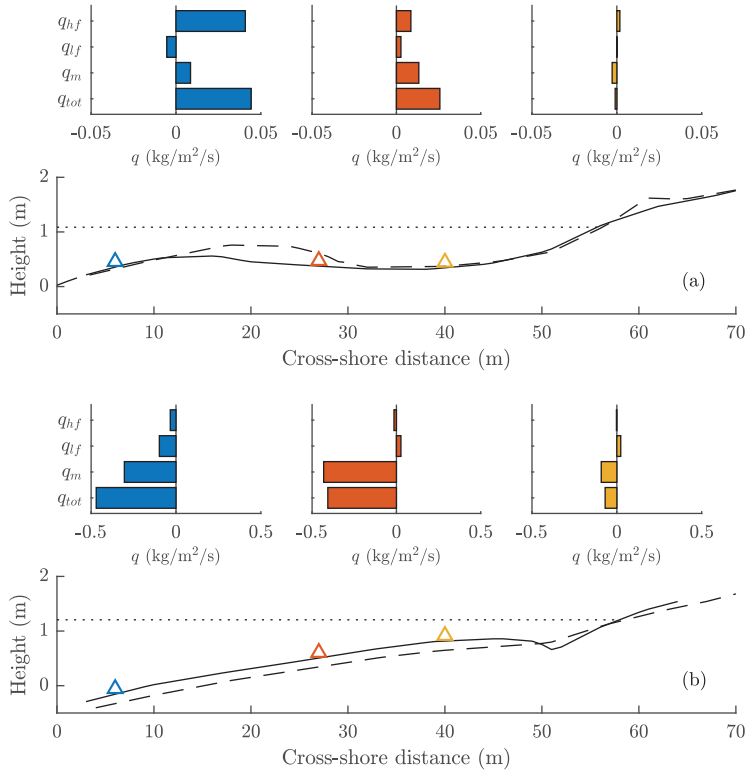
Figure 4.6: Sand fluxes at (triangles) three cross-shore locations for the Sand Engine experiment, averaged over (a) two accretive high tides and (b) two erosive high tides. Shown cases correspond to offshore wave conditions (a) $H_0 = 0.35$ m, $T_s = 9$ s and (b) $H_0 = 1.10$ m, $T_s = 5$ s. The solid (dashed) line shows the beach profile before (after) the high tides, and the dotted line shows the mean high tide water level. The barplot colors correspond with the colors used to indicate the locations of the rigs.

a proxy of sand stirring, and the long-wave orbital motion from negative to positive values, as shown by de Bakker et al. (2016) using the same SE dataset. Mean cross-shore currents transport sand in the onshore direction above the intertidal bar. This indicates the presence of a horizontal cell circulation, with a mean current in the landward direction over the bar and presumably seaward flow in a nearby cross-shore oriented channel. The onshore migration of the sandbar is thus mainly driven by cross-shore gradients in q_{hf} and q_m, with a small contribution of q_{lf} landward of the crest of the bar.

The intertidal beach was flattened and lowered during the erosive high tide (Figure 4.6b). Here, q_{tot} is an order of magnitude larger than during the accretive conditions and is directed offshore. The contribution of q_{hf} to q_{tot} is relatively small, and is now in the offshore direction. The change in direction of q_{lf} over the intertidal bar, as observed during accretive conditions, is also apparent here. The flattening of the beach profile is, however, dominantly caused by the cross-shore gradient in the offshore directed mean flux. These results show that gradients in
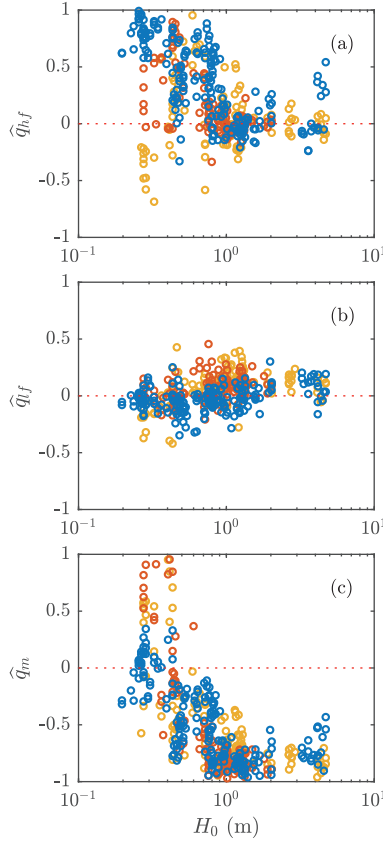
Figure 4.7: Contributions of the (a) short-wave flux q_{hf}, (b) long-wave flux q_{lf} and (c) the mean flux q_m to the total flux ($|q_{hf}| + |q_{lf}| + |q_m|$) versus the offshore significant wave height H_o in the SE data set. The colors indicate the location of the measurements with the (blue) most seaward located rig and (yellow) the most landward located rig.

the measured sand flux can be related qualitatively with morphological changes of the beach profile.

The contribution of the separate transport components q_{hf}, q_{lf} and q_m to q_{tot} for all SE data is shown in Figure 4.7 versus H_o. At the most seaward located rig, $\widehat{q}_{hf}$ is onshore directed and often dominates the total flux for $H_o \lesssim 0.5$ m (blue circles in Figure 4.7a). With increasing offshore wave height, $\widehat{q}_{hf}$ decreases and the flux direction becomes seaward. Observations at the two other rigs also follow this trend for high H_o, but there is a dependency on cross-shore location when wave heights are low. This is explained by a larger heterogeneity in the cross-shore morphology, as the intertidal bar is more pronounced during these conditions. The contribution of q_{lf} can be both positive and negative, and rarely exceeds 20 % of the total flux. As q_{hf} and q_m explain the bulk of the sand fluxes, $|\widehat{q}_m|$ is low when $|\widehat{q}_{hf}|$ is high and vice versa. The total flux is dominated by q_m when $H_o \gtrsim 1$ m. The above-mentioned cell

circulation, and thus a shoreward directed mean current over the bar, was observed during conditions with low H_0 only.

For the low-energetic conditions in the SE dataset when q_{hf} dominates the total suspended flux, i.e. for $H_0 < 0.5$ m, the magnitude of the flux is related with wave characteristics. q_{hf} is largest beneath waves with high root-mean-square orbital velocity (u_{rms}, calculated from u_{hf}) and high A_u (Figures 4.8a and 4.8b). Quantile regression of q_{hf} with A_u gives significant increasing trends for quantiles 0.5 and 0.9, while the magnitude of q_{hf} is unrelated to A_u for $\tau = 0.1$. The absence of a significant increasing trend for the lowest quantile can be explained by the relatively low q_{hf} measured at the rig located in the trough between the intertidal bar and the shoreline. Interestingly, S_u, which is commonly used to predict q_{hf} (e.g., van Rijn, 2007b), is not correlated with the magnitude of q_{hf} in these surf zone measurements (Figure 4.8c). With all wave conditions included, the magnitude of q_{hf} is related with $\bar{u}$ (Figure 4.8d). The downward trend of q_{hf} with increasing seaward directed $\bar{u}$ is significant for quantiles $\tau = 0.1$ and $\tau = 0.5$. This trend is probably related to the offshore directed mean current increasing the flow velocity during the seaward directed phase of the orbital motion and decreasing the velocity during the landward directed phase. These results indicate that u_{rms} and A_u are positively correlated with the magnitude of the onshore directed flux by short-waves, while this flux reduces for increasing offshore-directed $\bar{u}$.

These insights from the SE dataset are applied to scale the normalised q_{hf} for all conditions and to combine the SE data with those of BD and AM. Observations at the most landward SE rig were excluded, as it was often located in the trough between the intertidal bar and the upper beach where fluxes were often minute (Figure 4.6). Furthermore, only observations with offshore-directed $\bar{u}$ were included. The interpretation of trends in $\hat{q}_{hf}$ is complicated as
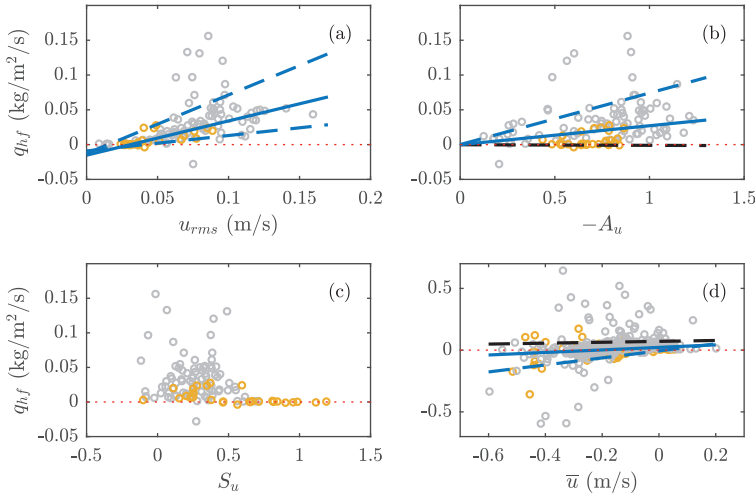
Figure 4.8: Short-wave flux q_{hf} versus (a) root-mean-square orbital velocity u_{rms}, (b) velocity asymmetry $-A_u$, (c) velocity skewness S_u, and (d) mean cross-shore current $\bar{u}$. In (a,b,c) only low-energetic conditions ($H_0 < 0.5$ m) are included, (d) contains all data. Measurements at the most landward located rig are emphasized in yellow. Lines indicate regression over the (dashed) 0.1, (solid) 0.5 and (dashed) 0.9 percentile and are blue when the slope is statistically significant.
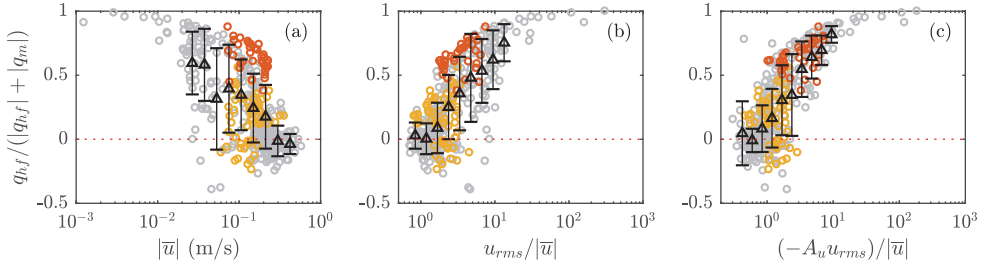
Figure 4.9: Normalised q_{hf} as $q_{hf}/(|q_{hf}| + |q_m|)$ at the selected STM versus (a) $|\overline{u}|$, (b) $u_{rms}/|\overline{u}|$ and (c) $(-A_u u_{rms})/|\overline{u}|$ for the (grey) Sand Engine, (red) BARDEXII and (yellow) Ameland experiments. The triangles show mean values with standard deviation for the data in bins with a bin-width of 0.15 on the log axis.

it also includes q_{lf} and q_m, of which the latter is obviously also related to $\overline{u}$. Scatter in the data due to variations in q_{lf} were omitted here by normalising q_{hf} as $q_{hf}/(|q_{hf}| + |q_m|)$. Observations of $q_{hf}/(|q_{hf}| + |q_m|)$ were subsequently plotted versus $|\overline{u}|$ (Figure 4.9a) to investigate how much of its variability is explained by $\overline{u}$. The SE data shows the full range between q_{hf} dominating over q_m $[q_{hf}/(|q_{hf}| + |q_m|) \sim 1]$ and q_{hf} being of minor importance and in the offshore direction $[q_{hf}/(|q_{hf}| + |q_m|) \sim -0.1]$, as was shown in Figure 4.7a. The range in magnitude of the mean cross-shore current for BD and AM is small and $\overline{u} \sim -0.15$ m/s. The contribution of q_{hf} to the total flux is, however, higher at BD, with $q_{hf}/(|q_{hf}| + |q_m|)$ between 0.4 and 0.9, with a mean of 0.60, versus $q_{hf}/(|q_{hf}| + |q_m|)$ between -0.2 and 0.4, with a mean of 0.11, at AM (Figure 4.9a). When u_{rms} is included as $u_{rms}/|\overline{u}|$ (Figure 4.9b), scatter reduces. The data from BD and AM are now also more separated on the x-axis. This is explained by the relatively large u_{rms} for BD in comparison with AM, the mean $u_{rms}/|u|$ for BD is 3.91 versus 2.13 for AM. The scatter in the data is further reduced by adding A_u as $(-A_u u_{rms})/|\overline{u}|$ (Figure 4.9c), particularly where $q_{hf}/(|q_{hf}| + |q_m|) > 0.5$.

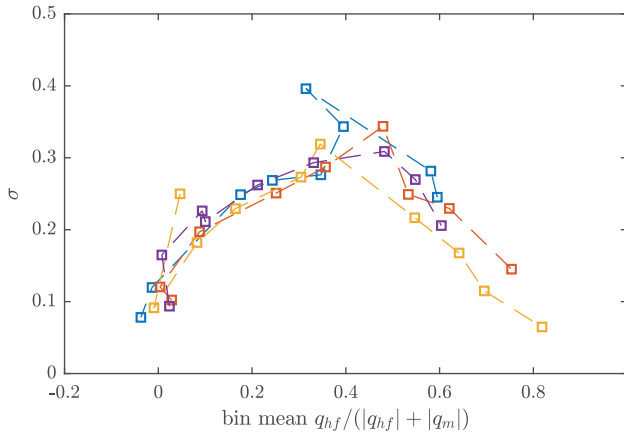**Figure 4.10:** The standard deviation σ of the bins in Figure 4.9 versus the mean of the bins for (blue) $|\overline{u}|$, (red) $u_{rms}/|\overline{u}|$, (yellow) $(-A_u u_{rms})/|\overline{u}|$, and (purple) $(S_u u_{rms})/|\overline{u}|$.

63

To illustrate the trends and scatter, the mean and standard deviation (σ) in $q_{hf}/(|q_{hf}|+|q_m|)$ were calculated in bins with a width of $log_{10}(x) = 0.15$, where x represents the variables on the x-axis in Figure 4.9. Bins were only included in the analysis if they contained more than ten measurements. While σ for $|\overline{u}|$ and $u_{rms}/|\overline{u}|$ is very similar when the bin mean is $q_{hf}/(|q_{hf}| + |q_m|) < 0.4$, σ is smaller when u_{rms} is included for $q_{hf}/(|q_{hf}| + |q_m|) > 0.5$ (Figure 4.10). The reduced scatter in the data for $(-A_u u_{rms})/|\overline{u}|$ is also apparent from σ, as σ is lower for all bins with a bin mean $q_{hf}/(|q_{hf}| + |q_m|) > 0.5$. Furthermore, there is a wider range in the mean values of the bins, and the data are thus better separated. Including S_u instead of $-A_u$ does not result in lower values for σ (Figure 4.10). Moreover, measurements with a high $q_{hf}/(|q_{hf}| + |q_m|)$ are not well separated from conditions with lower values, as the maximum bin mean is only 0.6. A_u is thus more successful than S_u in predicting when the short-wave suspended sand flux dominates over the mean flux in the shallow surf zone. While including wave characteristics u_{rms} and A_u improves the predictability for $q_{hf} > -q_m$, the spread in the data remains when q_m dominates the suspended sand flux.

4.4   Discussion

The short-wave suspended sand flux, measured in the shallow surf zone under a wide variety of wave conditions and on a variety of beaches, was shown to increase with u_{rms} and A_u and to decrease with an increasing offshore-directed $\overline{u}$. The dependency on the wave characteristics u_{rms} and A_u was most apparent when $q_{hf} > -q_m$. This is particularly the case for low-energetic conditions during the SE field campaign, when long period swell waves transformed into highly asymmetric plunging breakers in shallow water. These conditions are typically related with an onshore-directed propagation of the intertidal bar (Figure 4.6; Masselink et al., 2006; Aagaard et al., 2013). Elgar et al. (2001) already discussed field measurements that showed the cross-shore maximum in velocity asymmetry to be consistently colocated with the crest of an onshore migrating bar, and argued that A_u instead of the S_u is driving the onshore migration. The sand flux measurements presented here confirm their hypothesis that, as long as the mean cross-shore current is weak, the onshore directed short-wave flux in the shallow surf zone is more closely related with A_u. Under more energetic conditions, when the net sand flux becomes offshore directed, the magnitude and direction of the short-wave sand flux also depends on the magnitude of the offshore directed mean current. This is explained by the opposing current causing an increase in shear stress during the negative flow phase and a decrease in shear stress during the positive flow phase of the waves. This effect was earlier measured for shear waves (Miles et al., 2002), infragravity waves (de Bakker et al., 2016) and oscillatory flows (Ruessink et al., 2011).

The wave-driven suspended sand transport in morphodynamic models is often included based on empirical parameterisations including the near-bed wave orbital motion and the velocity skewness (e.g., van Rijn, 2007b). These parameterisations include calibration coefficients that are site-specific (e.g., Dubarbier et al., 2015; Walstra et al., 2015; Nienhuis et al., 2016) and optimal settings for deeper water are not necessarily optimal for shallow water and vice versa (Ruggiero et al., 2009). This implies that certain physical processes are either misrepresented or lacking in the transport formulations. The measurements presented in this study show that, in the shallow surf zone, A_u is more closely related with the short-wave driven suspended sand flux than S_u. Including A_u in empirical transport parameterisations could thus improve the performance of morphodynamic models in shallow water. The suitability of A_u to predict the wave-driven sand transport in the shallow surf zone, in contrast to S_u explaining more of the transport in the shoaling and outer surf zone, was earlier

also suggested using numerical models (Hoefel and Elgar, 2003; Calantoni and Puleo, 2006; Fernández-Mora et al., 2015).

The onshore transport by velocity asymmetric flows has been explained by a variety of factors: acceleration skewness (e.g., Austin et al., 2009), phase-lags (e.g., Ruessink et al., 2011; Grasso et al., 2011), boundary layer thickness (Nielsen, 1992), horizontal pressure gradients (e.g., Sleath, 1999; Calantoni and Puleo, 2006; Foster et al., 2006), and breaking-induced turbulence (e.g., van Thiel de Vries et al., 2008, see also Section 4.1). It is thus not necessarily the velocity asymmetry that is driving the onshore wave-induced transport, but rather a combination of processes that are connected to and scale with A_u. To illustrate that, for example, the turbulent kinetic energy k in the water column scales with $A_u u_{rms}^2$, k was estimated from velocity measurements collected during BD (Brinkkemper et al., 2016), AM (Grasso and Ruessink, 2012) and a field campaign at Truc Vert beach (France) in 2008 (Ruessink, 2010; Grasso and Ruessink, 2012). As mentioned in Section 4.2 these measurements could not be collected at SE. During these campaigns, horizontal and vertical flow velocities were measured using three vertically spaced Acoustic Doppler Velocimeters (ADVs). The turbulent velocities were extracted from these measurements using the differencing method (Feddersen and Williams, 2007), see Brinkkemper et al. (2016) for further details on the data processing. Here, data were selected when instruments were between 0.1 and 0.5 m above the bed. These data show a linear correlation of k with $-A_u u_{rms}^2$ (Figure 4.11b), this correlation is with $R^2 = 0.705$ stronger than for u_{rms}^2 alone ($R^2 = 0.490$, Figure 4.11a). Whether surface-induced turbulence beneath surf bores reaches the bed dominantly during the positive or the negative phase of the wave-orbital motion, crucial in order to affect q_{hf}, is not yet clear.

The identification of the impact of the individual processes related with A_u is not necessarily needed to improve transport formulations in practical engineering models, as these models rely largely on empirical parameterisations. Parameterisations based on A_u could be developed to include the combined effect of these processes, including the effect of breaking-induced turbulence. A first step would be to improve parameterisations to accurately predict A_u itself, as the difference in A_u between AM and BD cannot be predicted (Figure 4.5b) using conventional parameterisations based on U_r (Doering and Bowen, 1995; Ruessink et al., 2012a)). The solution might be to include offshore wave steepness and/or the beach slope
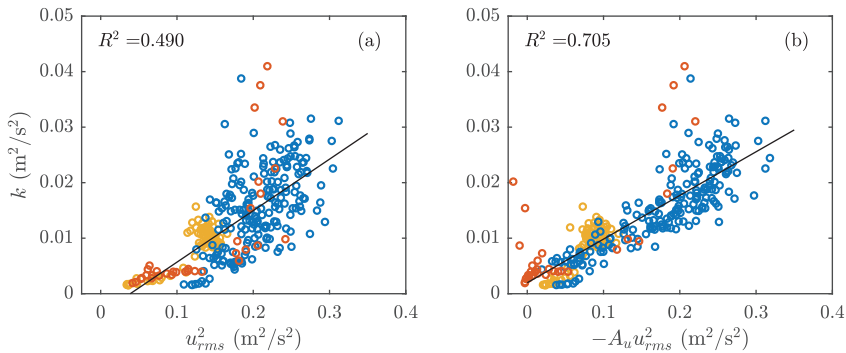

Figure 4.11: Measured turbulent kinetic energy k between 0.1 and 0.5 m above the bed versus (a) u_{rms}^2 and (b) $-A_u u_{rms}^2$ during laboratory experiment (red) BARDEXII, and field campaigns at (blue) Truc Vert beach and (yellow) Ameland.

to make the parameterisations broader applicable, as was recently suggested by Rocha et al. (2017).

The effectiveness of velocity asymmetric flows to induce sand mobilisation and transport was earlier found to depend on sediment grain size (e.g., Ruessink et al., 2009; van der A et al., 2010; Shimamoto et al., 2013), although a positive correlation between the velocity asymmetry and the short-wave transport exists for a wide range in grain sizes (van der A et al., 2010). The data used in this study were collected on beaches consisting of sand with a d_{50} of (AM) 200, (SE) 350 and (BD) 420 μm. While the range in sediment sizes could explain part of the remaining scatter in Figure 4.9, the inclusion of A_u in the parameterisation does reduce scatter both between the SE and BD datasets as well as within the SE dataset. It can therefore be argued that the reduction in scatter cannot be explained solely by the difference in grainsize between the datasets. It is not possible to determine whether this is also true for the smaller grainsize at AM, as the measured fluxes were all in the range $|q_m| > q_{hf}$, where the inclusion of A_u does not result in a better representation of $q_{hf}/(|q_{hf}| + |q_m|)$.

4.5 Conclusions

Near-bed suspended sand fluxes, collected in the shallow surf zone of a moderately sloping natural beach (SE), ranged from onshore directed and short-wave dominated under low energetic conditions ($H_o \lesssim 0.5$ m) to offshore directed and dominated by mean cross-shore currents under high energetic conditions ($H_o \gtrsim 0.8$ m). Cross-shore gradients in these suspended sand fluxes correlate with morphological changes and the fluxes thus relate qualitatively with the total vertically integrated sand transport.

The onshore directed short-wave sand flux during low-energetic conditions is highest beneath larger asymmetric waves and is not correlated with velocity skewness. Short-wave fluxes over the full range of conditions at SE show a correlation with the magnitude of the mean cross-shore current. The short-wave suspended sand flux reduces and reverses in direction with an increase in the offshore directed current. These correlations suggest the short-wave flux in the shallow surf zone to increase with u_{rms} and A_u, and to decrease with increasing offshore directed $\overline{u}$.

Data sets collected in the shallow surf zone of a mildly sloping natural beach (AM) and a steep laboratory beach (BD) were included to further investigate these correlations. The normalised short-wave flux $q_{hf}/(|q_{hf}| + |q_m|)$ scales with $u_{rms}/|\overline{u}|$ for the combination of the three datasets. This relation is further improved for $q_{hf} > |q_m|$ by including the velocity asymmetry. We hypothesize that the velocity asymmetry is a good proxy for the combined effect of several transport mechanisms described in earlier studies, and that including it in a parameterisation of the short-wave sand transport could improve the performance of morphodynamic models in shallow water, in particular to predict onshore migration of intertidal bars during low-energetic conditions and beach recovery.

Chapter 5

Synthesis

5.1   Main findings

The main aim, as stated in Chapter 1, was to better understand the processes involved in sand suspension and transport by short waves in a natural surf zone. This aim was reached by analysing measurements of hydrodynamics, sand concentrations and morphodynamics, collected during a field-scale laboratory experiment and several field campaigns. Three separate research objectives were formulated and studied in Chapters 2–4. Below, the main findings from these chapters are summarised.

5.1.1   Determine the cross-shore variability of turbulence in terms of the vertical profile and the intrawave variability

Most of our knowledge on turbulence characteristics in the nearshore originates from scaled and idealised laboratory experiments. It is, however, unclear how this knowledge translates to the natural environment. To improve our understanding of sand transport processes in shallow water, the field-scale BARDEXII experiment was carried out including measurements of turbulence at one cross-shore location on a steep (1:15) laboratory beach. Different water levels and forced random wave conditions allowed the collection of data beneath a wide range in the fraction of breaking waves. The combination of beach slope and wave steepness resulted in plunging breakers throughout the experiment. The vertical turbulence profile evolves from bottom-dominated to vertically uniform, and the turbulence intensity increases an order of magnitude, with an increase in fraction of breaking waves to ~ 0.5. This has been observed before during more idealised laboratory and field experiments, and reflects the increasing influence of surface-generated turbulence on wave-averaged turbulence intensity. To affect the wave-induced sand transport, the intensity of the breaking-induced turbulence reaching the bed should vary systematically on the timescale of individual waves. To investigate whether this was the case beneath the plunging breakers during BARDEXII, the intrawave variability of turbulence was analysed for non-breaking and breaking waves using a wave phase-averaging approach. Beneath non-breaking waves the near-bed turbulence peaks during flow reversal, indicating that ripple-induced vortex shedding dominates the turbulence flow field (ripple steepness was observed to exceed 0.1). Beneath breaking waves, when ripples are substantially more subdued, turbulence peaks beneath the front of the waves due to the injection of turbulence at the moment the plunging jet hits the water surface. Overall, there are substantial differences in the intensity, vertical structure and intrawave variability of turbulence between the non-breaking and the plunging waves, marking the change from bed- to surface-generated turbulence and the disappearance of vortex ripples.

5.1.2 Analyse the effect of breaking-induced turbulence on the suspension of sand

Consistent with earlier studies, the injection of turbulent vortices by breaking waves dominates the turbulence flow field in the shallow-water surf zone (Chapter 2). The net effect of this breaking-induced turbulence on the magnitude and direction of the short-wave sand transport has not yet been explored systematically. In Chapter 3, turbulence and sand concentration measurements, collected during the BARDEXII experiment, were analysed. Concentration measurements were conducted at four cross-shore locations, from the shoaling into the inner-surf zone. The relation between turbulence and sand suspension was analysed using an event-based and a wave-phase averaging approach. The turbulence and concentration events, defined as events exceeding the mean plus the standard deviation, comprise a small part of the time-series ($\sim 10\%$) but together explain a large part of the mean values ($\sim 40\%$). In the surf zone, $\sim 50\%$ of the suspension events are related to turbulence events within a time-window with a length of the peak wave period. This is higher than the $\sim 40\%$ found by Yoon and Cox (2012) beneath spilling breakers. The wave phase-averaged approach was used to analyse the intrawave variability of turbulence and sand concentration, similar to the method in Chapter 2. It was found that beneath non-breaking shoaling waves sand is mainly in suspension during the maximum onshore directed wave-orbital motion near the bed and a phase-lag is present vertically upward. Beneath breaking waves, concentrations are strongly phase-coupled to the wave-orbital motion and peak at the moment of maximum onshore directed wave-orbital motion throughout the water column. The sand concentration remains phase-coupled and vertically well mixed in the inner-surf zone, although concentrations decrease relative to the outer-surf zone. Overall, turbulence beneath plunging breakers is very effective in stirring sand from the bed and the high degree of vertical mixing beneath those breaking waves results in substantial onshore directed short-wave fluxes.

5.1.3 Determine which hydrodynamic parameters scale with the short-wave sand transport in the shallow surf zone

Sand transport formulas used to calculate surf-zone morphodynamics in practical engineering models are largely based on measurements collected beneath non-breaking regular waves. Earlier research suggested several processes (acceleration skewness, strong opposing currents and surface-induced turbulence) that cause these formulas to perform poorly in the shallow-water surf zone. In Chapter 4, observations of sand fluxes collected during the BARDEXII experiment and during two field campaigns were analysed to gain more insight in the magnitude, direction and relative importance of the short-wave sand transport. The field datasets were collected at the beach of the Dutch barrier island Ameland in 2010 and at the beach of the Sand Engine, a mega-nourishment near the Dutch town Ter Heijde, in 2014, and contained a similar instrument set-up as the BARDEXII experiment. The dataset collected at the Sand Engine contains the largest range in wave conditions and was therefore used to attain general trends. For low-energetic conditions, short-wave sand transport increases with the short-wave root-mean-square orbital motion u_{rms} and with the velocity asymmetry A_u, while a relation with velocity skewness is not found. An increase in the magnitude of the offshore directed mean current $|\overline{u}|$ decreases the short-wave transport and causes it to become negative. Using all datasets, the importance of the short-wave sand transport increases with $(-A_u u_{rms})/|\overline{u}|$. I hypothesise that A_u is a good proxy for the combined effect of multiple transport mechanisms that were identified beneath asymmetric flows in earlier research. The field and laboratory measurements thus support the hypothesis that the inclusion of velocity asymmetry in transport formulations would improve the performance of morphodynamic models in shallow water.

5.2 Discussion and perspectives

5.2.1 Implications for morphodynamic models

In operational wave-averaged morphodynamic models, the short-wave suspended transport is often based on semi-empirical parameterisations including the near-bed wave orbital motion and the velocity skewness (e.g., van Rijn, 2007b), driving an onshore-directed transport for flat-bed conditions beneath non-breaking shoaling waves. These parameterisations include calibration coefficients that were shown to be site-specific (e.g., Dubarbier et al., 2015; Walstra et al., 2015; Nienhuis et al., 2016) and optimal settings for deeper water are not necessarily optimal for shallow water and vice versa (Ruggiero et al., 2009). This implies that certain physical processes are misrepresented or lacking in existing transport formulations. In Chapter 3, I have shown that the intrawave variability in the suspended sand concentration beneath breaking plunging waves differs substantially from the variability beneath non-breaking waves. The high sand concentrations beneath the crest of breaking waves is in previous research ascribed to a variety of suspension mechanisms, e.g., breaking-induced turbulence (e.g., Ting and Kirby, 1995; Aagaard and Hughes, 2010), acceleration skewness (e.g., Nielsen, 1992; Henderson et al., 2004; van der A et al., 2008) and horizontal pressure gradients (Sleath, 1999; Foster et al., 2006; Calantoni and Puleo, 2006). Suspension mechanisms that are currently not included in transport formulations in operational morphodynamic models. To quantify the individual effect of these various mechanisms, highly detailed and idealized laboratory measurements are needed. The question is whether this highly detailed knowledge is necessary to improve practical engineering models, as these models rely on empirical parameterisations of the sand transport, irrespective of the precise mechanisms involved.

The inclusion of the velocity asymmetry in the empirical parameterisations of the short-wave sand transport could be one of the solutions to improve the performance of morphodynamic models in shallow water. The suitability of the velocity asymmetry to predict short-wave transport in the inner-surf zone, in contrast to the velocity skewness in the shoaling zone, was earlier suggested based on velocity measurements in the field (Elgar et al., 2001) and several studies using numerical models (Hoefel and Elgar, 2003; Calantoni and Puleo, 2006; Dubarbier et al., 2015; Fernández-Mora et al., 2015). In Chapter 4, this hypothesis is supported by sand flux measurements collected in the surf zone of a field-scale laboratory beach and in two natural surf zones. It is likely that a myriad of processes which scale with the velocity asymmetry are responsible for this relation with the short-wave sand transport. If true, a practical implication is that a detailed modelling of turbulence beneath breaking waves is not necessary to be included in morphodynamic models. The near-bed turbulent kinetic energy and its effect on sand transport can be predicted directly from velocity asymmetry (e.g., Figure 4.11). A recent example where the effects of acceleration skewness and phase-lags on the short-wave sand transport were included in a morphodynamic model, is the implementation of the SANTOSS transport model (van der A et al., 2013) into Delft3D (van der Werf et al., 2015). The SANTOSS model was developed and validated for a number of laboratory experiments, representing a wide range of non-breaking wave conditions. The implementation of these formulations in the morphodynamic model Delft3D have yet to be fully tested against laboratory and field data and still exclude the effect of breaking-induced turbulence on sand suspension and transport.

In order to use both the velocity skewness and the velocity asymmetry to estimate the short-wave sand transport, an accurate representation of these parameters is essential. Morphodynamic models often use parameterisations of the velocity nonlinearity based on the Ursell number (Ruessink et al., 2012a) as an input to transport formulations (e.g., Dubarbier

et al., 2015; Fernández-Mora et al., 2015; van der Werf et al., 2015). The field measurements from which these were derived show considerable scatter, especially for velocity skewness, and are restricted to mildly sloping beaches ($< 1 : 30$; Ruessink et al., 2012a). Rocha et al. (2017) recently showed that the parameterisations are more broadly applicable by including the offshore wave steepness and the beach slope. While more variables are needed for this approach, those are often readily available in morphodynamic models. Future work should focus on the calibration of these parameterisations, possibly using measurements or simulations with highly advanced (e.g., RANS) wave models, with a wide range of beach slopes and wave conditions. This more accurate approach in the parameterisation of the velocity skewness and asymmetry is needed for morphological models to more accurately predict short-wave sand transport beneath breaking waves in shallow water.

5.2.2 Bedload versus suspended load

The sand concentration during the laboratory- and field-experiments (Chapters 3 and 4) was measured at a minimum elevation of 0.04 m above the bed, and represents the concentration of sand grains in suspension. The sand fluxes in this study, although agreeing with morphological changes (Chapter 4), thus not necessarily represent the direction of the total sand transport, which is comprised of the bedload and suspended load transport. Several studies focused on the ratio between the suspended load and bedload transport in natural surf zones by measuring bedload transport in the form of ripple migration rates. These studies found that, in the surf zone, the bedload transport is approximately a factor 4 smaller than the suspended load transport (Aagaard et al., 2001; Miles and Thorpe, 2015), but can also be of the same magnitude (Masselink et al., 2008) under low-energetic conditions. Detailed measurements under monochromatic plunging waves by van der Zanden et al. (2017) also showed suspended load to dominate the net transport. This was, however, mainly due to strong undertow velocities (and, hence, mean transport), as intrawave variability in sand concentration was measured, except at the location of breaking, in the wave bottom boundary layer only. The field- and laboratory measurements in Chapters 3 and 4 do show such intrawave variability in the suspended load, and the short-wave sand flux occasionally dominates the total suspended flux. Moreover, ripples observed during the laboratory measurements did not show a clear migration direction (Ruessink et al., 2015) and it was therefore concluded that the suspension load was more important than the bedload to the net transport. More detailed simultaneous measurements of suspended load and bedload beneath irregular breaking waves are needed to estimate their relative importance to the total transport, especially during low-energetic conditions leading to beach recovery.

5.2.3 Onshore-directed mean currents

The overall majority of field, laboratory and modelling research on cross-shore morphodynamics, including the present study, assume alongshore-uniformity in bathymetry, and hence in hydrodynamics and sand transport processes. This assumption generally holds during high-energetic conditions, but not necessarily during low-energetic conditions, when nearshore morphology becomes alongshore variable (e.g., Wright and Short, 1984; Van Enckevort et al., 2004). Beach recovery is often associated with 2-dimensional horizontal flow-circulation patterns, with onshore-directed mean currents over the nearshore bar and offshore-directed currents in rip channels dissecting the bar (see also, for example, Plant et al. (2006) and Splinter et al. (2011)). These circulation cells can significantly contribute to the onshore-directed migration of nearshore bars (Aagaard et al., 1998; Aagaard et al., 2006; Aagaard and Vinther, 2008; Masselink et al., 2008; van Maanen et al., 2008) and

were also found to locally dominate the suspended sand transport in the low-energetic surf zone during the field campaign at the Sand Engine beach (Chapter 4, Figure 4.7). Thus, alongshore variability cannot be neglected to fully understand onshore bar migration and beach recovery, as was also pointed out by Almar et al. (2010). These low-energetic conditions with a mean onshore-directed flow often coincide with lower water levels and thus shallow water above the crest of the intertidal bar (Aagaard et al., 2006), which makes it challenging to collect measurements of flow and sand concentration with conventional field equipment (Brinkkemper et al., 2017a). Detailed sand flux measurements in shallow water are, however, needed to determine when, and how much, mean flows are contributing to onshore-directed sandbar migration during low-energetic conditions.

The simultaneous relevance of cross-shore and alongshore processes to coastal evolution is also not reflected in operational morphodynamic models. In general, cross-shore profile models contain reasonably advanced equations for cross-shore sand transport (with the limitations discussed in Section 5.2.1) but cannot predict alongshore variability (see also Walstra et al. (2015)). Most area models do not properly account for cross-shore transport processes, but are suited for the prediction of shoreline evolution for cases that are dominated by alongshore gradients in sand transport, such as along strongly curved coasts (e.g., the Sand Engine (Luijendijk et al., 2017)). Dubarbier et al. (2017) recently included cross-shore processes in a morphodynamic area model and succeeded to simulate an alongshore uniform bar to become alongshore variable while migrating onshore. Considerable more work is, however, needed before their exploratory approach can be used in scientific and applied projects at natural beaches.

Bibliography

Aagaard, T. and M. G. Hughes (2006). Sediment suspension and turbulence in the swash zone of dissipative beaches. *Marine Geology* 228.1-4, pp. 117–135. DOI:10.1016/J.MARGEO.2006.01.003.

Aagaard, T. and M. G. Hughes (2010). Breaker turbulence and sediment suspension in the surf zone. *Marine Geology* 271.3-4, pp. 250–259. DOI:10.1016/J.MARGEO.2010.02.019.

Aagaard, T. and S. G. Jensen (2013). Sediment concentration and vertical mixing under breaking waves. *Marine Geology* 336, pp. 146–159. DOI:10.1016/J.MARGEO.2012.11.015.

Aagaard, T. and N. Vinther (2008). Cross-shore currents in the surf zone: Rips or undertow? *Journal of Coastal Research* 24.3, pp. 561–570.

Aagaard, T., J. Nielsen, and B. Greenwood (1998). Suspended sediment transport and nearshore bar formation on a shallow intermediate-state beach. *Marine Geology* 148.3, pp. 203–225.

Aagaard, T., B. Greenwood, and J. Nielsen (2001). Bed level changes and megaripple migration on a barred beach. *Journal of Coastal Research* SI 34, pp. 110–116.

Aagaard, T., K. P. Black, and B. Greenwood (2002). Cross-shore suspended sediment transport in the surf zone: a field-based parameterization. *Marine Geology* 185.3, pp. 283–302. DOI:10.1016/S0025-3227(02)00193-7.

Aagaard, T., M. Hughes, R. Møller-Sørensen, and S. Andersen (2006). Hydrodynamics and sediment fluxes across an onshore migrating intertidal bar. *Journal of Coastal Research* 22.2, pp. 247–259.

Aagaard, T., B. Greenwood, and M. Hughes (2013). Sediment transport on dissipative, intermediate and reflective beaches. *Earth-Science Reviews* 124, pp. 32–50. DOI:10.1016/J.EARSCIREV.2013.05.002.

Abreu, T., P. A. Silva, F. Sancho, and A. Temperville (2010). Analytical approximate wave form for asymmetric waves. *Coastal Engineering* 57.7, pp. 656–667. DOI:10.1016/J.COASTALENG.2010.02.005.

Almar, R, B Castelle, B. Ruessink, N Sénéchal, P Bonneton, and V Marieu (2010). Two-and three-dimensional double-sandbar system behaviour under intense wave forcing and a meso–macro tidal range. *Continental Shelf Research* 30.7, pp. 781–792. DOI:10.1016/J.CSR.2010.02.001.

Austin, M., G. Masselink, T. O'Hare, and P. Russell (2009). Onshore sediment transport on a sandy beach under varied wave conditions: Flow velocity skewness, wave asymmetry or bed ventilation? *Marine Geology* 259.1, pp. 86–101. DOI:10.1016/J.MARGEO.2009.01.001.

Austin, M. J. and G. Masselink (2008). The effect of bedform dynamics on computing suspended sediment fluxes using optical backscatter sensors and current meters. *Coastal Engineering* 55.3, pp. 251–260. DOI:10.1016/J.COASTALENG.2007.10.003.

Bailard, J. A. (1981). An energetics total load sediment transport model for a plane sloping beach. *Journal of Geophysical Research* 86.C11, pp. 10938–10954.

Barkaszi, S. F. and W. R. Dally (1992). Fine-scale measurement of sediment suspension by breaking waves at Supertank. In: *Proceedings of the 23rd International Coastal Engineering Conference*. Am. Soc. Civil. Eng., New York, pp. 1910–1923.

Battjes, J. A. (1974). Surf similarity. In: *Proceedings of the 14th International Conference on Coastal Engineering*. Copenhagen, Denmark, pp. 466–480.

Beach, R. A. and R. W. Sternberg (1996). Suspended-sediment transport in the surf zone: Response to breaking waves. *Continental Shelf Research* 16.15, pp. 1989–2003.

Black, K. and C. Vincent (2001). High-resolution field measurements and numerical modelling of intra-wave sediment suspension on plane beds under shoaling waves. *Coastal Engineering* 42.2, pp. 173–197. DOI:10.1016/S0378-3839(00)00058-2.

Brinkkemper, J. et al. (2017a). Surf zone morphodynamics during low-moderate energetic conditions; the TASTI field experiment. In: *8th International Conference on Coastal Dynamics, Helsingør, Denmark*.

Brinkkemper, J. A., A. T. M. de Bakker, and B. G. Ruessink (2017b). Intrawave sand suspension in the shoaling and surf zone of a field-scale laboratory beach. *Journal of Geophysical Research: Earth Surface* 122. DOI:10.1002/2016JF004061.

Brinkkemper, J. A., T. Aagaard, A. T. M. de Bakker, and B. G. Ruessink (under review). Short-wave sand transport in the shallow surf zone. *Journal of Geophysical Research: Earth Surface*.

Brinkkemper, J. (2013). Modeling the cross-shore evolution of asymmetry and skewness of surface gravity waves propagating over an intertidal sandbar. MA thesis. Utrecht University, The Netherlands.

Brinkkemper, J. A., T. Lanckriet, F. Grasso, J. A. Puleo, and B. G. Ruessink (2016). Observations of turbulence within the surf and swash zone of a field-scale sandy laboratory beach. *Coastal Engineering* 113, pp. 62–72. DOI:10.1016/J.COASTALENG.2015.07.006.

Butt, T., P. Russell, J. Puleo, J. Miles, and G. Masselink (2004). The influence of bore turbulence on sediment transport in the swash and inner surf zones. *Continental Shelf Research* 24.7-8, pp. 757–771. DOI:10.1016/J.CSR.2004.02.002.

Cade, B. S. and B. R. Noon (2003). A gentle introduction to quantile regression for ecologists. *Frontiers in Ecology and the Environment* 1.8, pp. 412–420. DOI:10.1890/1540-9295(2003)001[0412:AGITQR]2.0.CO;2.

Calantoni, J. and J. A. Puleo (2006). Role of pressure gradients in sheet flow of coarse sediments under sawtooth waves. *Journal of Geophysical Research: Oceans* 111.C1. DOI:10.1029/2005JC002875.

Cox, D. T. and N. Kobayashi (2000). Identification of intense, intermittent coherent motions under shoaling and breaking waves. *Journal of Geophysical Research* 105.C6, pp. 14223–14236. DOI:10.1029/2000JC900048.

De Bakker, A. T. M., M. F. S. Tissier, and B. G. Ruessink (2014). Shoreline dissipation of infragravity waves. *Continental Shelf Research* 72, pp. 73–82. DOI:10.1016/J.CSR.2013.11.013.

De Bakker, A. T. M., J. A. Brinkkemper, F Steen, M. F. S. Tissier, and B. G. Ruessink (2016). Cross-shore sand transport by infragravity waves as a function of beach steepness. *Journal of Geophysical Research: Earth Surface* 121. DOI:10.1002/2016JF003878.

De Ruig, J. H. and R. Hillen (1997). Developments in Dutch coastline management: Conclusions from the second governmental coastal report. *Journal of Coastal Conservation* 3.2, pp. 203–210. DOI:10.1007/BF02905245.

De Schipper, M. A., S. de Vries, G. Ruessink, R. C. de Zeeuw, J. Rutten, C. van Gelder-Maas, and M. J. Stive (2016). Initial spreading of a mega feeder nourishment: Observations of the Sand Engine pilot project. *Coastal Engineering* 111, pp. 23–38.

de Winter, W., D. Wesselman, F. Grasso, and G. Ruessink (2013). Large-scale laboratory observations of beach morphodynamics and turbulence beneath shoaling and breaking waves. *Journal of Coastal Research* 2.65, p. 1515. DOI:10.2112/SI65-256.1.

Doering, J. and A. Bowen (1995). Parametrization of orbital velocity asymmetries of shoaling and breaking waves using bispectral analysis. *Coastal Engineering* 26.1-2, pp. 15–33. DOI:10.1016/0378-3839(95)00007-X.

Dohmen-Janssen, C. M., D. F. Kroekenstoel, W. N. Hassan, and J. S. Ribberink (2002). Phase lags in oscillatory sheet flow: Experiments and bed load modelling. *Coastal Engineering* 46.1, pp. 61–87. DOI:10.1016/S0378-3839(02)00056-X.

Dubarbier, B., B. Castelle, V. Marieu, and G. Ruessink (2015). Process-based modeling of cross-shore sandbar behavior. *Coastal Engineering* 95, pp. 35–50. DOI:10.1016/J.COASTALENG.2014.09.004.

Dubarbier, B., B. Castelle, G. Ruessink, and V. Marieu (2017). Mechanisms controlling the complete accretionary beach state sequence. *Geophysical Research Letters* 44, 5645–5654. DOI:10.1002/2017GL073094.

Elgar, S. (1987). Relationships involving third moments and bispectra of a harmonic process. *IEEE transactions on acoustics, speech, and signal processing* 35.12, pp. 1725–1726.

Elgar, S. and R. Guza (1985a). Observations of bispectra of shoaling surface gravity waves. *Journal of Fluid Mechanics* 161, pp. 425–448. DOI:10.1017/S0022112085003007.

Elgar, S. and R. Guza (1985b). Shoaling gravity waves: Comparisons between field observations, linear theory, and a nonlinear model. *Journal of Fluid Mechanics* 158, pp. 47–70. DOI:10.1017/S0022112085002543.

Elgar, S., E. L. Gallagher, and R. Guza (2001). Nearshore sandbar migration. *Journal of Geophysical Research: Oceans* 106 (C6), pp. 11623–11627. DOI:10.1029/2000JC000389.

Elgar, S., B. Raubenheimer, and R. T. Guza (2005). Quality control of acoustic Doppler velocimeter data in the surfzone. *Measurement Science and Technology* 16.10, pp. 1889–1893. DOI:10.1088/0957-0233/16/10/002.

Feddersen, F. (2012). Scaling surf zone turbulence. *Geophysical Research Letters* 39, p. L18613. DOI:10.1029/2012GL052970.

Feddersen, F. and A. J. Williams (2007). Direct estimation of the Reynolds stress vertical structure in the nearshore. *Journal of Atmospheric and Oceanic Technology* 24.1, pp. 102–116. DOI:10.1175/JTECH1953.1.

Feddersen, F., J. H. Trowbridge, and A. J. Williams (2007). Vertical structure of Dissipation in the Nearshore. *Journal of Physical Oceanography* 37.7, pp. 1764–1777.

Fernández-Mora, A, D Calvete, A Falqués, and H. Swart (2015). Onshore sandbar migration in the surf zone: New insights into the wave-induced sediment transport mechanisms. *Geophysical Research Letters* 42.8, pp. 2869–2877. DOI:10.1002/2014GL063004.

Flick, R. E., R. T. Guza, and D. L. Inman (1981). Elevation and velocity measurements of laboratory shoaling waves. *Journal of geophysical research* 86.5, pp. 4149–4160. DOI:10.1029/JC086iC05p04149.

Foster, D., A. Bowen, R. A. Holman, and P Natoo (2006). Field evidence of pressure gradient induced incipient motion. *Journal of Geophysical Research: Oceans* 111.C5. DOI:10.1029/2004JC002863.

Gallagher, E. L., S. Elgar, and R. Guza (1998). Observations of sand bar evolution on a natural beach. *Journal of Geophysical Research: Oceans* 103.C2, pp. 3203–3215. DOI:10.1029/97JC02765.

Gerbi, G. P., J. H. Trowbridge, E. A. Terray, A. J. Plueddemann, and T. Kukulka (2009). Observations of turbulence in the ocean surface boundary layer: Energetics and transport. *Journal of Physical Oceanography* 39.5, pp. 1077–1096. DOI:10.1175/2008JPO4044.1.

Govender, K., G. P. Mocke, and M. J. Alport (2004). Dissipation of isotropic turbulence and length-scale measurements through the wave roller in laboratory spilling waves. *Journal of Geophysical Research* 109, p. C08018. DOI:10.1029/2003JC002233.

Govender, K., H. Michallet, and M. J. Alport (2011). DCIV measurements of flow fields and turbulence in waves breaking over a bar. *European Journal of Mechanics, B/Fluids* 30, pp. 616–623. DOI:10.1016/J.EUROMECHFLU.2011.09.001.

Grasso, F. and B. G. Ruessink (2012). Turbulent viscosity in natural surf zones. *Geophysical Research Letters* 39.L23603. DOI:10.1029/2012GL054135.

Grasso, F., H. Michallet, and E. Barthélemy (2011). Sediment transport associated with morphological beach changes forced by irregular asymmetric, skewed waves. *Journal of Geophysical Research* 116, p. C03020. DOI:10.1029/2010JC006550.

Grasso, F., B. Castelle, and B. G. Ruessink (2012). Turbulence dissipation under breaking waves and bores in a natural surf zone. *Continental Shelf Research* 43, pp. 133–141.

Hamm, L, M Capobianco, H. Dette, A Lechuga, R Spanhoff, and M. Stive (2002). A summary of European experience with shore nourishment. *Coastal engineering* 47.2, pp. 237–264. DOI:10.1016/S0378-3839(02)00127-8.

Hanes, D. M. and D. A. Huntley (1986). Continuous measurements of suspended sand concentration in a wave dominated nearshore environment. *Continental Shelf Research* 6.4, pp. 585–596. DOI:10.1016/0278-4343(86)90024-5.

Henderson, S. M., J. S. Allen, and P. Newberger (2004). Nearshore sandbar migration predicted by an eddy-diffusive boundary layer model. *Journal of Geophysical Research: Oceans* 109.C6. DOI:10.1029/2003JC002137.

Henriquez, M., A. J. H. M. Reniers, B. G. Ruessink, and M. J. F. Stive (2014). PIV measurements of the bottom boundary layer under nonlinear surface waves. *Coastal Engineering* 94, pp. 33–46.

Hoefel, F. and S. Elgar (2003). Wave-induced sediment transport and sandbar migration. *Science* 299.5614, pp. 1885–1887. DOI:10.1126/SCIENCE.1081448.

Hsu, T.-J., S. Elgar, and R. Guza (2006). Wave-induced sediment transport and onshore sandbar migration. *Coastal Engineering* 53.10, pp. 817–824. DOI:10.1016/J.COASTALENG.2006.04.003.

Jaffe, B. and A. Sallenger Jr. (1992). The contribution of suspension events to sediment transport in the surf zone. In: *Proceedings of the 23rd International Coastal Engineering Conference*. Am. Soc. Civil. Eng., New York. Chap. 3, pp. 2680–2693.

Jaffe, B. E., R. W. Sternberg, and A. H. Sallenger (1984). The role of suspended sediment in shore-normal beach profile changes. In: *Proceedings of the 19th International Coastal Engineering Conference*, pp. 1983–1996.

Janssen, T. T., J. A. Battjes, and A. R. van Dongeren (2003). Long waves induced by short-wave groups over a sloping bottom. *Journal of Geophysical Research: Oceans* 108.C8. DOI:10.1029/2002JC001515.

Kana, T. W. (1978). Surf zone measurements of suspended sediment. In: *Proceedings of 16th Conference on Coastal Engineering*. Hamburg, Germany. Chap. 104, pp. 1725–1743.

Kim, Y., Z. Zhou, T.-J. Hsu, and J. A. Puleo (2017). Large eddy simulation of dam-break-driven swash on a rough-planar beach. *Journal of Geophysical Research: Oceans* 122.2, pp. 1274–1296. DOI:10.1002/2016JC012366.

Kimmoun, O. and H. Branger (2007). A particle image velocimetry investigation on laboratory surf-zone breaking waves over a sloping beach. *Journal of Fluid Mechanics* 588, pp. 353–397.

King, D. B. (1991). Studies in oscillatory flow bedload sediment transport. PhD thesis. Univ. of Calif., San Diego.

Koenker, R. (2005). *Quantile regression*. Cambridge Univ. Press, New York., p. 349.

Kranenburg, W. M., J. S. Ribberink, J. J. Schretlen, and R. E. Uittenbogaard (2013). Sand transport beneath waves: The role of progressive wave streaming and other free surface effects. *Journal of Geophysical Research: Earth Surface* 118.1, pp. 122–139. DOI:10.1029/2012JF002427.

Kuriyama, Y. (2012). Process-based one-dimensional model for cyclic longshore bar evolution. *Coastal Engineering* 62, pp. 48–61. DOI:10.1016/J.COASTALENG.2011.12.001.

Lanckriet, T. and J. A. Puleo (2013). Near-bed turbulence dissipation measurements in the inner surf and swash zone. *Journal of Geophysical Research* 118.12, pp. 6634–6647. DOI:10.1002/2013JC009251.

Lesser, G., J. Roelvink, J. Van Kester, and G. Stelling (2004). Development and validation of a three-dimensional morphological model. *Coastal Engineering* 51.8, pp. 883–915. DOI:10.1016/J.COASTALENG.2004.07.014.

Luijendijk, A. P., R. Ranasinghe, M. A. de Schipper, B. A. Huisman, C. M. Swinkels, D. J. Walstra, and M. J. Stive (2017). The initial morphological response of the Sand Engine: A process-based modelling study. *Coastal Engineering* 119, pp. 1–14. DOI:10.1016/J.COASTALENG.2016.09.005.

Masselink, G. and M. Hughes (2003). Introduction to coastal processes and geomorphology. *London:Hodder Arnold*.

Masselink, G., M. J. Austin, T. J. O'Hare, and P. E. Russell (2007). Geometry and dynamics of wave ripples in the nearshore zone of a coarse sandy beach. *Journal of Geophysical Research* 112.C10022. DOI:10.1029/2006JC003839.

Masselink, G., A. Ruju, D. Conley, I. Turner, G. Ruessink, A. Matias, C. Thompson, B. Castelle, and G. Wolters (2016). Large-scale Barrier Dynamics Experiment II (BARDEX II): experimental design, instrumentation, test programme and data set. *Coastal Engineering* 113, pp. 3–18. DOI:10.1016/J. COASTALENG.2015.07.009.

Masselink, G. and J. A. Puleo (2006). Swash-zone morphodynamics. *Continental Shelf Research* 26.5, pp. 661 –680. DOI:10.1016/J.CSR.2006.01.015.

Masselink, G., A. Kroon, and R. Davidson-Arnott (2006). Morphodynamics of intertidal bars in wave-dominated coastal settings - A review. *Geomorphology* 73.1, pp. 33–49. DOI:10.1016/J.GEOMORPH. 2005.06.007.

Masselink, G., M. Austin, J. Tinker, T. O'Hare, and P. Russell (2008). Cross-shore sediment transport and morphological response on a macrotidal beach with intertidal bar morphology, Truc Vert, France. *Marine Geology* 251.3, pp. 141–155. DOI:10.1016/J.MARGEO.2008.01.010.

McGranahan, G., D. Balk, and B. Anderson (2007). The rising tide: assessing the risks of climate change and human settlements in low elevation coastal zones. *Environment and urbanization* 19.1, pp. 17–37. DOI:10.1177/0956247807076960.

Miles, J. and A. Thorpe (2015). Bedform contributions to cross-shore sediment transport on a dissipative beach. *Coastal Engineering* 98, pp. 65–77. DOI:10.1016/J.COASTALENG.2015.01.007.

Miles, J., P. Russell, B. Ruessink, and D. Huntley (2002). Field observations of the effect of shear waves on sediment suspension and transport. *Continental Shelf Research* 22.4, pp. 657–681. DOI:10.1016/ S0278-4343(01)00095-4.

Mocke, G. P. (2001). Structure and modeling of surf zone turbulence due to wave breaking. *Journal of Geophysical Research* 106.C8, pp. 17039–17057. DOI:10.1029/2000JC900163.

Mori, N., T. Suzuki, and S. Kakuno (2007). Noise of Acoustic Doppler Velocimeter Data in Bubbly Flows. *Journal of Engineering Mechanics* 133.1, pp. 122–125. DOI:10 . 1061 / (ASCE) 0733 - 9399(2007)133:1(122).

Nadaoka, K., S. Ueno, and T. Igarashi (1988). Sediment suspension due to large scale eddies in the surf zone. In: *Proceedings of the 21st International Conference on Coastal Engineering*. Am. Soc. Civil. Eng., New York, pp. 1646–1660.

Nadaoka, K., M. Hino, and Y. Koyano (1989). Structure of the turbulent flow field under breaking waves in the surf zone. *Journal of Fluid Mechanics* 204, pp. 359–387.

Nielsen, P. (1984). Field measurements of time-averaged suspended sediment concentration under waves. *Coastal Engineering* 8, pp. 51–72.

Nielsen, P. (1992). *Coastal Bottom Boundary Layers and Sediment Transport: Advanced Series on Ocean Engineering*. World Scientific.

Nienhuis, J. H., A. D. Ashton, W. Nardin, S. Fagherazzi, and L. Giosan (2016). Alongshore sediment bypassing as a control on river mouth morphodynamics. *Journal of Geophysical Research: Earth Surface* 121.4, pp. 664–683.

O'Donoghue, T. and S. Wright (2004). Flow tunnel measurements of velocities and sand flux in oscillatory sheet flow for well-sorted and graded sands. *Coastal Engineering* 51.11–12, pp. 1163 –1184. DOI:10.1016/J.COASTALENG.2004.08.001.

O'Hara Murray, R. B., P. D. Thorne, and D. M. Hodgson (2011). Intrawave observations of sediment entrainment processes above sand ripples under irregular waves. *Journal of Geophysical Research: Oceans* 116.C1, pp. 2156–2202. DOI:10.1029/2010JC006216.

Osborne, P. D. and B. Greenwood (1992a). Frequency dependent cross-shore suspended sediment transport. 1. A non-barred shoreface. *Marine Geology* 106.1-2, pp. 1–24.

Osborne, P. D. and B. Greenwood (1992b). Frequency dependent cross-shore suspended sediment transport. 2. A barred shoreface. *Marine Geology* 106.1-2, pp. 25–51.

Osborne, P. D. and C. E. Vincent (1996). Vertical and horizontal structure in suspended sand concentrations and wave-induced fluxes over bedforms. *Marine Geology* 131, pp. 195–208.

Pedersen, C., R. Deigaard, and J. Sutherland (1998). Measurements of the vertical correlation in turbulence under broken waves. *Coastal Engineering* 35.4, pp. 231–249.

Plant, N. G., K. T. Holland, and J. A. Puleo (2002). Analysis of the scale of errors in nearshore bathymetric data. *Marine Geology* 191, pp. 71–86. DOI:10.1016/S0025-3227(02)00497-8.

Plant, N. G., K. T. Holland, J. A. Puleo, and E. L. Gallagher (2004). Prediction skill of nearshore profile evolution models. *Journal of Geophysical Research* 109.C01006. DOI:10.1029/2003JC001995.

Plant, N. G., K Todd Holland, and R. A. Holman (2006). A dynamical attractor governs beach response to storms. *Geophysical Research Letters* 33.17. DOI:10.1029/2006GL027105.

Puleo, J. A. (2009). Tidal variability of Swash-Zone Sediment Suspension and Transport. *Journal of Coastal Research* 25.4, pp. 937–948. DOI:10.2112/08-1031.1.

Puleo, J. A., R. V. Johnson, T. Butt, T. N. Kooney, and K. T. Holland (2006). The effect of air bubbles on optical backscatter sensors. *Marine Geology* 230.1, pp. 87–97. DOI:10.1016/J.MARGEO.2006.04.008.

Ribberink, J. S. (1998). Bed-load transport for steady flows and unsteady oscillatory flows. *Coastal Engineering* 34.1-2, pp. 59–82.

Ribberink, J. S. and A. A. Al-Salem (1994). Sediment transport in oscillatory boundary layers in cases of rippled beds and sheet flow. *Journal of Geophysical Research* 99.C6, pp. 12707–12727.

Rijksoverheid (2017). Artikel 3 Beheer, Onderhoud en Vervanging. In: *Rijksbegroting 2017, Section: J Deltafonds*.

Rocha, M., H Michallet, and P. Silva (2017). Improving the parameterization of wave nonlinearities – The importance of wave steepness, spectral bandwidth and beach slope. *Coastal Engineering* 121, pp. 77–89. DOI:10.1016/J.COASTALENG.2016.11.012.

Roelvink, J. A. and M. J. F. Stive (1989). Bar-generating cross-shore flow mechanisms on a beach. *Journal of Geophysical Research* 94.C4, pp. 4785–4800. DOI:10.1029/JC094IC04P04785.

Ruessink, B. G. (2005). Predictive uncertainty of a nearshore bed evolution model. *Continental Shelf Research* 25.9, pp. 1053–1069.

Ruessink, B. G. (2010). Observations of Turbulence within a Natural Surf Zone. *Journal of Physical Oceanography* 40.12, pp. 2696–2712. DOI:10.1175/2010JPO4466.1.

Ruessink, B. G. and Y. Kuriyama (2008). Numerical predictability experiments of cross-shore sandbar migration. *Geophysical Research Letters* 35.L01603. DOI:10.1029/2007GL032530.

Ruessink, B. G., K. T. Houwman, and P. Hoekstra (1998). The systematic contribution of transporting mechanisms to the cross-shore sediment transport in water depths of 3 to 9 m. *Marine Geology* 152, pp. 295–324.

Ruessink, B. G., Y. Kuriyama, A. J. H. M. Reniers, J. A. Roelvink, and D. J. R. Walstra (2007). Modeling cross-shore sandbar behavior on the timescale of weeks. *Journal of Geophysical Research* 112.F3, F03010. DOI:10.1029/2006JF000730.

Ruessink, B. G., T. J. J. van den Berg, and L. C. van Rijn (2009). Modeling sediment transport beneath skewed asymmetric waves above a plane bed. *Journal of Geophysical Research: Oceans* 114.C11021. DOI:10.1029/2009JC005416.

Ruessink, B. G., H. Michallet, T. Abreu, F. Sancho, D. A. Van der A, J. J. van der Werf, and P. A. Silva (2011). Observations of velocities, sand concentrations, and fluxes under velocity-asymmetric oscillatory flows. *Journal of Geophysical Research* 116.C03004. DOI:10.1029/2010JC006443.

Ruessink, B. G., G. Ramaekers, and L. C. van Rijn (2012a). On the parameterization of the free-stream non-linear wave orbital motion in nearshore morphodynamic models. *Coastal Engineering* 65.0, pp. 56 –63. DOI:10.1016/J.COASTALENG.2012.03.006.

Ruessink, B. G., M. Boers, P. F. C. van Geer, A. T. M. de Bakker, A. Pieterse, F. Grasso, and R. C. de Winter (2012b). Towards a process-based model to predict dune erosion along the Dutch Wadden coast. *Netherlands Journal of Geosciences-Geologie en Mijnbouw* 91.3, pp. 357–372.

Ruessink, B. G., J. A. Brinkkemper, and M. G. Kleinhans (2015). Geometry of wave-formed orbital ripples in coarse sand. *Journal of Marine Science and Engineering* 3.4, pp. 1568–1594. DOI:10. 3390/JMSE3041568.

Ruessink, B. G., C. Blenkinsopp, J. A. Brinkkemper, B. Castelle, B. Durbarbier, F. Grasso, J. A. Puleo, T. Lanckriet, and G. Masselink (2016). Sandbar and beachface evolution on a prototype coarse-

grained sandy barrier. *Coastal Engineering* 113, pp. 19–32. DOI:10.1016/J.COASTALENG.2015.11. 005.

Ruggiero, P., D. J. R. Walstra, G. Gelfenbaum, and M. van Ormondt (2009). Seasonal-scale nearshore morphological evolution: Field observations and numerical modeling. *Coastal Engineering* 56.11-12, pp. 1153–1172. DOI:10.1016/J.COASTALENG.2009.08.003.

Sato, S, K Homma, and T Shibayama (1990). Laboratory study on sand suspension due to breaking waves. *Coastal Engineering in Japan* 33.2, pp. 219–231.

Scott, C. P., D. T. Cox, T. B. Maddox, and J. W. Long (2005). Large-scale laboratory observations of turbulence on a fixed barred beach. *Measurement Science and Technology* 16, pp. 1903–1912.

Scott, N. V., T.-J. Hsu, and D. Cox (2009). Steep wave, turbulence, and sediment concentration statistics beneath a breaking wave field and their implications for sediment transport. *Continental Shelf Research* 29.20, pp. 2303–2317. DOI:10.1016/J.CSR.2009.09.008.

Shimamoto, T., P. Nielsen, and T. Baldock (2013). UPDATED "GRAB AND DUMP" MODEL FOR SEDIMENT TRANSPORT UNDER ACCELERATION SKEWED WAVES. In: *Proc. Seventh Int. Conf. on Coastal Dynamics, Bordeaux, France, Bordeaux University*, pp. 1495–1504.

Silva, P. A., T. Abreu, D. A. Van Der A, F. Sancho, B. Ruessink, J. Van der Werf, and J. S. Ribberink (2011). Sediment transport in nonlinear skewed oscillatory flows: Transkew experiments. *Journal of Hydraulic Research* 49.sup1, pp. 72–80. DOI:10.1080/00221686.2011.592681.

Sleath, J. (1999). Conditions for plug formation in oscillatory flow. *Continental Shelf Research* 19.13, pp. 1643–1664. DOI:10.1016/S0278-4343(98)00096-X.

Small, C. and R. J. Nicholls (2003). A global analysis of human settlement in coastal zones. *Journal of Coastal Research* 19.3, pp. 584–599.

Sou, I. M., E. A. Cowen, and P. L.-F. Liu (2010). Evolution of the turbulence structure in the surf and swash zones. *Journal of Fluid Mechanics* 644, pp. 193–216.

Splinter, K. D., R. A. Holman, and N. G. Plant (2011). A behavior-oriented dynamic model for sandbar migration and 2DH evolution. *Journal of Geophysical Research: Oceans* 116.C1. DOI:10.1029/2010JC006382.

Svendsen, I. A. (1987). Analysis of surf zone turbulence. *Journal of Geophysical Research* 92.C5, pp. 5115–5124.

Thorne, P. D., J. J. Williams, and A. G. Davies (2002). Suspended sediments under waves measured in a large-scale flume facility. *Journal of Geophysical Research: Oceans (1978–2012)* 107.C8, pp. 4–1.

Thorne, P. D., A. G. Davies, and J. J. Williams (2003). Measurements of near-bed intra-wave sediment entrainment above vortex ripples. *Geophysical Research Letters* 30.20. DOI:10.1029/2003GL018427.

Thornton, E. B. (1979). Energetics of breaking waves within the surf zone. *Journal of Geophysical Research* 84.C8, pp. 4931–4938.

Thornton, E. B. and R. Guza (1982). Energy saturation and phase speeds measured on a natural beach. *Journal of Geophysical Research: Oceans* 87.C12, pp. 9499–9508. DOI:10.1029/JC087IC12P09499.

Ting, F. C. K. (2001). Laboratory study of wave and turbulence velocities in a broad-banded irregular wave surf zone. *Coastal Engineering* 43.3-4, pp. 183–208.

Ting, F. C. K. (2002). Laboratory study of wave and turbulence characteristics in narrow-band irregular breaking waves. *Coastal Engineering* 46.4, pp. 291–313.

Ting, F. C. K. (2013). Laboratory measurements of large-scale near-bed turbulent flow structures under plunging regular waves. *Coastal Engineering* 77, pp. 120–139.

Ting, F. C. K. and J. T. Kirby (1994). Observation of undertow and turbulence in a laboratory surf zone. *Coastal Engineering* 24.1-2, pp. 51–80.

Ting, F. C. K. and J. T. Kirby (1995). Dynamics of surf-zone turbulence in a strong plunging breaker. *Coastal Engineering* 24.3-4, pp. 177–204.

Ting, F. C. K. and J. T. Kirby (1996). Dynamics of surf-zone turbulence in a spilling breaker. *Coastal Engineering* 27.3-4, pp. 131–160.

Tissier, M., R. Almar, P. Bonneton, H. Michallet, A. de Bakker, and G. Ruessink (2013). Role of short and long-wave interaction on wave celerity in the surf zone of a low-sloping beach. *Proc. Seventh Int. Conf. on Coastal Dynamics, Bordeaux, France, Bordeaux University*, pp. 1677–1686.

Traykovski, P., A. E. Hay, J. D. Irish, and J. F. Lynch (1999). Geometry, migration, and evolution of wave orbital ripples at LEO-15. *Journal of Geophysical Research: Oceans* 104.C1, pp. 1505–1524.

Van Maanen, B., P. J. de Ruiter, G. Coco, K. R. Bryan, and B. G. Ruessink (2008). Onshore sandbar migration at Tairua Beach (New Zealand): Numerical simulations and field measurements. *Marine Geology* 253.3, pp. 99–106. DOI:10.1016/J.MARGEO.2008.05.007.

Van der A, D. A., J. van der Zanden, T. O'Donoghue, D. Hurther, I. Cáceres, S. J. McLelland, and J. S. Ribberink (2017). Large-scale laboratory study of breaking wave hydrodynamics over a fixed bar. *Journal of Geophysical Research: Oceans* 122 (24). DOI:10.1002/2016JC012072.

Van der Werf, J., H. Nomden, J. Ribberink, D.-J. Walstra, and W. Kranenburg (2012). Application of a new sand transport formula within the cross-shore morphodynamic model Unibest-TC. In: *Proceedings of the 33rd International Conference on Coastal Engineering, Santander, Spain*.

Van der Zanden, J, D. van der A, D Hurther, I Cáceres, T O'Donoghue, and J. Ribberink (2016). Near-bed hydrodynamics and turbulence below a large-scale plunging breaking wave over a mobile barred bed profile. *Journal of Geophysical Research: Oceans* 121.8. DOI:10.1002/2016JC011909.

Van der Zanden, J, D Hurther, I Cáceres, T O'Donoghue, J. Ribberink, et al. (2017). Suspended sediment transport around a large-scale laboratory breaker bar. *Coastal Engineering* 125, pp. 51–69. DOI:10.1016/J.COASTALENG.2017.03.007.

van der A, D. A., T. O'Donoghue, A. G. Davies, and J. S. Ribberink (2008). Effects of acceleration skewness on rough bed oscillatory boundary layer flow. In: *Proceedings of the 31st International Conference on Coastal Engineering*. World Sci., Singapore, pp. 1583–1595.

van der A, D. A., T. O'Donoghue, and J. S. Ribberink (2009). SHEET FLOW SAND TRANSPORT PROCESSES IN OSCILLATORY FLOW WITH ACCELERATION SKEWNESS. *Paper 133 in Proc.Coastal Dynamics '09, World Sci., Singapore*.

van der A, D. A., T. O'Donoghue, and J. S. Ribberink (2010). Measurements of sheet flow transport in acceleration-skewed oscillatory flow and comparison with practical formulations. *Coastal Engineering* 57.3, pp. 331 –342. DOI:10.1016/J.COASTALENG.2009.11.006.

van der A, D. A., J. S. Ribberink, J. J. van der Werf, T. O'Donoghue, R. H. Buijsrogge, and W. M. Kranenburg (2013). Practical sand transport formula for non-breaking waves and currents. *Coastal Engineering* 76, pp. 26 –42. DOI:10.1016/J.COASTALENG.2013.01.007.

van der Werf, J. J., J. S. Doucette, T. O'Donoghue, and J. S. Ribberink (2007). Detailed measurements of velocities and suspended sand concentrations over full-scale ripples in regular oscillatory flow. *Journal of Geophysical Research* 112.F02012. DOI:10.1029/2006JF000614.

van der Werf, J., R. Veen, J. Ribberink, and J. van der Zanden (2015). Testing of the new SANTOSS transport formula in the DELFT3D morphological modeling system. In: *The Proceedings of the Coastal Sediments 2015, San Diego, USA*. World Scientific. DOI:10.1142/9789814689977_0100.

Van Enckevort, I. M. J., B. G. Ruessink, G. Coco, K. Suzuki, I. L. Turner, N. G. Plant, and R. A. Holman (2004). Observations of nearshore crescentic sandbars. *Journal of Geophysical Research: Oceans* 109.C6. DOI:10.1029/2003JC002214.

van Rijn, L. C., P. K. Tonnon, and D. J. R. Walstra (2011). Numerical modelling of erosion and accretion of plane sloping beaches at different scales. *Coastal Engineering* 58.7, pp. 637–655. DOI:10.1016/J.COASTALENG.2011.01.009.

van Rijn, L. C. (2007a). Unified view of sediment transport by currents and waves. I: Initiation of motion, bed roughness, and bed-load transport. *Journal of Hydraulic Engineering* 133.6, pp. 649–667. DOI:10.1061/(ASCE)0733-9429(2007)133:6(649).

van Rijn, L. C. (2007b). Unified view of sediment transport by currents and waves II: suspended transport. *Journal of Hydraulic Engineering* 133.6, pp. 668–689. DOI:10.1061/(ASCE)0733-9429(2007)133:6(668).

van Rijn, L. C., J. S. Ribberink, J. van Der Werf, and D. J. R. Walstra (2013). Coastal sediment dynamics: Recent advances and future research needs. *Journal of Hydraulic Research* 51.5, pp. 475–493. DOI:10.1080/00221686.2013.849297.

Van Thiel de Vries, J. S. M., M. R. A. Van Gent, D. J. R. Walstra, and A. J. H. M. Reniers (2008). Analysis of dune erosion processes in large-scale flume experiments. *Coastal Engineering* 55.12, pp. 1028–1040. DOI:10.1016/J.COASTALENG.2008.04.004.

Vincent, C. E. and M. O. Green (1990). Field measurements of the suspended sand concentration profiles and fluxes and of the resuspension coefficient $\gamma 0$ over a rippled bed. *Journal of Geophysical Research: Oceans* 95.C7, pp. 11591–11601. DOI:10.1029/JC095IC07P11591.

Voulgaris, G. and M. B. Collins (2000). Sediment resuspension on beaches: Response to breaking waves. *Marine Geology* 167.1-2, pp. 167–187.

Walstra, D., A. Reniers, R Ranasinghe, J. Roelvink, and B. Ruessink (2012). On bar growth and decay during interannual net offshore migration. *Coastal Engineering* 60, pp. 190–200. DOI:10.1016/J.COASTALENG.2011.10.002.

Walstra, D., B. Ruessink, A. Reniers, and R. Ranasinghe (2015). Process-based modeling of kilometer-scale alongshore sandbar variability. *Earth Eurface Processes and Landforms* 40.8, pp. 995–1005. DOI:10.1002/ESP.3676.

Watanabe, A. and S. Sato (2004). A sheet-flow transport rate formula for asymmetric, forward-leaning waves and currents. In: *Proceedings of the 29th International Conference on Coastal Engineering*. Am. Soc. Civil. Eng., New York, pp. 1703–1714.

Wong, P. P., I. J. Losada, J. P. Gattuso, J. Hinkel, A. Khattabi, K. L. McInnes, Y. Saito, and A. Sallenger (2014). Coastal systems and low-lying areas. In: Climate Change 2014: Impacts, Adaptation, and Vulnerability. Part A: Global and Sectoral Aspects. Contribution of Working Group II to the Fifth Assessment Report of the Intergovernmental Panel on Climate Change. *[Field, C.B., V.R. Barros, D.J. Dokken, K.J. Mach, M.D. Mastrandrea, T.E. Bilir, M. Chatterjee, K.L. Ebi, Y.O. Estrada, R.C. Genova, B. Girma, E.S. Kissel, A.N. Levy, S. MacCracken, P.R. Mastrandrea, and L.L. White (eds.)]* Cambridge University Press, Cambridge, United Kingdom and New York, NY, USA, pp. 361–409.

Wright, L. and A. D. Short (1984). Morphodynamic variability of surf zones and beaches: a synthesis. *Marine geology* 56.1-4, pp. 93–118. DOI:10.1016/0025-3227(84)90008-2.

Yoon, H.-D. and D. T. Cox (2010). Large-scale laboratory observations of wave breaking turbulence over an evolving beach. *Journal of Geophysical Research* 115.C10007. DOI:10.1029/2009JC005748.

Yoon, H.-D. and D. T. Cox (2012). Cross-shore variation of intermittent sediment suspension and turbulence induced by depth-limited wave breaking. *Continental Shelf Research* 47, pp. 93–106. DOI:10.1016/J.CSR.2012.07.001.

Yoon, H.-D., D. T. Cox, and M. Kim (2013). Prediction of time-dependent sediment suspension in the surf zone using artificial neural network. *Coastal Engineering* 71, pp. 78–86. DOI:10.1016/J.COASTALENG.2012.08.005.

Yu, Y., R. W. Sternberg, and R. A. Beach (1993). Kinematics of breaking waves and associated suspended sediment in the nearshore zone. *Continental Shelf Research* 13.11, pp. 1219–1242.

Zhang, D. and T. Sunamura (1990). Conditions for the occurrence of vortices induced by breaking waves. *Coastal Engineering in Japan* 33.2, pp. 145–155.

Zhang, D. P. and T. Sunamura (1994). Multiple bar formation by breaker-induced vortices: a laboratory approach. In: *Proceedings of the 24rd International Conference on Coastal Engineering*. Am. Soc. Civil. Eng., New York, pp. 2856–2870.

Zhou, Z., T.-J. Hsu, D. Cox, and X. Liu (2017). Large-eddy simulation of wave-breaking induced turbulent coherent structures and suspended sediment transport on a barred beach. *Journal of Geophysical Research: Oceans* 122.1. DOI:10.1002/2016JC011884.

About the author

Joost Brinkkemper was born on the 15th of June 1986 in Zaandam, the Netherlands. He graduated from the Bachelor Earth Sciences at the University of Amsterdam in 2007. During his master in Coastal Dynamics and Fluvial Systems at Utrecht University Joost became fascinated by the processes that shape our beaches. During his graduation research he studied the nonlinearity of short-waves propagating over an intertidal sandbar using field measurements and numerical model simulations. Later, during an internship at the LIPC in Merida (Mexico), he focused on wave run-up heights at beaches in the Mexican state of Yucatán. Inspired by these research projects he started this PhD research in 2013. He now holds the position of Specialist Coasts and Seas at WaterProof Marine Consultancy and Services.

Publications

Journal papers

Brinkkemper, J.A., Aagaard, T., de Bakker, A.T.M. & Ruessink, B.G. (under review), Sand transport in the shallow surf zone. Journal of Geophysical Research. Earth Surface

Brinkkemper, J. A., de Bakker, A. T. M. & Ruessink, B. G. (2017), Intrawave sand suspension in the shoaling and surf zone of a field-scale laboratory beach. Journal of Geophysical Research. Earth Surface, 122, 15 p., doi:10.1002/2016JF004061.

de Bakker, A. T. M., Brinkkemper, J. A., Van der Steen, F., Tissier, M. F. S. & Ruessink, B. G. (2016), Cross-shore sand transport by infragravity waves as a function of beach steepness. Journal of Geophysical Research. Earth Surface, 121, 14 p., doi:10.1002/2016JF003878.

Brinkkemper, J. A., Lanckriet, T., Grasso, F., Puleo, J. A. & Ruessink, B. G. (2016), Observations of turbulence within the surf and swash zone of a field-scale sandy laboratory beach. Coastal Engineering, 113, 62-72.

Medellín, G., Brinkkemper, J. A., Torres-Freyermuth, A., Appendini, C. M., Mendoza, E. T. & Salles, P. (2016), Run-up parameterization and beach vulnerability assessment on a barrier island: a downscaling approach. Natural Hazards and Earth System Science, 16 (1), 167-180.

Ruessink, B. G., Blenkinsopp, C., Brinkkemper, J. A., Castelle, B., Dubarbier, B., Grasso, F., Puleo, J. & Lanckriet, T. (2016), Sandbar and beach-face evolution on a prototype coarse sandy barrier. Coastal Engineering, 113, 19-32.

Ruessink, B. G., Brinkkemper, J. A. & Kleinhans, M. G. (2015), Geometry of wave-formed orbital ripples in coarse sand. Journal of Marine Science and Engineering, 3 (4), 1568-1594.

Rijsdijk, K. F., Zinke, J., de Louw, P. G. B., Hume, J. P., van der Plicht, H., Hooghiemstra, H., Meijer, H. J. M., Vonhof, H. B., Porch, N., Florens, F. B. V., Baider, C., van Geel, B., Brinkkemper, J., Vernimmen, T. & Janoo, A. (2011), Mid-Holocene (4200 yr BP) mass mortalities in Mauritius (Mascarenes): Insular vertebrates resilient to climatic extremes but vulnerable to human impact. The Holocene, 12 (8), 1179-1194.

International conferences

Brinkkemper, J., Christensen, D., Price, T., Naus, I., Hansen, A., van Bergeijk, V., van de Wetering, J., Ruessink, G., Ernsten, V. and Aagaard, T. (2017), Surf zone morphodynamics during low-moderate energetic conditions; the TASTI field experiment. 8th International Conference on Coastal Dynamics 2017, Helsingør, Denmark. (oral pres.)

de Bakker, A. T. M., Brinkkemper, J. A., van der Steen, F., Tissier, M. F. S. and Ruessink, B. G. (2016). Cross-shore sand transport by infragravity waves as a function of beach steepness. Ocean Sciences conference, 2016, New Orleans, USA. (oral pres.)

Brinkkemper, J. A. and Ruessink B. G. (2014). Surface-induced turbulence and resulting sand suspension beneath breaking waves. AGU Fall Meeting, 2014, San Francisco, USA. (poster pres.)

Brinkkemper, J. A., Torres-Freyermuth, A., Mendoza, E. T. & Ruessink, B. G. (2013), Parameterization of wave run-up on beaches in Yucatan, Mexico: a numerical study. 7th International Conference on Coastal Dynamics 2013, Bordeaux, France. (oral pres.)